

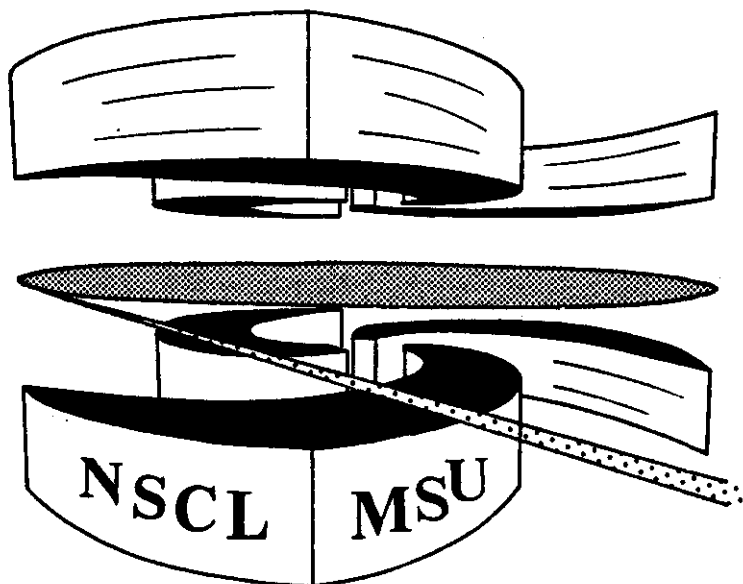


Michigan State University

National Superconducting Cyclotron Laboratory

**EMISSION TEMPERATURES FROM THE DECAY OF
PARTICLE UNSTABLE COMPLEX NUCLEI**

**T.K. NAYAK, T. MURAKAMI, W.G. LYNCH,
K. SWARTZ, D.J. FIELDS, C.K. GELBKE,
Y.D. KIM, J. POCHODZALLA, M.B. TSANG,
H.M. XU, F. ZHU, and K. KWIATKOWSKI**



Emission Temperatures from the Decay of Particle Unstable Complex Nuclei

T.K. Nayak^(a), T. Murakami,^(b) W.G. Lynch, K. Swartz,^(c) D.J. Fields,^(d)
C.K. Gelbke, Y.D. Kim, J. Pochodzalla,^(e) M.B. Tsang, H. M. Xu, and F. Zhu
*National Superconducting Cyclotron Laboratory and
Department of Physics, Michigan State University
East Lansing, Michigan 48824*

K. Kwiatkowski
*Department of Chemistry and Indiana University Cyclotron Facility,
Indiana University, Bloomington, IN 47405*

ABSTRACT

The relative populations of particle-unstable states of intermediate mass fragments were measured for the $^{14}\text{N}+\text{Ag}$ reaction at $E/A = 35$ MeV with a position sensitive hodoscope. These measurements were compared to the predictions of statistical calculations which include the sequential decay of heavier particle unstable nuclei. The best overall agreement between the calculated and measured excited state populations was obtained with calculations which assume emission temperatures of about 3-4 MeV for the primary distributions of the particle unstable intermediate mass fragments. However, a detailed comparison between calculated and measured excited state populations assuming $T_{\text{em}} = 4$ MeV reveals significant discrepancies for about one third to one half of the measured quantities. Calculations which include rotational effects do not satisfactorily account for this discrepancy. These results suggest the possibility of a breakdown in the assumption of local thermal equilibrium at freezeout.

PACS Numbers: 25.70.Np, 25.70.Gh

I. INTRODUCTION

The emission of intermediate-mass-fragments [IMF's, $6 \leq A \leq 30$] is an important decay mode of highly excited nuclear systems formed in proton-nucleus and nucleus-nucleus collisions.^{1,2} Dynamical³ and statistical⁴ models suggest a variety of mechanisms that could be responsible for fragment production. For example, IMF emission may be related to the occurrence of adiabatic instabilities⁵⁻⁸ which may lead to a liquid-gas phase separation for highly excited nuclear matter.⁹⁻¹¹ More conventional fragment emission models have very successfully reproduced many features of the fragment data however, without invoking such bulk instabilities or a liquid-gas phase transition. To distinguish between different mechanisms for fragment production it is important to know whether binary or multifragment breakup configurations predominate in the reaction of interest and whether thermal emission mechanisms can be applied. To apply a particular emission model, one must have the density and excitation energy of the fragmenting system at breakup. Such information may suggest that more than one model may be necessary to describe fragment production for all the different reactions; models that are appropriate for fragment production at low incident energies may be inappropriate for violent nuclear collisions and vice versa.

At low incident energies ($E/A \leq 10$ MeV), intermediate mass fragments can be emitted through the binary decay of a fully equilibrated compound nucleus.¹²⁻¹⁵ As the incident energy of a heavy ion reaction is increased above $E/A = 20$ MeV however, faster non-compound fragment production mechanisms become important. Such processes have cross sections which are strongly forward peaked, indicating the emission of many fragments prior to the attainment of statistical equilibrium for the compound nucleus. The determination of the temperature of the emitting system from fits to the inclusive spectra^{16,17} becomes increasingly problematic at higher incident energies, due to the sensitivity of the spectra

to the Coulomb barrier fluctuations,¹⁸ and strongly time dependent phenomena such as collective motion,^{19–21} and equilibration.¹⁶

Complementary information about the temperature of the fragmenting system may be obtained from the relative populations of ground and excited states of emitted intermediate mass fragments. Statistical models frequently populate the excited states of emitted fragments with statistical weights determined by the excitation energy or “temperature” of the emitting system.^{14,22–25} If one adopts this approximation, the ratio n_1/n_2 of the populations of two narrow excited states of a fragment at freezeout is given by

$$\frac{n_1}{n_2} = \frac{(2J_1 + 1)}{(2J_2 + 1)} \exp\left(-\frac{\Delta E}{T_{\text{em}}}\right) \quad (1)$$

where $\Delta E = E_1^* - E_2^*$; J_i and E_i^* are the spin and excitation energy, respectively, of the i -th state of the fragment, and T_{em} is the “emission temperature” which characterizes the internal excitation energy of the system at freezeout. If the excited states are thermally populated and the feeding from sequential decay of heavier nuclei is not significant, values for T_{em} may be determined from the populations of excited states of emitted fragments.

Emission temperatures of $T_{\text{em}} \approx 3 - 5$ MeV have been deduced from the relative populations of particle stable excited states by γ -ray measurements^{26–29} and from decays of particle-unstable nuclei.^{30–38} Most of these values for the emission temperature were derived from the relative populations of a few states of light mass fragments and do not offer a detailed test of the internal consistency of this approach. More stringent tests may be obtained by comparing measured and calculated excited state populations for isotopes which have many resolved excited states.

In this paper, we describe such a test involving the populations of the particle unstable excited states of intermediate mass fragments emitted in the $^{14}\text{N} + \text{Ag}$ reaction at $E/A = 35$ MeV.³⁹ Experimental details of these measurements are given in section II. Single particle

inclusive spectra and two particle coincidence cross sections will be presented in sections III and IV, respectively. Statistical calculations to assess the influence of sequential feeding are discussed in section V. Apparent temperatures extracted from 40 groups of particle unstable states of Li, Be, B, C, N, and O isotopes are compared to the predictions of statistical feeding calculations in section VI. The question whether angular momentum effects due to rotation of the emitting system can account for the discrepancy between experimental data and model predictions for ^{10}B nuclei is discussed in section VII. Summary and conclusions are given in section VIII.

II. EXPERIMENTAL SETUP

The experiment was performed at the K500 cyclotron of the National Superconducting Cyclotron Laboratory of Michigan State University. A natural silver target of 0.5-mg/cm^2 areal density was bombarded with ^{14}N ions of $E/A=35$ MeV incident energy. Isotopically resolved light particles ($Z \leq 2$) and intermediate-mass fragments ($Z \geq 3$) were measured by a close-packed tetragonal array of thirteen telescopes.⁴⁰ The array was centered at $\theta_{\text{lab}} = 38.4^\circ$, which is significantly larger than the grazing angle $\theta_{\text{gr}} = 6^\circ$. A schematic front view of the detection apparatus is shown in Figure 1. The hodoscope consists of nine light particle telescopes (LP) and four heavy fragment telescopes (HF). One light particle telescope is situated at the center of the array. The four heavy fragment telescopes are situated above, below and to the left and right of the central light particle telescope. At the periphery of the array are situated eight additional light particle telescopes. The light particle and heavy fragment telescopes have solid angles of 4.5 msr and 5.7 msr, respectively. The angular separation between adjacent telescopes is 8° .

Both light particle and heavy fragment telescopes consist of two independent single wire gas proportional counters, providing position information along two orthogonal coordinates

(here denoted by x and y), followed by triple element energy loss telescopes.⁴⁰ For the detection of light particles, a non-planar 200 μm silicon surface barrier detector of 450 mm^2 surface area was used for the first element, a 5 mm thick Si(Li) of 500 mm^2 surface area was used for the second element and a 10 cm thick NaI(Tl) scintillation detector was used for the third element. For the detection of heavy fragments, planar 75 μm and 100 μm silicon surface barrier detectors of 300 mm^2 surface area and 1.5 % thickness uniformity were used for the first and second elements; a 5 mm thick Si(Li) detector of 400 mm^2 was used for the third element.

The position spectra of the gas counters were calibrated with the 5.805 and 5.763 MeV α particles from a 1 mm diameter ^{244}Cm source which was placed at the target location. Figure 2 shows the two dimensional calibration spectrum for a heavy fragment telescope after correction for non-linearities in the position readout. A position resolution of 0.33 ± 0.02 mm FWHM was achieved for α -particles with the heavy fragment detectors, and a slightly worse resolution of 0.50 ± 0.01 was achieved with the light particle detectors. The silicon detectors were calibrated at low energies with ^{241}Am and ^{212}Po α sources. These calibrations were extrapolated to energies of several hundred MeV by injecting a signal from a precision BNC pulser into the input stage of the preamplifiers. In this fashion, relative calibrations of all the silicon detectors were obtained with an estimated accuracy of about 0.5%.

The NaI(Tl) detectors were used to construct singles spectra for light particles. Calibrations for the NaI(Tl) detectors were obtained by converting the ΔE information from the 5 mm Si(Li) detectors to corresponding energies. Calibrations were cross checked by the measurement of energies of recoil protons backscattered from a polypropylene target by a 490 MeV ^{14}N beam. The energy calibrations of NaI(Tl) detectors are estimated to be accurate to within 5%. The particle identification (PID) functions for the light particle telescopes were corrected for the position dependent non-uniformities of the silicon detectors. To ensure

accurate particle identification, software gates were imposed on the positions of the detector which excluded the periphery of the detectors. Further details of the technique are described in Ref. [40].

III. SINGLE PARTICLE INCLUSIVE CROSS SECTIONS

Single particle inclusive energy spectra for hydrogen and helium isotopes are shown in figure 3. Kinetic energy spectra for selected isotopes of lithium, beryllium, boron, carbon, nitrogen, and oxygen are given in figure 4.

All the spectra in figures 3 and 4 are Maxwellian in shape, display maxima at energies close to the exit channel Coulomb barrier and then decrease exponentially at higher energies. Accurate fits to the single particle kinetic energy spectra are required for calculating the efficiency for detecting the decay products of the particle unstable IMF's, and for calculating the backgrounds caused by coincident particles which are emitted independently and do not originate from the decay of a heavier particle unstable IMF. The efficiency and background functions are discussed in the following section and in Ref. [40].

The inclusive data were fitted by using a "moving source" parameterization given by

$$\frac{d^2\sigma}{d\Omega dE} = \sum_{i=1}^3 N_i \sqrt{E - U_c} \exp\{-[E - U_c + E_i - 2\sqrt{E_i(E - U_c)} \cos \theta]/T_i\} \quad (2)$$

where, N_i is a normalization constant, U_c is the kinetic energy gained by the Coulomb repulsion from the residue assumed, for simplicity, to be stationary in the laboratory system, T_i is the kinetic temperature parameter of the i th source, and $E_i = \frac{1}{2}mv_i^2$, where m is the mass of the emitted particle and v_i is the velocity of the i th source in the laboratory system. Fits to the data are shown by the solid lines in figures 3 and 4, obtained with the use of three "moving sources", and the parameter values for the fits are listed in Table 1.

Although the fragment kinetic energy spectra are rather well described by the superposition of the contributions from three sources, the range of angles covered in this experiment was not sufficient to unambiguously establish the parameters of these sources. Indeed, the representation of these spectra by the superposition of an equilibrium plus two non equilibrium sources is an approximation which we justify mainly by the accuracy of our fits. As an illustration of the decomposition into equilibrium and non equilibrium sources imposed by our fits, we show the measured energy spectrum for ^{10}B fragments as the solid points in figure 5 along with the full three moving source fit (solid line) and the best fit assumptions for the equilibrium fit (dashed line). Consistent with Ref. [41], these fits suggest that equilibrium emission plays only a minor role in the emission of the more energetic fragments. The precise magnitude of the equilibrium contribution, however, can not be established without additional measurements at backward angles.

IV. TWO PARTICLE COINCIDENCE CROSS SECTIONS

A. Analysis of the Excitation Energy Spectra

Products from the decay of particle unstable nuclei are detected as coincident particles. From the measured energies and angles of the coincident particles, the relative energy is determined, and, by accumulating all the measured events, the relative energy spectrum $Y_{\text{tot}}(E_{\text{mea}}^*)$ is obtained, E_{mea}^* being the measured excitation energy. This total excitation energy can be decomposed into two parts :

$$Y_{\text{tot}}(E_{\text{mea}}^*) = Y_c(E_{\text{mea}}^*) + Y_{\text{back}}(E_{\text{mea}}^*) \quad (3)$$

where Y_c is the yield from the decay into channel c of the particle unstable nucleus and Y_{back} is a background from coincidences which do not proceed through the decay of the particle unstable nucleus being considered.

The coincidence yield, Y_c can be related to a normalized excitation energy spectrum $|dn(E^*)/dE^*|_c$ in the rest frame of the unstable fragment by the equation,

$$Y_c(E_{\text{mea}}^*) = \int dE^* \epsilon(E^*, E_{\text{mea}}^*) \left| \frac{dn(E^*)}{dE^*} \right|_c \quad (4)$$

where E^* is the actual excitation energy and $\epsilon(E^*, E_{\text{mea}}^*)$ is the efficiency function. The decay yield $|dn(E^*)/dE^*|_c$ is normalized so that $\int^\infty dE^* |dn(E^*)/dE^*|_c$ is the total yield observed in channel c divided by the observed yield of the corresponding particle-stable nucleus.

The efficiency function is calculated for the detector geometry of the hodoscope, by taking into account the position and energy resolutions of the telescopes. It includes corrections for the target beam spot size, multiple scattering and energy loss in the target and the gas detector windows. For simplicity, the efficiency is calculated by assuming that the particle unstable nucleus decays isotropically in its rest frame and that the energy and angular distributions of the excited nucleus are identical to those measured for the corresponding particle-stable nucleus. Both approximations appear to be reasonably accurate.³² Further details of the efficiency calculation are given in Ref. [40]. The regions close to the periphery of the silicon detectors, where only poor isotopic resolution could be attained, were avoided by utilizing software gates on position information. These gates were also imposed on the efficiency calculation. The efficiency function turned out to be somewhat sensitive to the position resolutions of the gas counters. The uncertainties in the efficiency calculations due to the uncertainties in the position resolution of the gas counters were, therefore, estimated and included in establishing the uncertainties in the excited state yields.

The background yield, $Y_{\text{back}}(E_{\text{mea}}^*)$, which appears in equation (3) can be written in an approximate form as

$$Y_{\text{back}} = C_{12} \sigma_1 \sigma_2 [1 + R_{\text{back}}(E_{\text{rel}})], \quad (5)$$

where C_{12} is a normalization constant, σ_1 and σ_2 are the single particle inclusive cross sections

for particles 1 and 2 interpolated with the moving source fits discussed in the last section; E_{rel} is the relative energy of the two particles, and $[1 + R_{\text{back}}(E_{\text{rel}})]$ is the background correlation function. The background correlation function is assumed to vanish for $E_{\text{rel}} \rightarrow 0$ and to go to unity at large E_{rel} where final state interactions can be neglected. In the following, we have parameterized the background correlation function as

$$1 + R_{\text{back}}(E_{\text{rel}}) = 1 - \exp\{-E_{\text{rel}}/\Delta_{\text{b}}\} \quad (6)$$

where $E_{\text{rel}} = E^* - E_{\text{b}}$ and E_{b} is the threshold energy for an excited nucleus to decay by the given decay channel. The fit parameter Δ_{b} governs the width of the minimum at E_{b} . The accuracy of the background parameterization was assessed by constructing the measured total correlation function, $[1 + R_{\text{tot}}(E_{\text{rel}})]$, defined by

$$Y_{\text{tot}}(E_{\text{rel}}) = C_{12} \sigma_1 \sigma_2 [1 + R_{\text{tot}}(E_{\text{rel}})] \quad (7)$$

and comparing the measured correlation function to the background correlation functions for relative energies where no particle unstable states exist. Values for the measured correlation functions were obtained by summing both sides of equation (7) over the energies of particles 1 and 2 corresponding to a fixed relative energy E_{rel} , and choosing C_{12} such that the measured correlation function is unity for large relative energies.

The form of the excitation energy spectrum can be usually obtained from measured phase shifts for the decay channels of a particular particle unstable nucleus of interest, and by adjusting the relative intensities for the yields from different excited states. Here we summarize the main expressions used to extract the excited state population probabilities; further details are given in the appendix. If we assume a thermal population of states, the expression for the decay spectrum of an excited nucleus with a single open channel, c , is

$$\left| \frac{dn(E^*)}{dE^*} \right|_c = C_{\text{stable}} \sum_i \exp\left(-\frac{E^*}{T}\right) \frac{1}{\pi} (2J_i + 1) \frac{\partial \delta_{i,\text{res}}}{\partial E^*}. \quad (8)$$

Here c designates the charges and masses of the daughter fragments. Different channel spins and orbital momenta are indicated by the index i , and $\delta_{i,\text{res}}$ and J_i are the phase shifts and spins which contribute to channel c and C_{stable} is a constant, which is fixed by the requirement that $\int_0^\infty dE^* |dn(E^*)/dE^*|_c$ is the total yield for decay into channel c divided by the total yield of the corresponding particle-stable nucleus.

If the resonant part of the phase shifts in eq. (8) are dominated by isolated levels labelled by an index λ and these resonances have been fitted with the R -matrix formalism for an isolated level, then $\left| \frac{dn(E^*)}{dE^*} \right|_c$ can be approximated by

$$\left| \frac{dn(E^*)}{dE^*} \right|_c = \sum_\lambda \left| \frac{dn_\lambda(E^*)}{dE^*} \right|_c \quad (9)$$

where

$$\left| \frac{dn_\lambda(E^*)}{dE^*} \right|_c = N_\lambda \exp\left(-\frac{E^*}{T}\right) \frac{(2J_\lambda + 1)}{\pi} \times \frac{\Gamma_\lambda/2}{(E_\lambda + \Delta_\lambda - E^*)^2 + \frac{1}{4}\Gamma_\lambda^2} \left[1 - \frac{d\Delta_\lambda}{dE^*} + \frac{E_\lambda + \Delta_\lambda - E^*}{\Gamma_\lambda} \frac{d\Gamma_\lambda}{dE^*} \right] \frac{\Gamma_{\lambda c}}{\Gamma_\lambda}. \quad (10)$$

Here N_λ is a normalization constant, ($N_\lambda = C_{\text{stable}}$ if the states are thermally populated and sequential feeding is negligible), J_λ is the spin of the level, $\Gamma_{\lambda c} = 2P_c\gamma_{\lambda c}^2$ is the partial width of the state, $\Gamma_\lambda = \sum_c \Gamma_{\lambda c}$ is the total width of the state, and $\Delta_\lambda = -\sum_c (S_c - B_c)\gamma_{\lambda c}^2$. Here we include the branching ratio $\Gamma_{\lambda c}/\Gamma_\lambda$ generalizing eq. (8) to accommodate more than one open channel c . The penetration factor P_c , S_c , boundary condition B_c , and the reduced width $\gamma_{\lambda c}^2$ are further defined and discussed in the appendix.

For cases where the resonance parameters Γ_λ and Δ_λ depend weakly on the energy, a Breit-Wigner description for the level parameters is frequently adopted. In these cases, Γ_λ and Δ_λ are constants, and $|dn_\lambda/dE^*|_c$ becomes

$$\left| \frac{dn_\lambda(E^*)}{dE^*} \right|_c = N_\lambda \exp\left(-\frac{E^*}{T}\right) \frac{(2J_\lambda + 1)}{\pi} \frac{\Gamma_\lambda/2}{(E_{\text{res}} - E^*)^2 + \frac{1}{4}\Gamma_\lambda^2} \frac{\Gamma_{\lambda c}}{\Gamma_\lambda}. \quad (11)$$

where E_{res} is the resonance energy for the level λ .

For cases involving the decay of two overlapping states with the same spin and parity, the formulae are rather complicated. These cases are discussed in the appendix where additional information concerning excitation energy spectra are given.

B. Extraction of the Population Probabilities

The decay spectra for most of the particle unstable nuclei discussed here consist of a sum of contributions from various particle unstable levels as defined by eq. (9). If one sums the decays from one of the levels in eq. (9) over the open decay channels, c , one obtains the excitation energy distribution for the level considered :

$$\frac{dn_{\lambda,\text{tot}}(E^*)}{dE^*} = \sum_c \left| \frac{dn_{\lambda}(E^*)}{dE^*} \right|_c. \quad (12)$$

If the branching ratios to the various channels are known, a measurement of a single decay channel is sufficient to evaluate $\frac{dn_{\lambda,\text{tot}}(E^*)}{dE^*}$.

Following Ref. [39], one can define a “population probability”, n_{λ} , for this level, by integrating over the excitation energy

$$n_{\lambda} = \frac{1}{(2J_{\lambda} + 1)} \int dE^* \frac{dn_{\lambda,\text{tot}}(E^*)}{dE^*}. \quad (13)$$

The extra spin degeneracy factor $(2J_{\lambda} + 1)$ in the denominator of the eq. (13) reflects our choice to remain consistent with notation adopted in Ref. [39]. This spin degeneracy factor must be kept in mind during subsequent discussion of the measured and calculated population probabilities.

For the majority of the excitation energy spectra considered here, the excited states are relatively narrow and the Boltzmann factor $\exp(-E^*/T)$ varies little over the resonance

line shape. Then the Boltzmann factor can be approximated by $\exp(-E_{\text{res}}/T)$, and taken out of the integral. The thermal population probability then becomes

$$n_\lambda = N_\lambda \exp(-E_{\text{res}}/T), \quad (14)$$

and in the limit that $\left| \frac{dn(E^*)}{dE^*} \right|_c$ can be approximated by a set of Breit-Wigner resonances, one obtains,

$$\left| \frac{dn(E^*)}{dE^*} \right|_c = \sum_\lambda n_\lambda \frac{(2J_\lambda + 1)}{\pi} \frac{\Gamma_\lambda/2}{(E_{\text{res}} - E^*)^2 + \frac{1}{4}\Gamma_\lambda^2} \frac{\Gamma_{\lambda c}}{\Gamma_\lambda}, \quad (15)$$

and n_λ can be evaluated directly.

Regardless of the form of the fitting expression, $Y_c(E_{\text{mea}}^*)$ is obtained by folding $\left| \frac{dn(E^*)}{dE^*} \right|_c$ against the efficiency function $\epsilon(E^*, E_{\text{mea}}^*)$ according to eq. (4). Because the parameterization of the single particle inclusive spectra for particle stable nuclei of the same isotope are used to evaluate the efficiency function, we have chosen to normalize the population probability such that $n_\lambda \cdot (2J_\lambda + 1)$ is equal to the yield for the state λ divided by the total yield of the particle stable nucleus.

C. Measured Excitation Energy Spectra

Figures 6–12 show correlation functions for lithium and beryllium isotopes, and figures 13–19 show excitation energy spectra for boron, carbon, nitrogen and oxygen isotopes. In all cases, the solid points with error bars indicate the experimental data. The solid lines and dashed lines represent the fits to the data, and associated backgrounds respectively. Spectroscopic information used in fitting the data is given in tables 2–5. The uncertainties in the population probabilities in all cases were assessed by varying the background and also by varying the position resolution assumed in the calculation of the efficiency. An alternate form of the background is depicted by the dotted lines.

1. Particle Unstable states of ${}^5\text{Li}$

Figure 6 shows the correlation function for the decay ${}^5\text{Li} \rightarrow \alpha + \text{p}$. At low relative energies, there is a narrow peak³¹ at $E_{\text{rel}} = 0.19$ MeV due to the two stage decay of ${}^9\text{B}$, where ${}^9\text{B}_{\text{g.s.}} \rightarrow \text{p} + {}^8\text{Be}_{\text{g.s.}} \rightarrow \text{p} + (\alpha + \alpha)$. To estimate the contamination due to the ${}^9\text{B}_{\text{g.s.}}$ decays, a Breit Wigner resonance of width $\Gamma = 0.055$ MeV was included in the fit. The broad peak at $1 \text{ MeV} \leq E_{\text{rel}} \leq 3 \text{ MeV}$ is due to the decay of the ($J^\pi = \frac{3}{2}^-$) particle unbound ground state of ${}^5\text{Li}$. This wide state was fitted with Breit-Wigner line shape using the parameters⁴² given in table 2, and a Boltzmann factor with a value of $T = 3$ MeV was used to describe the temperature dependent function in the line shape. The value of n_λ extracted for this state are not very sensitive to the value of T . Because ${}^5\text{Li}$ has no particle stable states, the energy spectrum for particle stable ${}^6\text{Li}$ was used to calculate the efficiency. As a consequence, the population probabilities given in table 2 are defined relative to the particle stable yield of ${}^6\text{Li}$.

The d- ${}^3\text{He}$ correlation function is shown in figure 7. A pronounced peak corresponding to the ($J^\pi = \frac{3}{2}^+$, 16.66 MeV)⁴² state in ${}^5\text{Li}$ can be seen at $E_{\text{rel}} \approx 0.4$ MeV. This peak was fitted with the R -matrix expression for decay from a single level (equation 10). The resonance parameters for the two decay channels (${}^5\text{Li} \rightarrow \text{d} + {}^3\text{He}$ and ${}^5\text{Li} \rightarrow \text{p} + \alpha$) of this state are $E_\lambda = 129$ keV, $\gamma^2(\text{d}) = 780$ keV, $l_{\text{d}} = 0$, $a_{\text{d}} = 7$ fm, $\gamma^2(\text{p}) = 12$ keV, $l_{\text{p}} = 2$, $a_{\text{p}} = 7$ fm, and the boundary conditions are $B_{\text{d}} = B_{\text{p}} = 0$.⁴² Contributions from the wide state at $E^* = 20$ MeV⁴² are also included in the fit. The resonance parameters for the 16.66 MeV state however, generated a peak in the excitation energy spectrum at an energy of about 280 keV lower than the peak observed experimentally, so the complete spectrum generated by these parameters was shifted by 280 keV to match to the experimental data. Because the d and ${}^3\text{He}$ have different charge to mass ratios, these distortions of the excitation energy spectra can result from Coulomb final state interactions with the residual nucleus.⁴³ Such

effects have not been explored qualitatively for the $d\text{-}^3\text{He}$ system. As in the case of the ^5Li ground state, the population probability n_λ of this state listed in table 2, is defined with respect to the yield of stable ^6Li nuclei.

2. Particle Unstable states of ^6Li

The correlation function for the decay $^6\text{Li} \rightarrow d + \alpha$ is shown in figure 8. An isolated peak corresponding to the $(J^\pi = 3^+, E^* = 2.186 \text{ MeV})^{42}$ state of ^6Li is observed at $E_{\text{rel}} \approx 0.71 \text{ MeV}$. The second maximum in the ^6Li spectra corresponds to excited states of ^6Li at 4.31 MeV ($J^\pi = 2^+$) and 5.65 MeV ($J^\pi = 1^+$). Both the states at 4.31 MeV and 5.65 MeV are so wide that the line shape distortions coming from the Boltzmann factor must be taken into account. The population probabilities for all these states were fitted by Breit-Wigner resonance using the spectroscopic information⁴² given in Table 2 and explicitly including a Boltzmann factor with $T = 4 \text{ MeV}$. In this fit, the population probability for the state at 2.186 MeV was taken as one free parameter, and the populations of states at 4.31 MeV and 5.65 MeV were taken to be equal and were fitted as another free parameter. Values for the extracted population probabilities n_λ , with respect to the ground state yield of ^6Li , are listed in table 2 for the two groups of states.

3. Particle Unstable states of ^7Li

The correlation function for the decay $^7\text{Li} \rightarrow \alpha + t$ is shown in figure 9. The peak located at $E_{\text{rel}} = 2.1622 \text{ MeV}$ corresponds to the $(J^\pi = \frac{7}{2}^-, E^* = 4.630 \text{ MeV})^{42}$ excited state of ^7Li . This peak was fitted with the R -matrix theory (eq. 10) using the resonance parameters ($E_\lambda = 2.80 \text{ MeV}$, $\gamma^2 = 1.3 \text{ MeV}$, $l = 3$, $a = 4 \text{ fm}$, $B = -3$).⁴⁴ A second broad structure in the $\alpha + t$ spectra of figure 9 corresponds to the overlapping $(J^\pi = \frac{5}{2}^-, E^* = 6.68 \text{ MeV})$ and $(J^\pi = \frac{5}{2}^-, E^* = 7.46 \text{ MeV})^{42}$ states of ^7Li . The threshold for neutron decay is at $E^* = 7.25 \text{ MeV}$, and the state at 7.46 MeV decays to both the $\alpha + t$ and $^6\text{Li} + n$ channels. Because these states are overlapping and have the same spins and parities, the phase shifts for these

states were analysed with the R -matrix formalism for two overlapping levels which will be discussed in the appendix and given by eq. 79, using the R -matrix parameters ($E_\lambda = 5.730$ MeV, $\gamma^2(\alpha) = 0.98$ MeV, $l_\alpha = 3, a_\alpha = 4.4$ fm)⁴⁵ for the level at 6.68 MeV, and ($E_\lambda = 5.188$ MeV, $\gamma^2(\alpha) = 0.024$ MeV, $l_\alpha = 3, a_\alpha = 4$ fm, $\gamma^2(n) = 1.2$ MeV, $l_n = 1, a_n = 4$ fm)⁴⁴ for the level at 7.46 MeV, with the boundary conditions $B_\alpha = -3$ and $B_n = -1$. The population probability for the state at 4.63 MeV was fitted individually, and the population probabilities for the overlapping states at 6.68 and 7.46 MeV were assumed to be equal in the fit. The excited state at $E^* = 9.67$ MeV⁴² was included in the fit to better describe the data, but its population probability was not determined.

Figure 10 gives the correlation function for ${}^7\text{Li} \rightarrow {}^6\text{He} + \text{p}$. The peak corresponds to the proton decay of the ($J^\pi = \frac{3}{2}^-$)^{42,46} state at $E^* = 11.24$ MeV. This peak was fitted with the Breit-Wigner resonance parameters given in table 2. The population probabilities for the ${}^7\text{Li}$ excited states n_λ are listed in table 2.

4. Particle Unstable states of ${}^7\text{Be}$

The ${}^3\text{He} + \alpha$ correlation function is shown in figure 11. The states in ${}^7\text{Be}$ are isospin analogs of the ${}^7\text{Li}$ states, and are fitted analogously. The ($J^\pi = \frac{7}{2}^-$) state at $E^* = 4.57$ MeV was fitted with the R -matrix parameters ($E_\lambda = 3.885$ MeV, $\gamma^2(\alpha) = 1.595$ MeV, $l_\alpha = 3, a_\alpha = 4$ fm, $B_\alpha = -3$).⁴⁴ The ($J^\pi = \frac{5}{2}^-$) states at $E^* = 6.73$ MeV and 7.21 MeV were fitted with two-level R -matrix expressions using the R -matrix parameters ($E_\lambda = 9.007$ MeV, $\gamma^2(\alpha) = 3.1$ MeV, $l_\alpha = 3, a_\alpha = 4$ fm) for the 6.73 MeV state and ($E_\lambda = 5.993$ MeV, $\gamma^2(\alpha) = 0.023$ MeV, $l_\alpha = 3, a_\alpha = 4$ fm, $\gamma^2(\text{p}) = 1.2$ MeV, $l_p = 1, a_p = 4$ fm)^{44,47} for the 7.21 MeV state. The corresponding channel boundary conditions are $B_\alpha = -3$ and $B_p = -1$. The population probability for the state at 4.57 MeV and for the doublet at 6.73 and 7.21 MeV are listed in table 2.

The ${}^6\text{Li}+p$ correlation function for ${}^7\text{Be}$ is shown in figure 12. The ($J^\pi = \frac{5}{2}^-$) $E^* = 7.21$ MeV state of ${}^7\text{Be}$ was fitted with the Breit-Wigner formalism. A second state at $E^*=9.27$ MeV⁴² was included in the fit, but its population probability was not determined.

5. Particle Unstable states of ${}^8\text{B}$

The ${}^7\text{Be}+p$ correlation function is shown in Figure 13. Two pronounced maxima corresponding to the $E^* = 0.774$ MeV ($J = 1^+$)⁴² and $E^* = 2.32$ MeV ($J^\pi = 3^+$)⁴² excited states of ${}^8\text{B}$ can be clearly seen. These peaks were fitted by using the Breit-Wigner resonance parameters⁴² given in table 3. The spin of the 0.774 MeV state is taken to be equal to that of the corresponding state⁴² in the mirror nucleus ${}^8\text{Li}$. In the fit, $\Gamma = 310$ keV was used for the state at 2.32 MeV instead of 350 keV⁴² because it gave a better description of the data.

6. Particle Unstable states of ${}^{10}\text{B}$

The measured excitation energy spectra, $Y(E^*)$ for the decay channels ${}^{10}\text{B} \rightarrow {}^6\text{Li} + \alpha$ and ${}^{10}\text{B} \rightarrow {}^9\text{Be} + p$ are shown in Figure 14 as a function of the excitation energy of ${}^{10}\text{B}$. In spite of the good excitation-energy resolution of the hodoscope some of the ${}^{10}\text{B}$ states could not be resolved. For the states within an unresolved group, a common population probability n_λ was assumed. The upper part of the figure shows the ${}^6\text{Li} + \alpha$ coincidence spectrum. The first peak in the ${}^6\text{Li} + \alpha$ corresponds to the ($J^\pi = 3^+$) excited state at 4.774 MeV.^{42,48} The second group consists of the states at $E^* = 5.1103$ MeV ($J^\pi = 2^-$), the state at 5.1639 MeV ($J^\pi = 2^+$) and the ($J^\pi = 1^+$) state at 5.18 MeV.^{42,49} A small shoulder after the second group of states may be due to the decay of the 8.889 MeV and 8.895 MeV excited states of ${}^{10}\text{B}$ to the 3.563 MeV excited state of ${}^6\text{Li}^*$. These two states were included in the fits, but not analyzed further. A third group consists of the ($J^\pi = 2^+$) state at $E^* = 5.9195$ MeV, the ($J^\pi = 4^+$) state at 6.0250 MeV and the ($J^\pi = 3^-$) state at 6.1272 MeV.^{42,49,50} A fourth peak corresponds to the ($J^\pi = 4^-$) state at 6.56 MeV.^{42,50} All the preceding states were

fitted by using the Breit-Wigner parameters given in table 3, and the resulting population probabilities are listed in table 3 as well.

The lower part of Figure 14 shows the coincidence spectra of ${}^9\text{Be}+p$. A pronounced peak at $E^* = 7.5$ MeV is composed of the ($J^\pi = 2^-$) state at 7.43 MeV, the ($J^\pi = 1^+$) state at 7.467 MeV, the ($J^\pi = 2^+$) state at 7.478 MeV and the ($J^\pi = 0^+$) state at 7.5599 MeV.^{42,51} A second group consists of the ($J^\pi = 1^+$) state at 7.67 MeV, the ($J^\pi = 1^-$) state at 7.819 MeV and the ($J^\pi = 2^+$) state at 8.07 MeV.^{42,52} A third group in this spectrum consists of the ($J^\pi = 3^-$) state at 8.889 MeV^{42,53} and ($J^\pi = 2^+$) state at 8.895 MeV.^{42,54} The ($J^\pi = 1^-$) state at 6.873 MeV and the ($J^\pi = 2^+$) state at 7.002 MeV are near the threshold and were not analyzed because the branching ratios are not well known.⁴² These states were fitted by using the Breit-Wigner parameters given in table 3, and the resulting population probabilities are listed in table 3 as well.

7. Particle Unstable states of ${}^{11}\text{C}$

Excitation energy spectra for the decay ${}^{11}\text{C} \rightarrow {}^7\text{Be} + \alpha$ are shown in figure 15. The first peak corresponds to the ($J^\pi = \frac{3}{2}^-$) state at $E^* = 8.1045$ MeV.^{42,55} The second peak corresponds to the ($J^\pi = \frac{5}{2}^-$) state at 8.420 MeV.⁴² The third peak consists of ($J^\pi = \frac{7}{2}^+$) state at 8.655 MeV^{42,56} and the ($J^\pi = \frac{5}{2}^+$) state at 8.701 MeV.⁴² These three groups of states were analyzed using the Breit-Wigner parameters given in table 3, and the resulting population probabilities are listed in table 3 as well. Excited states of ${}^{11}\text{C}$ at $E^* = 9.20, 9.65, 9.78, 9.97, 10.083, 10.069, 11.03, 11.44$ and 12.65 MeV⁴² were also included while fitting the experimental yield, but population probabilities were not extracted for these states because the spectroscopic information for some of these states is uncertain.

8. Particle Unstable states of ${}^{13}\text{N}$

The excitation energy spectrum for the decay ${}^{13}\text{N} \rightarrow {}^{12}\text{C} + p$ is shown in Figure 16. Relative

populations were extracted from two groups of states in ^{13}N . The first group consists of the ($J^\pi = \frac{3}{2}^-$) state at 3.511 MeV and ($J^\pi = \frac{5}{2}^+$) state at 3.547 MeV.⁴² Also analysed was the ($J^\pi = \frac{7}{2}^+$) state at 7.155 MeV which decays to an excited ($E^* = 4.44$ MeV) $^{12}\text{C}^*$ and appears in the excitation energy spectrum at $E^* \approx 2.7$ MeV.⁴² These peaks were analyzed using the Breit-Wigner parameters in table 4 and the extracted population probabilities are given in table 4 as well. Additional excited states of ^{13}N at $E^* = 2.3649, 6.364, 6.886, 7.376, 9.00,$ and 9.476 MeV⁴² were included in the fit to the experimental data, but population probabilities are not provided for these states because they either lack statistics or necessary spectroscopic information is not available.

9. Particle Unstable states of ^{14}N

The excitation energy spectrum for $^{14}\text{N} \rightarrow ^{13}\text{C} + \text{p}$ is shown in Figure 17. Nine groups of excited states were analyzed. The first group consists of the ($J^\pi = 2^-$) state at 7.9669 MeV.⁴² The second group consists of the ($J^\pi = 1^-$) state at 8.062 MeV.⁴² The third consists of the ($J^\pi = 4^-$) state at 8.4899 MeV and the ($J^\pi = 0^+$) state at 8.6197 MeV.⁴² The fourth group is made of three overlapping states, the ($J^\pi = 3^-$) state at 8.9118 MeV the ($J^\pi = 5^+$) state at 8.9638 MeV and the ($J^\pi = 2^+$) state at 8.9804 MeV.⁴² The fifth group consists of the ($J^\pi = 3^+$) state at 9.1289 MeV and ($J^\pi = 2^+$) state at 9.1723 MeV.⁴² The sixth group consists of the ($J^\pi = 2^-$) state at 9.3893 MeV and the ($J^\pi = 2^-$) state at 9.509 MeV.⁴² The seventh group consists of the ($J^\pi = 3^+$) state at 10.079 MeV, and the ($J^\pi = 2^+$) state at 10.101 MeV.⁴² The eighth group consists of an isolated ($J^\pi = 5^+$) state at 10.812 MeV.⁴² The ninth group consists of a ($J^\pi = 3^+$) state at 11.05 MeV.⁴² The excitation energy spectrum was fitted by using the Breit-Wigner parameters given in table 4, and the extracted population probabilities were listed in table 4 as well. Excited states of ^{14}N at $E^* = 9.703, 10.226, 10.432, 10.534, 11.761, 12.2, 12.408$ were also included while fitting the spectrum, but population probabilities from these were not extracted because they either lack the statistics

or the spectroscopic information is not available.

10. Particle Unstable states of ^{16}O

The excitation energy spectrum for the decay $^{16}\text{O} \rightarrow ^{12}\text{C} + \alpha$, is shown in figure 18. Four groups of states were analyzed. The first group consists of the ($J^\pi = 2^-$) state at 12.53 MeV which decays to an excited ($E^* = 4.44$ MeV) $^{12}\text{C}^*$ nucleus.⁴² The second group of peaks at about $E^* = 9.9$ MeV includes the ($J^\pi = 2^+$) state at 9.845 MeV which decays to a ^{12}C in its ground state, and the ($J^\pi = 3^-$) state at 14.1 MeV, the ($J^\pi = 4^-$) state at 14.302 MeV and the ($J^\pi = 5^+$) state at 14.399 MeV which decay to an excited ^{12}C nucleus ($E^* = 4.44$ MeV).⁴² The branching ratios for these latter two decays are not known, therefore we evaluated the sensitivity of our analysis to these states by varying the branching ratios for these states between 0% and 100%. These variations in the branching ratios introduced variations in the relative population probabilities for these states. The range of such variations was used to estimate the systematic uncertainties in the population probabilities associated with these unknown branching ratios. A third group of states consists of the ($J^\pi = 4^+$) state at 10.356 MeV which decays to ^{12}C in its ground state, and the ($J^\pi = 4^+$) state at 14.620 MeV, the ($J^\pi = 5^-$) state at 14.660 MeV, the ($J^\pi = 6^+$) state at 14.815 MeV and the ($J^\pi = 2^+$) state at 14.926 MeV which decay to an excited $^{12}\text{C}^*$ ($E^* = 4.44$ MeV).⁴² A fourth group at about $E_{\text{rel}} = 11$ MeV was also analyzed. This group consists of the ($J^\pi = 4^+$) state at 11.097 MeV which decay to ^{12}C in its ground state.⁴² The state at 15.408 MeV ($J^\pi = 3^-$) which could contribute to this group has a very small ($\approx 1\%$) α branching ratio to the 4.43 excited state.⁴² The fits to the excitation energy spectrum were obtained by using the Breit-Wigner resonance parameters given in table 5, and the resulting population probabilities were listed in table 5 as well. States in ^{16}O corresponding to $E^* = 8.8719, 9.585, 11.52, 11.6, 12.049, 12.440$ MeV which decay to the ground state of ^{12}C and an α particle, and $E^* = 12.796, 12.97, 13.02, 13.09, 13.129, 13.259, 13.664, 13.869, 13.98, 14.032, 15.196, 15.26, 15.785$ and 15.828 MeV⁴²

which decay to an excited $^{12}\text{C}^*$ ($E^* = 4.44$ MeV) and an α particle were also included in fitting the spectra. The population probabilities for these states were not extracted for these states either because they lack statistics or because the necessary spectroscopic information is not available.

11. Particle Unstable states of ^{18}O

The excitation energy spectrum for the decay $^{18}\text{O} \rightarrow ^{14}\text{C} + \alpha$ is shown in figure 19. Three groups of states are identified. The first group consists of the ($J^\pi = 4^+$) state at 7.1169 MeV.^{42,57,58} The second group consists of the ($J^\pi = 5^-$) state at 7.864 MeV.^{42,57,58} The third group consists of the ($J^\pi = 1^-$) state at 8.039 MeV, the ($J^\pi = 5^-$) state at 8.125 MeV, the ($J^\pi = 2^+$) state at 8.213 MeV, and the ($J^\pi = 3^-$) state at 8.282 MeV.^{42,57,58} These peaks are fitted by using the Breit-Wigner resonance parameters given in table 5, and the resulting population probabilities are also listed in the table. A zero background was used for the alternate background for the estimation of the uncertainty due to the background subtraction.

V. SEQUENTIAL FEEDING FROM HIGHER-LYING STATES

If the excitation energy at freezeout is thermally distributed, and rotational effects are small, the primary population probabilities for the excited states of a specific intermediate mass fragment should follow a Boltzmann distribution. The observed populations of excited states are influenced however by the sequential decay of heavier particle unstable nuclei,^{28-30,37,59-63} and the populations and decays of many of these unbound states are not known experimentally. We have performed statistical calculations following the approach outlined in Ref. [29] to estimate the influence of feeding on measured values of population probabilities.

A. Levels and Level Densities

Sequential decay calculations were performed for an ensemble of nuclei with $3 \leq Z \leq 13$. Since the spins, isospins and parities of many low-lying particle bound and unbound levels of nuclei with $Z \leq 11$ are known, a lookup table containing excitation energies, spins, isospins, parities and branching ratios for approximately 2600 known levels for isotopes within this charge range⁴² was constructed, and used in the sequential decay calculations. For known levels with incomplete spectroscopic information, values for the spin, isospin, and parity were chosen randomly according to primary distributions obtained from the non-interacting shell model.⁶⁴ The calculations were repeated with different initial values for the unknown spectroscopic information until the sensitivities of the calculations to these spectroscopic uncertainties were assessed.

The low-lying discrete levels of heavier nuclei with $Z \geq 12$ are not as well known as those of lighter nuclei. To calculate the decay of these heavier nuclei for low excitation energies, $E^* \leq \epsilon_0(A_i, Z_i)$, we used a continuum approximation to the discrete level density,⁶³ modifying the empirical interpolation formula of Ref. [65] to include a spin dependence:

$$\rho(E^*, J_i) = \frac{1}{T_1} \exp[(E^* - E_1)/T_1] \frac{(2J_i + 1) \exp[-(J_i + \frac{1}{2})^2/2\sigma_i^2]}{\Sigma(2J_i + 1) \exp[-(J_i + \frac{1}{2})^2/2\sigma_i^2]}, \quad (16)$$

$$\text{for } E^* \leq \epsilon_0, \quad \text{where} \quad \sigma_i^2 = 0.0888[a_i(\epsilon_0 - E_0)]^{\frac{1}{2}} A_i^{\frac{2}{3}},$$

and $a_i = A_i/8$; J_i , A_i , and Z_i are the spin, mass and charge numbers of the fragment. The values for $\epsilon_0 = \epsilon_0(A_i, Z_i)$, $T_1 = T_1(A_i, Z_i)$, and $E_1 = E_1(A_i, Z_i)$ were taken from Ref. 65. For $Z \geq 12$, $E_0 = E_0(A_i, Z_i)$ is determined by matching the level density at ϵ_0 provided by eq. (16) to that provided by eq. (17) given below. [Note: In eq. (16) and also in eq. (17) below, we match the density of levels rather than the density of states because the spins of many of the discrete levels are not known.]

For higher excitation energies in the continuum for all nuclei, we assumed the level

density of the form

$$\rho(E^*, J_i) = \rho_1(E^*) \rho_2(J_i, \sigma_i), \quad (17)$$

$$\begin{aligned} \text{where} \quad \rho_1(E^*) &= \frac{\exp\{2[a_i(E^* - E_0)]^{1/2}\}}{12\sqrt{2}[a_i(E^* - E_0)^5]^{1/4}\sigma_i}, \\ \rho_2(J_i, \sigma_i) &= \frac{(2J_i + 1)\exp[-(J_i + \frac{1}{2})^2/2\sigma_i^2]}{2\sigma_i^2}, \\ \sigma_i^2 &= 0.0888[a_i(E^* - E_0)]^{1/2}A_i^{2/3}. \end{aligned}$$

For $Z_i \geq 12$, $E_0 = E_0(A_i, Z_i)$ is determined by matching the level density provided by eq. (16) at ϵ_0 to that provided by eq. (17). At smaller values of Z_i , E_0 is adjusted for each fragment to match the integral of the continuum level density to the total number of tabulated levels according to the equation:

$$\int_{E_0}^{\epsilon_0} dE^* \int dJ \rho(E^*, J) = \int_0^{\epsilon_0} dE \sum_i \delta(E - E^*), \quad (18)$$

where ϵ_0 , for these lighter fragments, was chosen to be the maximum excitation energy up to which the information concerning the number and locations of discrete states appears to be complete.

To reduce the computer memory requirements, the populations of continuum states were stored at discrete excitation energy intervals of 1 MeV for $E^* \leq 15$ MeV, 2 MeV for $15 \leq E^* \leq 30$ MeV, and 3 MeV for $E^* \geq 30$ MeV. The results of these calculations do not appear to be sensitive to these binning widths. Parities of continuum states were chosen to be positive and negative with equal probability. To save both space and time, the isospins of the continuum states were taken to be equal to the isospin of the ground state of the same nucleus.

B. Primary Populations

For the i th level of spin J_i we assumed an initial population P_i given by

$$P_i \propto P_0(A_i, Z_i)(2J_i + 1) \exp(-E^*/T_{\text{em}}), \quad (19)$$

where $P_0(A_i, Z_i)$ denotes the population per spin degree of freedom of the ground state of a fragment and T_{em} is the emission temperature which characterizes the thermal population of states of a given isotope. (This temperature is assumed to be associated with the intrinsic excitation of the fragmenting system at breakup and may be different from the “kinetic” temperature which may be extracted from the kinetic energy spectra of the emitted fragments.) The initial populations of states of a given fragment were assumed to be thermal up to excitation energy of $E_{\text{cutoff}}^* = A \cdot 5$ MeV, corresponding to a mean lifetime of the continuum states at the cutoff energy about 125 fm/c.⁶⁶

For simplicity, we parameterized the initial relative populations, $P_0(A_i, Z_i)$ by

$$P_0(A, Z) \propto \exp(-fV_C/T_{\text{em}} + Q/T_{\text{em}}), \quad (20)$$

where V_C is the Coulomb barrier for emission from a parent nucleus of mass and atomic numbers A_p and Z_p and Q is the ground state Q -value

$$V_C = Z_i(Z_p - Z_i)e^2/\{r_0[A_i^{1/3} + (A_p - A_i)^{1/3}]\} \quad (21)$$

$$\text{and} \quad Q = [B(A_p - A_i, Z_p - Z_i) + B_i] - B(A_p, Z_p). \quad (22)$$

We used a radius parameter of $r_0=1.2$ fm, $A_p=122$, $Z_p=54$. For heavy nuclei, the binding energies, $B(A, Z)$, of heavy nuclei were calculated from the Weizsacker mass formula⁶⁷ and for the emitted light fragments we used the measured binding energies, B_i , of the respective ground states.⁶⁸ At each temperature T_{em} , the parameter, f in eq. (20) was adjusted to provide optimal agreement between the calculated final fragment distributions (obtained after the decay of particle unstable states) and the measured fragment distributions. This

constraint reduced the possibility of inaccuracies in the predicted primary elemental distributions at high temperatures.^{61,62} The values of f obtained for different T_{em} are discussed in the last part of this section.

C. Branching Ratios

Particle decay branching ratios were calculated for the n, 2n, p, 2p, d, t, ^3He , α channels. The decays via γ rays were taken into account for calculations of the final particle stable yields. Tabulated branching ratios were used whenever possible to describe the decay of particle unstable states. Where such information was not available, the branching ratios were calculated from the Hauser-Feshbach formula,⁶⁹ taking into account constraints imposed by isospin and parity conservation. The branching ratio for a channel c was taken to be

$$\frac{\Gamma_c}{\Gamma} = \frac{G_c}{\sum_i G_i} \quad (23)$$

$$\text{where} \quad G_c = \langle T_{I,D} T_{I,F} T(3)_{I,D} T(3)_{I,F} | T_{I,P} T(3)_{I,P} \rangle^2 \\ \times \sum_{Z=|S+j|}^{Z=|S+j|} \sum_{l=|J+Z|}^{l=|J+Z|} \{ [1 + \pi_P \pi_D \pi_F (-1)^l] / 2 \} T_l(E). \quad (24)$$

Here, J and j are the spins of the parent and daughter nuclei, Z is the channel spin, S and l are the intrinsic spin and orbital angular momentum of the emitted particle, and $T_l(E)$ is the transmission coefficient for the l th partial wave. The factor, $[1 + \pi_P \pi_D \pi_F (-1)^l] / 2$ enforces parity conservation and depends on the parities $\pi = \pm 1$ of the emitted fragment and the parent and daughter nuclei. The Clebsch-Gordon coefficient involving $T_{I,P}$, $T_{I,D}$, and $T_{I,F}$, the isospins of the parent nucleus, daughter nucleus, and emitted particle, likewise allows one to take isospin conservation into account.

For decays from states when the kinetic energy of the emitted particle is less than 20 MeV and $l \leq 20$, the transmission coefficients were interpolated from a set of calculated optical model transmission coefficients. For decays from continuum states when the

kinetic energy of the emitted particle exceeds 20 MeV, the transmission coefficients were approximated by the sharp cutoff approximation.

D. Results

Calculations were performed for $T_{em} = 2, 3, 4, 5, 6,$ and 8 MeV. The measured fragment elemental and isotopic distributions and calculated final elemental distributions for $E_{cutoff}^*/A = 5$ MeV are compared for different values of T_{em} in figures 20, 21 and 22. The solid points correspond to the fragment yields at $\theta = 38^\circ$ summed over all measured energies. The dashed lines in Figure 20 show the calculated elemental distributions of primary fragments assumed for each temperature. The fitted parameters, f , are indicated in the figure. The solid lines show the calculated final elemental distributions obtained after the statistical decay of particle unbound fragments. At each temperature the parameter, f , was adjusted so that the calculated final elemental distribution closely follows the trend of the measured elemental distribution. Since these parameters, f , have been adjusted to reproduce the elemental yields measured in this experiment, one must be very cautious about applying the results of these calculations to other reactions. The solid histograms in figure 21 and 22 represent final isotopic distributions obtained for each temperature. In general, the trends of the isotopic distributions are reproduced.

At each temperature T_{em} , the relative population probabilities were calculated taking sequential feeding into account. In the following sections, these calculated population probabilities are compared to the experimental data to assess whether these calculations can explain the measured population probabilities.

VI. Emission Temperatures

To provide an overall comparison between the calculated and measured population probabilities, we performed a least-squares analysis, computing

$$\chi_\nu^2 = \frac{1}{\nu} \sum_{i=1}^{\nu} \frac{(y_{\text{exp},i} - y_{\text{cal},i})^2}{\sigma_i^2} \quad (25)$$

for each initial temperature in the calculation. Here $y_{\text{exp},i}$ and $y_{\text{cal},i}$ are the experimental and calculated values of the population probabilities or ratios of population probabilities and ν is the number of data points. The uncertainty σ_i is given by $\sigma_i^2 = \sigma_{\text{exp},i}^2 + \sigma_{\text{cal},i}^2$ where $\sigma_{\text{exp},i}$ is the experimental uncertainty, and $\sigma_{\text{cal},i}$ reflects the range of calculated values obtained when the spins, isospins, and parities were varied for the states where these information are incomplete. Restricting the summation to the mathematically independent population probabilities makes the χ_ν^2 function unduly sensitive to the feeding corrections to the populations of particle stable states. The ratios of population probabilities have the advantage of being sensitive to these feeding corrections even though they are not completely independent.

Values for χ_ν^2 were computed according to eq. (25) for combinations of population probabilities and the ratios of population probabilities. The results are presented in Fig. 23 for four groups : $Z = 3, 4$; $Z = 5, 6$; $Z = 7$; and $Z = 8$, as functions of the temperature ($T_{\text{em}} = 2 - 8$ MeV) of the primary distribution assumed in the feeding calculation. The solid lines depict values for χ_ν^2 where both the independent population probabilities and all the ratios of populations have been included, and the dash-dotted lines show χ_ν^2 where just the ratios of population probabilities are included. Results for lithium and beryllium isotopes, shown in the upper left hand window of the figure, display a minimum at about $T_{\text{em}} \approx 3$ MeV for the ratios of population probabilities alone and at about $T_{\text{em}} \approx 4$ MeV when all the quantities are combined. Similar calculations for Boron and Carbon isotopes, shown in the upper right hand window, display minima at about $T_{\text{em}} \approx 3$ MeV. The results for nitrogen isotopes, shown in the lower left hand window, display a minimum at $T_{\text{em}} \approx 4$ MeV for

the ratios of population probabilities alone. This minimum shifts to $T_{\text{em}} \approx 3$ MeV when χ_ν^2 values of the population probabilities are added. For the oxygen isotopes, shown in the lower right hand window few groups of states are detected, and the locations of the minima in the χ_ν^2 functions are not well determined.

These comparisons of the temperature dependence of χ_ν^2 do not reveal any unambiguous dependence of the emission temperature on the fragment charge. We have therefore combined the results for all fragments to get an improved measure for T_{em} . The solid curve in Fig. 24 depicts the values of χ_ν^2 where the independent population probabilities and the ratios of population probabilities have been included. The dashed line in the figure indicates the values, where χ_ν^2 is summed over only the independent population probabilities of all fragments ($3 \leq Z \leq 8$), and the dash-dotted line shows the corresponding values where the sum includes just the ratios of population probabilities of all fragments. Minimum values for χ_ν^2 occur in these comparison at emission temperatures of $T_{\text{em}} \approx 3 - 4$ MeV. For comparison, the dotted line in the figure shows the χ_ν^2 value for the ratio between the population probabilities of ^5Li in its ground and 16.66 MeV excited states. Calculations predict that the relative populations of ^5Li excited states to be rather insensitive to the corrections due to the sequential feeding from heavier particle unstable nuclei. The minimum value of χ_ν^2 occurs at $T_{\text{em}} = 4$ MeV for the ^5Li states, consistent with the emission temperatures extracted from the $^{14}\text{N}+^{197}\text{Au}$ system at $E/A = 35$ MeV.

Even for $T_{\text{em}} \approx 3 - 4$ MeV, the values of χ_ν^2 shown in figures 24 and 25 are rather large indicating that the discrepancies between measurement and calculation are significant. To explore this issue in greater detail, we will present individual comparisons between the experimental and calculated population probabilities and the ratios of population probabilities at $T_{\text{em}} = 4$ MeV. In these comparisons, we calculate an apparent emission temperature T_{app}

defined by the relation

$$\frac{n_i}{n_j} = \exp(-[E_i^* - E_j^*]\beta_{\text{app}}), \quad (26)$$

where $\beta_{\text{app}} = 1/T_{\text{app}}$. Using the definition of the population probability to simplify the above equation for cases where j denotes the ground state, one obtains,

$$(2J_{\text{g.s.}} + 1)n_i = \exp(-E_i^* \beta_{\text{app}}), \quad (27)$$

where $J_{\text{g.s.}}$ is the spin of the ground state. Equations 26 and 27 can be used to define T_{app} in terms of ratios of either measured or calculated values of n_i and n_j . Because values for T_{app} calculated by eq. (26) and (27) can be negative or infinite, we extract and assign an uncertainty to β_{app} rather than to T_{app} .

In figures 25, 26, 27, 28 we present values for β_{app} (on the lower axis) and $T_{\text{app}} = 1/\beta_{\text{app}}$ (on the upper axis) for population probabilities and ratios of population probabilities for isotopes with $Z = 3, 4$; $Z = 5, 6$; $Z = 7$; and $Z = 8$, respectively. The solid points represent the values for β_{app} obtained for experimental population probabilities or the ratios of population probabilities. In cases where states are not resolved, the quantities are calculated for groups of states defined in tables 2 – 5. The histograms represent corresponding values for β_{app} obtained from sequential feeding calculations starting with an initial temperature $T_{\text{em}} = 4$ MeV. The uncertainties in the calculation are designated by the spread of the histogram which is shaded in the figure. In this figure, only those cases are plotted for which both the calculated or experimental uncertainties are smaller than the dynamical range of the figure.

Values for β_{app} and T_{app} obtained from the population probabilities of two groups of states in ${}^5\text{Li}$ and ${}^6\text{Li}$, and three groups of states in ${}^7\text{Li}$ and ${}^7\text{Be}$ are shown in figure 25. (The relevant populations were given in table 2). The experimental data in figure 25 for the population of states in ${}^5\text{Li}$, ${}^6\text{Li}$, and ${}^7\text{Li}$ are comparable to the results obtained for the

fragments in previous measurements at similar energies^{32,63} The calculations and data are in good agreement for ratios involving the widely separated ground state and 16.66 MeV excited state of ${}^5\text{Li}$ [$\Delta E = 16.66$ MeV], which is rather insensitive to sequential feeding.^{61,62} For most transitions, the calculated apparent temperatures are similar to the measured ones.

The values for β_{app} and T_{app} obtained from measured and calculated population probabilities for groups of states in ${}^8\text{B}$, ${}^{10}\text{B}$ and ${}^{11}\text{C}$ are presented in figure 26. For convenience of presentation, the ratios are labelled according to the groups of states discussed in section IV. In general, the population probabilities for the three nuclei are moderately well described by the calculations. The measured ratio of the second group of excited states to the first group of excited states of ${}^8\text{B}$ is significantly larger than the corresponding ratio predicted by the sequential feeding calculations. Even larger discrepancies are observed for excited states of ${}^{10}\text{B}$. There, the measured ratios involving the second group of excited states at $E^* \approx 5.1$ MeV and the third group of excited states at $E^* \approx 6$ MeV yield negative temperatures, in strong disagreement with the assumptions of a statistical primary distribution as embodied in the sequential decay calculation. Because there are large uncertainties in the calculation for the ratios of population probabilities for ${}^{11}\text{C}$, these ratios are not plotted.

In figure 27, we present β_{app} and T_{app} for groups of states in ${}^{13}\text{N}$ and ${}^{14}\text{N}$. The experimental and calculated population probabilities for the first group of states in ${}^{13}\text{N}$ are in agreement. The deviation for the second group is large. For ${}^{14}\text{N}$, the calculated population probabilities differ significantly from the measured ones, indicating that more feeding to the particle stable states is predicted than is observed. Somewhat better agreement for the population probabilities of ${}^{14}\text{N}$ excited states is obtained for $T_{\text{em}} = 3$ MeV. The measured ratios of population probabilities, on the other hand, are very consistent with calculations for $T_{\text{em}} = 4$ MeV.

Comparisons for groups of states in ^{16}O and ^{18}O are shown in fig. 28. Here, the overall agreement is somewhat worse for ^{16}O states than for the states of ^{18}O . Unlike the case for the lighter fragments, the second and third groups in ^{16}O are mixtures of states which decay to the ground state of ^{12}C and to the first excited state of ^{12}C . This reduces the sensitivity of population probabilities to the temperature making these states less suitable for temperature measurement.

To summarize these comparisons, roughly half of all the experimental population probabilities and one-third of the ratios of population probabilities deviate significantly from the predictions of the statistical calculations. The largest discrepancies in the ratios of excited state population probabilities are observed for ^{10}B . The largest discrepancies for the population probabilities were observed for ^{14}N .

VII. Angular Momentum Effects

The measured population probabilities are shown as the solid points and the results of the feeding calculations are shown as the shaded bands in figure 29 for the case of ^{10}B at an emission temperature of 4 MeV. These bands depict the range of values for n_i calculated when the spins and parities of states with incomplete nuclear structure information are randomly chosen according to primary distribution provided by the non-interacting shell model. Clearly, these calculations do not reproduce the non-monotonic dependence of n_i upon excitation energy. The uncertainty due to unknown spectroscopic information is much less than the observed enhancement of the experimental populations at $E^*=6$ MeV.

A. The Influence of Rotational Effects on the Population Probabilities

Angular momentum effects due to the rotation of the emitting system can cause the populations of high spin states of emitted fragments to be selectively enhanced. To explore

this issue, we have estimated the influence of rotational effects (1) by modifying the sequential decay calculations discussed previously, and (2) by applying the statistical theory of compound nuclear decay.

Sequential Decay Calculations : We introduce rotational effects into our sequential decay calculations by assuming⁷ the system rotates with collective velocity, ω , and approximating the primary population by

$$P \propto P_0(A, Z) \left(\sum_{m=-J}^J \exp\left\{-\frac{(m - \bar{m})^2}{2\sigma_m^2}\right\}\right) \exp(-E^*/T_{\text{em}}). \quad (28)$$

where m are the m -substates ($-J \leq m \leq +J$) of a given J . Here, \bar{m} and σ_m are parameters which describe the centroid and width of the m substate distribution for the fragment, and are chosen to be proportional to the rigid body moment of inertia, $\mathcal{I}(A, Z)$. Finally, to simplify our expressions, we express \bar{m} and σ_m in terms of the corresponding values for ^{12}C fragments :

$$\bar{m} = \bar{m}_{12\text{C}}(A/12)^{5/3} \quad \text{and} \quad \sigma_m = (\sigma_m)_{12\text{C}}(A/12)^{5/3} \quad (29)$$

where $\bar{m}(^{12}\text{C})$ and $\sigma_m(^{12}\text{C})$ are the appropriate centroid and width parameters for ^{12}C fragments.

The calculations were performed for many different values of $\bar{m}_{12\text{C}}$ and $(\sigma_m)_{12\text{C}}$. For each set of parameters $\bar{m}_{12\text{C}}$ and $(\sigma_m)_{12\text{C}}$, $P_0(A, Z)$ was adjusted to make the calculated particle stable yields consistent with the measured ones. The calculated population probabilities most similar to the measured ones were obtained for $\bar{m}_{12\text{C}} = 6$, $(\sigma_m)_{12\text{C}} = 2.5$ and $T_{\text{em}} = 4$ MeV. As indicated by the solid line in figure 30, the populations of high spin states are significantly enhanced for this choice of parameters, however, the enhancement for the triplet of high spin states ($J = 2, 3, 4$) at $E_i^* = 6$ MeV can not be reproduced without simultaneously overpredicting the population of the high spin state ($J = 4$) at $E_i^* = 6.56$ MeV and the spin

doublet ($J = 3, 2$) at $E_i^* = 9.0$ MeV. In this respect, the inclusion of rotational effects does not improve the agreement with the experimental data.

Compound Nuclear Decay : Recently, it has been suggested⁷⁰ that the influence of rotational effects on the population probability may be easily explored in the approximation of the compound nucleus emission.⁷¹ In the statistical theory of the compound nucleus, the yield Y_i of an excited state of an emitted fragment can be written as :⁷²

$$Y_i = C_0 \sum_{l=0}^{\infty} \sum_{Z=|I_p-l|}^{I_p+l} \sum_{I_D=|Z-I_i|}^{Z+I_i} \int dE_D^* \rho(E_D^*, I_D) T_l(E_p^* + Q_{g.s.} - E_i^* - E_D^*). \quad (30)$$

Here C_0 is a factor independent of the spin and excitation energy of the excited state of the emitted fragment, l is the orbital angular momentum, Z is the channel spin, I_p and E_p^* are the spin and excitation energy of the parent nucleus, I_D and E_D^* are the spin and excitation energy of the daughter nucleus, I_i and E_i^* are the spin and excitation energy of the emitted fragment and $Q_{g.s.}$ is the ground state Q -value for the decay. $\rho(E_D^*, I_D)$ is the level density of the daughter nucleus and T_l is the transmission coefficient for the emitted fragment.

For the purposes of these illustrative calculations, the level density of the daughter nucleus can be written in an exponential form⁷³ which is approximately valid for the range of temperatures considered here :

$$\rho(E_D^*, I_D) = C (2I_D + 1) \exp\left(\frac{E_D^*}{T_D} - \frac{E_{rot}}{T_D}\right) \quad (31)$$

where C is a constant and T_D is the temperature of the daughter nucleus :

$$T_D = \sqrt{\frac{8E_D^*}{A_D}} \quad (32)$$

where we have taken the level density parameter $a = 8$ (MeV)⁻¹, and we approximate E_D^* by

$$E_D^* = E_p^* + Q_{g.s.} - E_i^* - V_{coul}(R_{D_i}), \quad (33)$$

where $V_{\text{coul}}(R_{D_i})$ is the Coulomb potential when the fragment and daughter nucleus are separated by a distance $R_{D_i} = 1.2(A_D^{1/3} + A_i^{1/3})$. E_{rot} is the rotational energy associated with the daughter nucleus and is approximated by,

$$E_{\text{rot}} = (\hbar)^2 \frac{(I_D + \frac{1}{2})^2}{2\mathcal{I}_D} \quad (34)$$

where \mathcal{I}_D is the moment of inertia of the daughter nucleus. For simplicity, we assume a rigid body moment of inertia $\mathcal{I}_D = 2/5 m_D R_D^2$ where m_D and $R_D = 1.2A_D^{1/3}$ (fm) are the mass and radius of the daughter nucleus. We also assumed a sharp cut-off transmission coefficient T_l given by

$$T_l(E_p^* + Q_{\text{g.s.}} - E_i^* - E_D^*) = \theta(E_p^* + Q_{\text{g.s.}} - E_i^* - E_D^* - V_{\text{coul}}(R_\mu) - \frac{\hbar^2(l + \frac{1}{2})^2}{2\mu R_\mu^2}). \quad (35)$$

where $\mu = m_D m_i / (m_D + m_i)$ is the reduced mass for the system consisting of the daughter nucleus plus an emitted fragment of mass m_i .

The measured quantity in our experiment is the population probability, which is defined as

$$n_i = \frac{Y_i}{2I_i + 1}. \quad (36)$$

This quantity must be calculated. If one combines the information given above and integrates over energy, an explicit expression for n_i can be obtained in the limit of full spin coupling :

$$n_i = B(I_P) \frac{e^{-E_i^*/T_D}}{2I_i + 1} \sum_{l=0}^{\infty} \sum_{Z=|I_P-l|}^{I_P+l} \sum_{I_D=|Z-I_i|}^{Z+I_i} (2I_D + 1) \exp[-\{ \frac{(l + \frac{1}{2})^2 \hbar^2}{2\mu R_{D_i}^2} + \frac{(I_D + \frac{1}{2})^2 \hbar^2}{2\mathcal{I}_D} \} / T_D]. \quad (37)$$

Here $B(I_P)$ is a constant which, like C_0 , is independent of spin and excitation energy of the fragment, but could depend on the spin of the parent nucleus. Values for n_i were calculated for the excited states of ^{10}B assuming $I_p = 25, 50, 75$ and 100 , assuming a mass $A_p = 118$,

charge $Z_p = 50$, and excitation energy $E_p^* = 200$ MeV for the parent nucleus. The overall normalization constant $B(I_p)$ for the calculated values of n_i was determined at each value of I_p by minimizing the function χ_ν^2

$$\chi_\nu^2 = \frac{1}{N_{\text{point}} - 1} \sum_{i=1}^{N_{\text{point}}} \frac{(n_{\text{exp},i} - n_{\text{cal},i})^2}{\sigma_{\text{exp},i}^2} \quad (38)$$

where N_{point} is the total number of data points, $n_{\text{exp},i}$ and $n_{\text{cal},i}$ are the experimental and calculated values of the population probabilities, respectively, and $\sigma_{\text{exp},i}$ is the experimental uncertainty. The results are shown in figure 31 along with the experimental values of n_i . Values of $\chi_\nu^2 = 2.4, 1.8, 1.5, 1.7$ were obtained for $I_p = 25, 50, 75, 100$ respectively. Thus the agreement with experimental data is improved slightly for larger I_p . It can be seen that larger values of the parent nucleus I_p lead to larger enhancements in the populations of high spin states of the emitted ^{10}B nuclei. Values of $I_p = 75$ and 100 show enhanced populations for high spin states at $E_i^* \approx 6.0, 6.6,$ and 8.9 MeV, but the effects are nevertheless small compared to the experimental variations in n_i . Larger rotational effects are predicted for larger values of I_p , but values of I_p greater than $I_p = 88$ are inconsistent with the stability criterion for a metastable equilibrated compound nucleus as predicted by the liquid drop model. Further calculations are necessary to determine whether larger effects can be predicted by non-compound emission models. The calculations suggest, however, that it may be difficult to enhance the population of group of states at $E_i^* = 6.0$ MeV by rotational effects without likewise enhancing the high spin state at $E_i^* = 6.56$ MeV or the high spin doublet at $E_i^* \approx 8.9$ MeV.

B. Decay Angular Distributions

Additional information about the importance of rotational effects can be obtained from the measurements sensitive to the spin alignment of the emitted IMF's. Such spin alignment

effects can be explored by the measurement of the decay angular distributions for the particle unstable IMF's. Previous measurements of the spin alignments for the decay of ${}^6\text{Li} \rightarrow \alpha + d$ are consistent with a vanishing spin alignment of the excited ${}^6\text{Li}$.³²

Angle conventions used for investigating the decay angular correlations are shown in Figure 32. The unit vector \hat{n}_\perp defines the reaction normal which is in the direction perpendicular to the reaction plane defined by the beam axis and the momentum of the particle unstable fragment. Here, θ_d is defined to be the polar angle in the center of mass between the reaction normal \hat{n}_\perp and the velocity \vec{v}_α of the outgoing α -particle defined in this frame of the unstable fragment. In terms of the relative momentum \vec{q} , the total momentum \vec{P} , and the beam velocity \vec{v}_{beam} one has,

$$\theta_d = \cos^{-1} \frac{\vec{v}_\alpha \cdot (\vec{v}_{\text{beam}} \times \vec{v}_{\text{c.m.}})}{|\vec{v}_\alpha| |\vec{v}_{\text{beam}} \times \vec{v}_{\text{c.m.}}|} = \cos^{-1} \frac{\vec{q} \cdot (\vec{v}_{\text{beam}} \times \vec{P})}{|\vec{q}| |\vec{v}_{\text{beam}} \times \vec{P}|}, \quad (39)$$

The azimuthal angle ϕ_d between the projection of the vector \vec{v}_α on the reaction plane and the direction of the total momentum of the ${}^{10}\text{B}$ nucleus can be defined by

$$\phi_d = \cos^{-1} \frac{\vec{q} \cdot \vec{P}}{|\vec{q}| |\vec{P}| \sin \theta_d} \quad \text{if } \sin \theta_d \neq 0. \quad (40)$$

The distributions, ϕ_d and θ_d explore correlations in the reaction plane and correlations with respect to the reaction normal, respectively.

Figure 33 shows relative energy spectra for the decay ${}^{10}\text{B} \rightarrow \alpha + {}^6\text{Li}$ for different gates in the polar angle θ_d with respect to the reaction normal. The solid curve in the center panel for $\theta_d = 81^\circ - 100^\circ$ shows a best fit to the data for this angle gate assuming the dashed curve for the background. Using the population probabilities and background parameters obtained from this fit to the excitation energy spectra for $\theta_d = 80^\circ - 100^\circ$, the excitation energy spectra were calculated for all the values of θ_d using the appropriate efficiency functions calculated for the other polar angle gates. The solid and dotted curves in the other panels of figure

33 show the corresponding calculations for the relative energy spectra and backgrounds, respectively. The experimental data are reasonably well reproduced by this extrapolation for all cases, indicating that the same values of the relative populations can roughly account for the relative energy spectra regardless of θ_d . A similar analysis (not shown) performed for different gates on the azimuthal angle ϕ_d did not reveal a sizable anisotropy. Both the analysis suggest that any anisotropy in the decay angular distribution for ^{10}B must be small. Analysis of the $^6\text{Li} \rightarrow \alpha + d$ correlations (not shown) were also consistent with a vanishing anisotropy in the decay angular distributions.

C. Comparison with Statistical Calculations

More precise determinations of the decay angular distributions for ^{10}B were obtained by fitting each of the relative energy spectra in Fig. 33 and the corresponding spectra for the ϕ_d gates to obtain n_i as a function of θ_d and ϕ_d . Uncertainties in the extracted population probabilities n_i were estimated using different assumptions for the background and by considering possible uncertainties in the efficiency function. Angular correlations were extracted for the first three groups of α -unstable states of ^{10}B corresponding to excitation energies of 4.66 – 4.92 MeV, 5.0 – 5.26 MeV, 5.66 – 6.36 MeV respectively. In figures 34 and 35, we present the decay angular correlation as a function of θ_d and ϕ_d respectively. These angular correlations were normalized to average values of unity. The excitation energies and spins of the states which contribute to different groups are indicated in the figures. This more detailed comparison shows small anisotropy in the angular correlations for the first state and negligible anisotropy for the second and third groups of states.

The decay angular distributions were calculated using the statistical compound nuclear model as discussed before. In these estimates, the m -substate populations were calculated assuming the fragments were emitted from a compound nucleus whose spin is perfectly

aligned along the reaction normal. Within this approximation, the population for each m -substate of the emitted fragment is given by

$$P_i(m_i) = \sum_{l, m_i, Z, \nu, I_D, m_D} e^{-E_i^*/T_D} \langle I_i m_i I_D m_D | Z \nu \rangle^2 \langle l m_i Z \nu | I_p I_p \rangle^2 \\ \times (2I_D + 1) \exp\left[-\left\{\frac{(l + \frac{1}{2})^2 \hbar^2}{2\mu R_\mu^2} + \frac{(I_D + \frac{1}{2})^2 \hbar^2}{2I_D}\right\}/T_D\right] \quad (41)$$

The various quantities are as defined in Eq. 33-40. One must now consider the decay of these aligned fragments. For decay with a single open channel, this is given by

$$\frac{dP_f}{d\Omega} = \sum_{l_f, m_f, Z_f, \nu_f, m_i, m_1, m_2} \langle I_1 m_1 I_2 m_2 | Z_f \nu_f \rangle^2 \langle l_f m_f Z_f \nu_f | I_i m_i \rangle^2 \\ \times |Y_{l_f m_f}(\Omega)|^2 \frac{T_{\beta l_f Z_f}^{I_i}}{\sum T_{\gamma l_f' Z_f''}^{I_i}} [P_i(m_i)]. \quad (42)$$

Here the subscript i refers to the values for ^{10}B fragment, the subscripts 1 and 2 identify the angular momentum quantum numbers for the emitted particles α and ^6Li ; l_f and m_f are the orbital angular momentum and corresponding m -substate value for the α -decay of ^{10}B ; Z_f and ν_f are the channel spins and the channel spin m -substate values; and $P_i(m_i)$ is calculated according to equation (41). The transmission coefficients T^{I_i} are obtained from the optical potential calculations. Decay angular distributions were calculated with equation (42) for $^{10}\text{B} \rightarrow \alpha + ^6\text{Li}$ using the parent spins $I_p = 25, 50, 75, 100$. The results for the θ_a -angular correlations for the first ($J = 3^+$, $E^* = 4.77$ MeV excited state) are shown in figure 36. The small anisotropy seen for the first group is consistent with the angular momentum I_p of an aligned compound nucleus between 50 and 75. This result offers some positive evidence for the importance of rotational effects. This comparison, however, cannot be used to place stringent upper limits on the angular momentum of the system, since the decay angular distributions of the systems can lead to similar decay angular correlations provided the initial spin is poorly aligned with the reaction normal.

VIII. SUMMARY AND CONCLUSION

In this paper, we report measurements, with a position sensitive hodoscope, of the relative populations of 40 groups of particle unstable states of Li, Be, B, C, N and O fragments emitted in ^{14}N induced reaction on ^{nat}Ag at $E/A = 35$ MeV. Extensive calculations were also performed to predict the relative populations of these same states while taking into account the sequential feeding from heavier particle unstable nuclei. In global comparisons involving all the population probabilities and ratios of population probabilities, the best agreement between calculated and measured quantities occurred at $T_{\text{em}} = 3 - 4$ MeV. The emission temperature extracted for ^5Li fragments is slightly higher ($T_{\text{em}} \approx 4$ MeV), and is consistent with the systematic incident energy dependence of emission temperatures extracted from ^5Li fragments previously reported.

Even for an emission temperature $T_{\text{em}} = 3 - 4$ MeV, however, the magnitude of the χ^2 functions used in the global comparisons were rather large, indicating a significant discrepancy between measured and calculated quantities. Indeed, the disagreement between calculated and measured quantities was substantial for roughly half of the population probabilities and one third of the ratios of population probabilities. The relative populations of the excited states were studied in detail for excited ^{10}B nuclei, where some of the largest discrepancies between the calculated and measured population probabilities were observed. Calculations were performed to explore whether rotational effects could account for this deviation when imbedded in a statistical description. While the inclusion of rotational effects did indeed alter the population probabilities, it did not account for the effects observed experimentally and in some respects, the trends induced by rotation differed quantitatively from the trends observed experimentally. Measurements of the decay angular distributions of ^{10}B fragments did indicate the existence of small anisotropy of these decay angular distributions,

offering positive evidence for the existence of rotational effects.

At the present time, the discrepancies between calculated and measured population probabilities are not understood; several possible explanations can be offered.

- 1) Since the masses of the fragments considered in our analysis are close to the mass of the projectile, simple non-thermal production mechanisms cannot be excluded. These mechanisms may not thermally populate the fragment excited states. This possibility can be explored via additional measurements with heavier or lighter projectile nuclei.
- 2) There is a possibility that the spins or branching ratios of some of the states analyzed in this paper may be incorrectly assigned in the literature. The extracted populations are sensitive to this spectroscopic information. Incorrect spectroscopic information will result in an incorrect extraction of the corresponding population probabilities. For the states of ^{10}B where large discrepancies were observed, however, the relevant spectroscopic information appears well established and the discrepancies appear to be real.
- 3) Some of the measured peaks could contain background peaks from three body decays or from the decays to daughter fragments in particle stable excited states. Additional measurements with improved excitation energy resolution could help to clarify this issue.
- 4) Some heavier particle unstable nuclei could decay sequentially to the excited intermediate mass fragments measured in this experiment with branching ratios that differ significantly from the ones predicted in the Hauser-Feshbach model of statistical decay. This would lead to an enhancement or a depletion of the populations of selected excited states.
- 5) It is conceivable that the excited states of the emitted fragments could be thermally populated at a higher density transition state where the energies of the levels differ significantly from their asymptotic values. If the evolution of the system to zero density is adiabatic, the populations of these levels could be preserved while the ordering of the levels could be changed leading to the appearance of non-thermal populations of the isolated fragments.

Whether these discrepancies would be less in experiments with heavier or lighter beams where simple fragment production modes are suppressed, is an open question which should be addressed by future investigations.

ACKNOWLEDGEMENT

This work was supported by the U.S. National Science Foundation under Grant No. PHY 86-11210 and by the U.S. Department of Energy under Contract No. DE-AC02-81ER-40007. One of authors (W.G.L.) acknowledges the receipt of the U.S. Presidential Young Investigator Award.

APPENDIX

Expression for the Excitation Energy Spectrum

To find an expression for the excitation energy spectrum, $|dn(E^*)/dE^*|_c$, we must consider the modifications of the phase space density of the decay products due to their mutual interactions. Following ref. 74, we consider the interactions of two spinless non-identical particle. The density of two particle states containing one of each of the decay products can be written as

$$\rho_{12}(\vec{p}_1, \vec{p}_2) = \rho_T(\vec{P}) \cdot \rho_r(\vec{q}) \quad (43)$$

where $\rho_T(\vec{P})$ is the density of states associated with the motion of the center-of-mass of these particles, and $\rho_r(\vec{q})$ is the density of states per unit volume in momentum space for the relative motion of the two particles. Here \vec{p}_1, \vec{p}_2 are the momenta of the two detected particles, \vec{q} is the relative momentum and \vec{P} is the total momentum. The density of states for center of mass motion $\rho_T(\vec{P})$ is not affected by the mutual interaction of the two decay products. We need consider only modifications of the density of states for the relative motion

$\rho_r(\vec{q})$. If one considers the number of states in a box of volume V about the center of mass of the two particles and requires the relative wave function to vanish at the boundaries of the box, one can obtain

$$\rho_r(\vec{q}) = (\rho_0(q) + \Delta\rho(q))/4\pi q^2 \quad (44)$$

$$\text{where} \quad \rho_0(q) = \frac{4\pi V}{h^3} q^2 \quad (45)$$

is the density of states per unit relative momentum for non-interacting spinless particles, and

$$\Delta\rho(q) = \frac{1}{\pi} \sum_l (2l + 1) \frac{\partial \delta_l}{\partial q} \quad (46)$$

describes the modification of the phase density due to the interactions between the two particles.⁷⁵ In this expression, δ_l is the scattering phase shift for the partial wave with orbital angular momentum l . Additional quantum numbers are in general associated with the phase shifts. Each of these phase shifts can contribute to $\Delta\rho$. If one assigns an index i to each phase shift, one can generalize eq. (46) for particles with non-zero spins :

$$\Delta\rho(q) = \frac{1}{\pi} \sum_i (2J_i + 1) \frac{\partial \delta_i}{\partial q}. \quad (47)$$

If the two particles are in contact with a thermal reservoir with a temperature T , the phase space will be populated in accordance with the Boltzmann factor $\exp(-E^*/T)$. For the phase space of relative motion, one expects a probability distribution per unit relative momentum which has the form⁷⁴ :

$$4\pi q^2 \cdot \rho_r(\vec{q}) \exp\left(-\frac{q^2}{2\mu T}\right) = \rho_0(q) \exp\left(-\frac{q^2}{2\mu T}\right) + \Delta\rho(q) \exp\left(-\frac{q^2}{2\mu T}\right), \quad (48)$$

where μ is the reduced mass of the two body decay channel. The latter term in eq. (48) arises from the interactions between the two fragments. If one isolates the portion $\delta_{i,\text{res}}$ of the

total phase shift δ_i which corresponds to the modifications of the two particle phase space due to long lived resonant interactions between the two fragments, one obtains an expression for the population of resonant excited states. For a system with a single open channel, the expression for the decay spectrum of the excited nucleus becomes

$$\left| \frac{dn(E^*)}{dE^*} \right|_c = C_{\text{stable}} \sum_i \exp\left(-\frac{E^*}{T}\right) \frac{1}{\pi} (2J_i + 1) \frac{\partial \delta_{i,\text{res}}}{\partial E^*}, \quad (49)$$

where C_{stable} is a constant fixed by the requirement that $\int^\infty dE^* |dn(E^*)/dE^*|_c$ is the total decay yield into channel c divided by the total yield for the corresponding particle-stable nucleus. To proceed further, we need an expression for $\partial \delta_{i,\text{res}}/\partial E^*$, allowing for the possibility that more than one decay channel may be open.

Most of the phase shifts for the formation of particle unstable light nuclei are already experimentally known. Many are parameterized using the R -matrix theory of nuclear reactions.⁷⁶ We now recapitulate the essential elements of this theory. Central to this theory is the R -matrix, $R_{\nu\nu'}$ which is the multichannel analog to the logarithmic derivative of the radial wave function ψ_ν . The symbol ν is a shorthand which denotes the many quantum numbers (e.g., c , l , m , channel spins etc.) required to completely specify the decay channel. The index c designates two specific daughter isotopes produced by the decay of the particle unstable nucleus. Due to the existence of particle unbound states in the fragment, $R_{\nu\nu'}$ is often expressed as a sum of poles :

$$R_{\nu\nu'} = \sum_\lambda \frac{\gamma_{\lambda\nu} \gamma_{\lambda\nu'}}{E_\lambda - E^*} \quad (50)$$

corresponding to resonances at $E^* \approx E_\lambda$. The terms $\gamma_{\lambda\nu}$ are the reduced widths which contain information about coupling of the resonance λ to the decay channel ν . In principle, the locations of the poles E_λ correspond to the energy eigenvalues of eigenstates $\Psi_{\lambda\nu}(\vec{r}) = \text{const.} \cdot \psi_{\lambda\nu}(r) \cdot Y_{l,m}(\theta, \phi)$ which satisfy Schrodinger equation at $r < a_\nu$ in addition

to a boundary condition

$$a_\nu \left. \frac{d\psi_{\lambda\nu}(r)}{dr} \right|_{r=a_\nu} = B_\nu \psi_{\lambda\nu}(a_\nu), \quad (51)$$

at the channel radius a_ν , with the boundary value B_ν .

Within the R -matrix theory, the scattering matrix $S_{\nu\nu'}$ is given by a matrix expression

$$\mathbf{S} = (\mathbf{ka})^{1/2} \mathbf{O}^{-1} [\mathbf{1} - \mathbf{R}(\mathbf{L} - \mathbf{B})]^{-1} [\mathbf{1} - \mathbf{R}(\mathbf{L}^* - \mathbf{B})] \mathbf{I} (\mathbf{ka})^{-1/2} \quad (52)$$

where

$$\begin{aligned} (\mathbf{ka})^{\frac{1}{2}} &= (k_\nu a_\nu)^{\frac{1}{2}} \delta_{\nu\nu'}, \\ \mathbf{O}^{-1} &= O_\nu^{-1} \delta_{\nu\nu'}, \\ \mathbf{L} &= L_\nu \delta_{\nu\nu'}, \\ \mathbf{B} &= B_\nu \delta_{\nu\nu'}, \\ \text{and } \mathbf{I} &= I_\nu \delta_{\nu\nu'} \end{aligned} \quad (53)$$

are matrix representations for channel dependent quantities. Here, k_ν is the channel wave number, O_ν and I_ν are the outgoing and incoming solutions of the radial equation for channel ν , and

$$L_\nu = a_\nu \frac{O'_\nu}{O_\nu} = a_\nu \frac{(I'_\nu)^*}{(I_\nu)^*} \quad (54)$$

is the corresponding logarithmic derivative. Values for a_ν and B_ν are not apriori specified by the R -matrix theory. In practice, for charged particle decay channels, a_ν is often chosen sufficiently large that the outgoing and incoming radial wave functions O_ν and I_ν can be accurately approximated by Coulomb wave functions. While the choices for B_ν and a_ν are not especially significant, they do define a convention which must be consistently followed because B_ν and a_ν are coupled to the values of E_λ and $\gamma_{\lambda\nu}$ obtained from fitting the equation

(52) to low energy scattering data. In other words, the parameters of a resonance are not completely specified by E_λ and $\gamma_{\lambda\nu}$, and the conventions for B_ν and a_ν must also be followed when fitting R -matrix expression to the experimental data.

Little can be gained by elaborating on the R -matrix theory. We now address specific limiting cases which are relevant to the states measured in this work.

A. One-level approximation

When E^* is near an isolated resonance at energy E_λ , the R -matrix is often approximated by

$$R_{\nu\nu'} = R_{\nu\nu'}^\lambda = \frac{\gamma_{\lambda\nu} \cdot \gamma_{\lambda\nu'}}{E_\lambda - E^*} \quad (55)$$

where the pole reflects the influence of the resonance at $E^* = E_\lambda$. Substituting equation (55) into (52), the one-level formula for the S -matrix becomes

$$S_{\nu\nu'} = \exp[i(\omega_\nu + \omega_{\nu'} - \phi_\nu - \phi_{\nu'})] \left[\delta_{\nu\nu'} + \frac{i(\Gamma_{\lambda\nu}\Gamma_{\lambda\nu'})^{1/2}}{E_\lambda + \Delta_\lambda - E^* - \frac{i}{2}\Gamma_\lambda} \right] \quad (56)$$

where ϕ and ω are the hard sphere and Coulomb phase shifts, respectively, and $\delta_{\nu\nu'}$ is the Kronecker delta function. The width $\Gamma_{\lambda\nu}$ and the energy shift $\Delta_{\lambda\nu}$ can be expressed in terms of the reduced width $\gamma_{\lambda\nu}^2$ as follows

$$\Gamma_{\lambda\nu} = 2P_\nu\gamma_{\lambda\nu}^2, \quad \Gamma_\lambda = \sum_\nu \Gamma_{\lambda\nu} \quad (57)$$

$$\Delta_\lambda = - \sum_\nu (S_\nu - B_\nu)\gamma_{\lambda\nu}^2. \quad (58)$$

Here Γ_λ is the total width of the resonance. P_ν is called the penetration factor which is related to the probability that the particles in the exit channel escape from the interaction region. Mathematically P_ν and S_ν can be expressed in terms of F and G , the regular and irregular solutions of the radial wave equation in the external region and their derivatives,

all evaluated at channel radius a_ν . One obtains

$$P_\nu = \rho_\nu A_\nu^{-2} |_{r=a_\nu} \quad \text{and} \quad S_\nu = \rho_\nu A_\nu^{-1} (\partial A_\nu / \partial \rho_\nu) |_{r=a_\nu} \quad (59)$$

where $A_\nu^2 = F_\nu^2 + G_\nu^2$, and $\rho_\nu = k_\nu r$

where F and G are the regular and irregular Coulomb wave functions. The inclusion of the factor Δ_λ in equation (56) has the consequence that the level energy E_λ is different from the resonance energy E_{res} of the level λ and is given by⁴⁷ :

$$E_{\text{res}} = E_\lambda + \Delta_\lambda. \quad (60)$$

From equation (56) it is clear that the S-matrix has off-diagonal terms which mix channels ν and ν' . To obtain the modifications of the phase space density due to unbound resonances, the position of the S-matrix within the square bracket of Eq. (56) must be diagonalized. The phases involving the Coulomb and hard sphere phase shifts can, in principle, be eliminated by an alternate choice of incoming and outgoing channel wave functions, and we drop it in the ensuing discussion. In the diagonal representation, the S-matrix in the resonant channel becomes

$$S = \exp(2i\delta_{\lambda,\text{res}}) = \frac{E_\lambda + \Delta_\lambda - E^* + \frac{i}{2}\Gamma_\lambda}{E_\lambda + \Delta_\lambda - E^* - \frac{i}{2}\Gamma_\lambda}. \quad (61)$$

Near E_{res} , this single resonance makes the dominant contribution to the partial wave decomposition in eq. (49). Let us denote the contribution to $\left| \frac{dn}{dE^*} \right|_\nu$ from this single term as

$\left| \frac{dn_\lambda}{dE^*} \right|_\nu$. One can easily obtain a thermal expression for the excitation energy distribution of this isolated level by inserting eq. (61) into eq. (49) to obtain

$$\begin{aligned} \frac{dn_{\lambda,\text{tot}}(E^*)}{dE^*} &= C_{\text{stable}} \exp\left(-\frac{E^*}{T}\right) \frac{(2J_\lambda + 1)}{\pi} \\ &\times \frac{\Gamma_\lambda/2}{(E_\lambda + \Delta_\lambda - E^*)^2 + \frac{1}{4}\Gamma_\lambda^2} \left[1 - \frac{d\Delta_\lambda}{dE^*} + \frac{E_\lambda + \Delta_\lambda - E^*}{\Gamma_\lambda} \frac{d\Gamma_\lambda}{dE^*} \right] \quad (62) \end{aligned}$$

In general, ν will not be the resonant channel in the diagonal representation and this state will decay to all available channels ν . The branching ratio which governs the decay to the original channel ν is equal to the absolute value of the coefficient which describes the contribution to the resonant channel from the ν th original channel. Using the S matrix of the eq. (61), we can solve for the given channels of the S-matrix to obtain the branching ratio BR_ν for the decay of this state to ν th channel

$$BR_\nu = \frac{\Gamma_{\lambda\nu}}{\Gamma_\lambda}. \quad (63)$$

The excitation energy spectrum for channel ν is obtained by multiplying the excitation energy spectrum in eq. (62) by this branching ratio. In most cases, a given pair of final decay products, c , are emitted with a unique partial wave l_c and channel spin z_c . Thus by specifying c for resonance λ , ν is completely defined and therefore becomes redundant.

Taking this into account, we can then write decay spectrum for the channel c as

$$\left| \frac{dn_\lambda(E^*)}{dE^*} \right|_c = N_\lambda \exp\left(-\frac{E^*}{T}\right) \frac{(2J_\lambda + 1)}{\pi} \times \frac{\Gamma_{\lambda c}/2}{(E_\lambda + \Delta_\lambda - E^*)^2 + \frac{1}{4}\Gamma_\lambda^2} \left[1 - \frac{d\Delta_\lambda}{dE^*} + \frac{E_\lambda + \Delta_\lambda - E^*}{\Gamma_\lambda} \frac{d\Gamma_\lambda}{dE^*} \right], \quad (64)$$

where the constant C_{stable} has been replaced by another constant N_λ which depends specifically on the level λ . For nuclei with more than one isolated level, the contribution from the various levels can be seen to be $\left| \frac{dn}{dE^*} \right|_c = \Sigma_\lambda \left| \frac{dn_\lambda}{dE^*} \right|_c$. In the absence of sequential feeding from heavier particle unstable nuclei, the value of N_λ should be equal C_{stable} for all states in the summation. Values for N_λ for individual excited states obtained from fits to the experimental data, are given in section IV.

Where the resonance parameters Γ_λ and Δ_λ depend only weakly on the energy, a Breit-Wigner description of the S-matrix is frequently used. In this case, Γ_λ and Δ_λ are

constants, and $|dn_\lambda/dE^*|_c$ becomes

$$\left| \frac{dn_\lambda(E^*)}{dE^*} \right|_c = N_\lambda \exp\left(-\frac{E^*}{T}\right) \frac{(2J_\lambda + 1)}{\pi} \frac{\Gamma_\lambda/2}{(E_{\text{res}} - E^*)^2 + \frac{1}{4}\Gamma_\lambda^2} \frac{\Gamma_{\lambda c}}{\Gamma_\lambda}. \quad (65)$$

where E_{res} is the resonance energy for the level λ .

B. The Two-level approximation

The analysis of overlapping levels with the same spins and parities is more complicated. For our purposes, however, it is only necessary to obtain the appropriate expressions for the case of two overlapping levels and two open decay channels. The R -matrix for this case is given by (ref. [76] page 329) :

$$R_{\nu\nu'} = \frac{\gamma_{1\nu}\gamma_{1\nu'}}{E_1 - E} + \frac{\gamma_{2\nu}\gamma_{2\nu'}}{E_2 - E}. \quad (66)$$

The relationship between R -matrix and S -matrix given in equation (52) can be written in the form

$$\mathbf{S} = \mathbf{\Omega}\mathbf{W}\mathbf{\Omega} \quad (67)$$

$$\text{where } \mathbf{\Omega} = \mathbf{I}^{1/2}\mathbf{O}^{-1/2} = \exp[i(\omega_\nu - \phi_\nu)]\delta_{\nu\nu'} \quad (68)$$

and the components of the matrix \mathbf{W} in the case of two levels with two open channels are

$$W_{11} = 1 + 2iP_1[R_{11} - L_2^0(R_{11}R_{22} - R_{12}^2)]d^{-1}, \quad (69)$$

$$W_{22} = 1 + 2iP_2[R_{22} - L_1^0(R_{11}R_{22} - R_{12}^2)]d^{-1}, \quad (70)$$

$$W_{12} = W_{21} = 2iP_1^{1/2}R_{12}P_2^{1/2}d^{-1}, \quad (71)$$

where

$$d = (1 - R_{11}L_1^0)(1 - R_{22}L_2^0) - L_1^0R_{12}^2L_2^0 \quad (72)$$

$$\text{with } L_\nu^0 = L_\nu - B_\nu = S_\nu + iP_\nu - B_\nu. \quad (73)$$

The indices 1 and 2 refer to channels 1 and 2 respectively.

Following our previous discussion, we adopt the factors of Ω in eq. (67) which can be eliminated by an alternative choice of incoming and outgoing channel wavefunctions. Thus, to find stationary wave solutions in both the channels, we need to solve the eigenvalue equation

$$\zeta \vec{a} = \mathbf{W} \vec{a} \quad (74)$$

for the eigenvectors \vec{a} and their corresponding eigenvalues ζ . This yields the two possible eigenvalues :

$$\zeta_1 = \frac{1}{2} \left\{ W_{11} + W_{22} - \sqrt{(W_{11} + W_{22})^2 - 4(W_{11}W_{22} - W_{12}W_{21})} \right\} \quad (75)$$

$$\zeta_2 = \frac{1}{2} \left\{ W_{11} + W_{22} + \sqrt{(W_{11} + W_{22})^2 - 4(W_{11}W_{22} - W_{12}W_{21})} \right\} \quad (76)$$

for the two levels considered. By substituting these eigenvalues in equation (74), the eigenvectors \vec{a} can be obtained. The branching ratios for the decay from one of the levels λ to channel $\nu(=1,2)$ are then

$$(\text{BR})_{\lambda,\nu=1} = \frac{|W_{12}|^2}{|\zeta_\lambda - W_{11}|^2 + |W_{12}|^2} \quad (77)$$

$$(\text{BR})_{\lambda,\nu=2} = \frac{|\zeta_\lambda - W_{11}|^2}{|\zeta_\lambda - W_{11}|^2 + |W_{12}|^2} \quad (78)$$

The two-level decay spectrum for the decay into channel ν is given by

$$\left| \frac{dn(E^*)}{dE^*} \right|_\nu = N \exp\left(-\frac{E^*}{T}\right) \frac{(2J+1)}{2\pi i} \left\{ \frac{1}{\zeta_1} \frac{d\zeta_1}{dE^*} (\text{BR})_{1\nu} + \frac{1}{\zeta_2} \frac{d\zeta_2}{dE^*} (\text{BR})_{2\nu} \right\} \quad (79)$$

where J is the spin of the levels considered. Here we use a single normalization constant N because the experimental data generally do not allow for a separate determination of the emission temperature T and also for two normalizations for two overlapping states with the same spin.

- a. Present address: Nevis Laboratories, Columbia University,
P.O. Box 137, Irvington, New York 10533.
- b. Present address: Department of Physics, Kyoto University,
Kyoto 606, Japan.
- c. Present address: Nuclear Physics Laboratory, University of Washington,
Seattle, WA 98195, USA.
- d. Present address: Physics Division, Lawrence Livermore National Laboratory,
Livermore, CA 94550, USA.
- e. Present address: Institut für Kernphysik, Universität Frankfurt,
D-6000 Frankfurt, Germany.

References

- ¹ Proceedings of the Symposium on Central Collisions and Fragmentation Processes,
ed. C.K. Gelbke, Nucl. Phys. A471, 1c-451c (1987).
- ² W.G. Lynch, Ann. Rev. Nucl. Sci. 37, 493 (1987); and references contained therein.
- ³ G. F. Bertsch and S. Das Gupta, Phys. Reports 160, 189 (1988); and references
contained therein.
- ⁴ C. K. Gelbke and D.H. Boal, Prog. Part. Nucl. Phys. 19, 33 (1987); and references
contained therein.
- ⁵ G. Bertsch and P.J. Siemens, Phys. Lett. 126B, 9 (1983).

- ⁶ T. J. Schlagel and V. R. Pandharipande, *Phys. Rev. C* **36**, 162 (1987).
- ⁷ K. Sneppen and L. Vinet, *Nucl. Phys. A***480**, 342 (1988).
- ⁸ D. H. Boal, J. N. Glosli, and C. Wicentowich *Phys. Rev. C* **40**, 601 (1989); *Phys. Rev. Lett.* **62**, 737 (1989).
- ⁹ J. A. Lopez and P.J. Siemens, *Nucl. Phys. A***431**, 728 (1984).
- ¹⁰ J. E. Finn, S. Agarwal, A. Bujak, J. Chuang, L. J. Gutay, A. S. Hirsch, R. W. Minich, N. T. Porile, R. P. Scharenberg, B. C. Stringfellow, and F. Turkot, *Phys. Rev. Lett.* **49**, 1321 (1982).
- ¹¹ H. R. Jaqaman, *Phys. Rev. C* **27**, 2782 (1983).
- ¹² L. G. Sobotka, M. L. Padgett, G. J. Wozniak, G. Guarino, A. J. Pacheco, L. G. Moretto, Y. Chan, R. G. Stokstad, I. Tserruya, and S. Wald, *Phys. Rev. Lett.* **51**, 2187 (1983).
- ¹³ L. G. Sobotka, M. A. McMahan, R. J. McDonald, C. Signarbieux, G. J. Wozniak, M. L. Padgett, J. H. Gu, Z. H. Liu, Z. Q. Yao, and L. G. Moretto, *Phys. Rev. Lett.* **53**, 2004 (1984).
- ¹⁴ W. A. Friedman and W. G. Lynch, *Phys. Rev. C* **28**, 16 (1983)., *ibid.* 950.
- ¹⁵ L. G. Moretto, *Nucl. Phys. A***247**, 211 (1975).
- ¹⁶ D. J. Fields, W. G. Lynch, C. B. Chitwood, C. K. Gelbke, M.B. Tsang, H. Utsunomiya, and J. Aichelin, *Phys. Rev. C* **30**, 1912 (1984).

- ¹⁷ D. J. Fields, W. G. Lynch, T. K. Nayak, M. B. Tsang, C. B. Chitwood, C. K. Gelbke, R. Morse, J. Wilczynski, T. C. Awes, R. L. Ferguson, F. Plasil, F. E. Obenshain, and G. R. Young *Phys. Rev. C* **34**, 536 (1986).
- ¹⁸ S. Ban-Hao and D. H. E. Gross, *Nucl. Phys. A* **437**, 643 (1985).
- ¹⁹ M. B. Tsang, C. B. Chitwood, D. J. Fields, C. K. Gelbke, D. R. Klesch, W. G. Lynch, K. Kwiatkowski, and V. E. Viola, Jr., *Phys. Rev. Lett.* **52**, 1967 (1984).
- ²⁰ M. B. Tsang, R. M. Ronningen, G. Bertsch, Z. Chen, C. B. Chitwood, D. J. Fields, C. K. Gelbke, W. G. Lynch, T. Nayak, J. Pochodzalla, T. Shea, and W. Trautmann, *Phys. Rev. Lett.* **57**, 559 (1986).
- ²¹ P. J. Siemens, and J. O. Rasmussen, *Phys. Rev. Lett.* **42**, 880 (1979).
- ²² G. Fai and J. Randrup, *Nucl. Phys. A* **381**, 557 (1982).
- ²³ D. H. E. Gross, L. Satpathy, Mang Ta-Chung, and M. Satpathy, *Z. Phys. A* **309**, 41 (1982).
- ²⁴ D. H. E. Gross, Zhang Xiao-ze, and Xu Shu-yan, *Phys. Rev. Lett.* **56**, 1544 (1986).
- ²⁵ J. Randrup and S. E. Koonin, *Nucl. Phys. A* **356**, 223 (1981).
- ²⁶ D.J. Morrissey, W. Benenson, E. Kashy, B. Sherrill, A.D. Panagiotou, R.A. Blue, R.M. Ronningen, J. van der Plicht, and H. Utsunomiya, *Phys. Lett.* **148B**, 423 (1984).
- ²⁷ D. J. Morrissey, W. Benenson, E. Kashy, C. Bloch, M. Lowe, R. A. Blue, R. M. Ronningen, B. Sherrill, H. Utsunomiya, and I. Kelson, *Phys. Rev. C* **32**, 877 (1985).

- ²⁸ H. M. Xu, D. J. Fields, W. G. Lynch, M. B. Tsang, C. K. Gelbke, M. R. Maier, D. J. Morrissey, J. Pochodzalla, D. G. Sarantites, L. G. Sobotka, M. L. Halbert, D. C. Hensley, D. Hahn, and H. Stocker, *Phys. Lett.* **182B**, 155 (1986).
- ²⁹ H. M. Xu, W. G. Lynch, C. K. Gelbke, M. B. Tsang, D. J. Fields, M. R. Maier, D. J. Morrissey, T. K. Nayak, J. Pochodzalla, D. G. Sarantites, L. G. Sobotka, M. L. Halbert, D. C. Hensley, *Phys. Rev. C* **40**, 186 (1989).
- ³⁰ J. Pochodzalla, W. A. Friedman, C. K. Gelbke, W. G. Lynch, M. Maier, D. Ardouin, H. Delagrange, H. Doubre, C. Gregoire, A. Kyanowski, W. Mittig, A. Peghaire, J. Peter, F. Saint-Laurent, Y. P. Viyogi, B. Zwieglinski, G. Bizard, F. Lefebvres, B. Tamain and J. Quebert, *Phys. Rev. Lett.* **55**, 177 (1985).
- ³¹ J. Pochodzalla, W. A. Friedman, C. K. Gelbke, W. G. Lynch, M. Maier, D. Ardouin, H. Delagrange, H. Doubre, C. Gregoire, A. Kyanowski, W. Mittig, A. Peghaire, J. Peter, F. Saint-Laurent, Y. P. Viyogi, B. Zwieglinski, G. Bizard, F. Lefebvres, B. Tamain, J. Quebert, *Phys. Lett.* **161B**, 256 (1985).
- ³² J. Pochodzalla, C. K. Gelbke, W. G. Lynch, M. Maier, D. Ardouin, H. Delagrange, H. Doubre, C. Gregoire, A. Kyanowski, W. Mittig, A. Peghaire, J. Peter, F. Saint-Laurent, B. Zwieglinski, G. Bizard, F. Lefebvres, B. Tamain, J. Quebert, Y. P. Viyogi, W. A. Friedman and D. H. Boal, *Phys. Rev. C* **35**, 1695 (1987).
- ³³ C. B. Chitwood, C. K. Gelbke, J. Pochodzalla, Z. Chen, D. J. Fields, W. G. Lynch, R. Morse, M. B. Tsang, D. H. Boal and J. C. Shillcock, *Phys. Lett.* **172B**, 27 (1986).
- ³⁴ Z. Chen, C. K. Gelbke, J. Pochodzalla, C. B. Chitwood, D. J. Fields, W. G. Lynch, and M. B. Tsang, *Phys. Lett.* **184B**, 280 (1987).

- ³⁵ Z. Chen, C. K. Gelbke, J. Pochodzalla, C.B. Chitwood, D.J. Fields, W. G. Gong, W. G. Lynch, and M. B. Tsang, Nucl. Phys. A**473**, 564 (1987).
- ³⁶ Z. Chen, C. K. Gelbke, W. G. Gong, Y. D. Kim, W. G. Lynch, M. R. Maier, J. Pochodzalla, M. B. Tsang, F. Saint-Laurent, D. Ardouin, H. Delagrangé, H. Doubre, J. Kasagi, A. Kyanowski, A. Peghaire, J. Peter, E. Rosato, G. Bizard, F. Lefebvres, B. Tamain, J. Quebert and Y. P. Viyogi, Phys. Rev. C **36**, 2297 (1987).
- ³⁷ D. Fox, D. A. Cebra, J. Karn, C. Parks, A. Pradhan, A. Vander Molen, J. van der Plicht, G. D. Westfall, W. K. Wilson and R. S. Tickle, Phys. Rev. C **38**, 146 (1988).
- ³⁸ F. Deak, A. Kiss, Z. Seres, A. Galonsky, C. K. Gelbke, L. Heilbronn, W. Lynch, T. Murakami, H. Schelin, M. B. Tsang, B. A. Remington, J. Kasagi, Phys. Rev. C **39**, 733 (1989).
- ³⁹ T. K. Nayak, T. Murakami, W. G. Lynch, K. Swartz, D. J. Fields, C. K. Gelbke, Y. D. Kim, J. Pochodzalla, M. B. Tsang, F. Zhu, and K. Kwiatkowski, Phys. Rev. Lett. **62**, 1021 (1989).
- ⁴⁰ T. Murakami, T. K. Nayak, W. G. Lynch, K. Swartz, Z. Chen, D. J. Fields, C. K. Gelbke, Y. D. Kim, M. R. Maier, J. Pochodzalla, M. B. Tsang, H. M. Xu, and F. Zhu, Nucl. Instrum. Method Phys. Res. A**275**, 112 (1989).
- ⁴¹ D. E. Fields, K. Kwiatkowski, D. Bonser, R. W. Viola, V. E. Viola, W. G. Lynch, J. Pochodzalla, M. B. Tsang, C. K. Gelbke, D. J. Fields, and S. M. Austin, Phys. Lett. **220B**, 356 (1989).
- ⁴² F. Ajzenberg-Selove, Nucl. Phys. A**1**, 1 (1979); Nucl. Phys. A**375**, 1 (1982); Nucl. Phys. A**413**, 1 (1984); Nucl. Phys. A**433**, 1 (1985); Nucl. Phys. A**449**, 1 (1986); Nucl. Phys. A**460**, 1 (1986); Nucl. Phys. A**475**, 1 (1987); Nucl. Phys. A**490**, 1 (1988).

- ⁴³ J. Pochodzalla, C. K. Gelbke, C. B. Chitwood, D. J. Fields, W. G. Lynch, M. B. Tsang, and W. A. Friedman, *Phys. Lett.* **175B**, 275 (1986).
- ⁴⁴ R. J. Spiger and T. A. Tombrello, *Phys. Rev.* **163**, 964 (1967).
- ⁴⁵ M. Ivanovich, P. G. Young and G. G. Ohlsen, *Nucl. Phys.* **A110**, 441 (1968).
- ⁴⁶ G. Presser, R. Bass, and K. Kruger, *Nucl. Phys.* **A131**, 679 (1969).
- ⁴⁷ F. C. Barker, *Aust. J. Phys.* **25**, 341 (1972).
- ⁴⁸ D. E. Alburger et. al. *Phys. Rev.* **143**, 692 (1966).
- ⁴⁹ G. Dearnaley, D. S. Gemmell and S. S. Hanna, *Nucl. Phys.* **36**, 71 (1962).
- ⁵⁰ P. D. Forsyth et. al. *Nucl. Phys.* **82**, 33(1966).
- ⁵¹ W. Auwartet et. al. *Nucl. Phys.* **A242**, 129 (1975).
- ⁵² Tsan Mo. and W. F. Hornyak, *Phys. Rev.* **187**, 187 (1969).
- ⁵³ W. Oelert, A. Djalois, C. Mayer-Boricke, and P. Turek, *Phys. Rev. C* **19**, 1747 (1979).
- ⁵⁴ A. Kiss et. al. *Nucl. Phys.* **A282**, 44 (1977).
- ⁵⁵ G. Hardie, B. W. Filippone, A. J. Elwyn, M. Wiescher, and R. E. Segel, *Phys. Rev. C* **29**, 1199 (1984).
- ⁵⁶ M. Wiescher, R. N. Boyd, S. L. Blatt, L. J. Rybarcyk, J. A. Spizuoco, R. E. Azuma, E. T. H. Clifford, J. D. King, J. Gorres, C. Rolfs and A. Vlioks, *Phys. Rev. C* **28**, 1431 (1983).
- ⁵⁷ M. Gai, R. Keddy, D. A. Bromley, J. W. Olness and E. K. Warburton, *Phys. Rev. C* **36**, 1256 (1987).

- ⁵⁸ J. A. Becker, L. F. Chase, Jr., D. Kohler, and R. E. McDonald, *Phys. Rev. C* **8**, 2007 (1973).
- ⁵⁹ J. Gomez Del Campo, J. L. Charvet, A. D'Onofrio, R. L. Auble, J. R. Beene, M. L. Halbert, and H. J. Kim, *Phys. Rev. Lett.*, **61**, 290 (1988).
- ⁶⁰ L. G. Sobotka, D. G. Sarantites, H. Puchta, F. A. Dilmanian, M. Jaaskelainen, M. L. Halbert, J. H. Barker, J. R. Beene, R. L. Ferguson, D. C. Hensley, and G. R. Young, *Phys. Rev. C* **34**, 917 (1986).
- ⁶¹ D. Hahn and H. Stocker, *Phys. Rev. C* **35**, 1311 (1987).
- ⁶² D. J. Fields, C. K. Gelbke, W. G. Lynch, and J. Pochodzalla, *Phys. Lett.* **187B**, 257 (1987).
- ⁶³ Z. Chen, C. K. Gelbke, *Phys. Rev. C* **38**, 2630 (1988).
- ⁶⁴ B. A. Brown, Private Communication
- ⁶⁵ A. Gilbert, A. G. W. Cameron, *Canadian Journal of Physics*, **43**, 1446 (1965).
- ⁶⁶ R. G. Stokstad, Proceedings of the Topical Conference on Heavy-Ion Collisions, held at Fall Creek Falls State Park, Tennessee, June 13-17, 1977, p. 22.
- ⁶⁷ P. Marmier and E. Sheldon, *Physics of Nuclei and particles*, Vol. 1, *Academics* **38** (1969).
- ⁶⁸ A. H. Wapstra and G. Audi, *Nucl. Phys.* **A432**, 1 (1985).
- ⁶⁹ W. Hauser and H. Feshbach, *Phys. Rev.* **87**, 366 (1952).
- ⁷⁰ R. P. Schmitt, *Phys. Rev. Lett.* **65**, 2080 (1990).

- ⁷¹ T. K. Nayak and W. G. Lynch, Phys. Rev. Lett. **65**, 2081 (1990).
- ⁷² C. C. Lu, L. C. Vaz, and J. R. Huizenga, Nucl. Phys. **A229**, 229 (1972).
- ⁷³ T. Ericson, Adv. Phys. **3**, 425 (1960).
- ⁷⁴ L. D. Landau and E. M. Lifshitz, "Course of Theoretical Physics : Statistical Mechanics", Pergamon, New York (1980) Vol. 5, Pt. 1, page 236.
- ⁷⁵ K. Huang, Statistical Mechanics (Wiley, New York, 1963), p. 310.
- ⁷⁶ A. M. Lane and R. G. Thomas, Rev. of Mod. Phys. **30**, 257 (1958).

Figure Captions

Fig. 1 : Front view of the hodoscope showing all the nine light particle(LP) and four heavy fragment (HF) telescopes. The actual dimensions of heavy fragment detectors are displayed. Since they are closer to the target, however, they cover larger solid angles than suggested by this projection.

Fig. 2 : Two dimensional position spectrum of the calibration mask for one of the heavy fragment detectors. The missing points were used to identify and establish the orientation of the different detectors.

Fig. 3 : Inclusive differential cross sections for H and He isotopes as shown for laboratory angles listed in the figure. The solid lines represent "moving source fits".

Fig. 4 : Inclusive differential cross section for selected isotopes of Lithium, Beryllium, Boron, Carbon, Nitrogen and Oxygen are shown for laboratory angles listed in the figure. The solid lines represent "moving source fits".

Fig. 5 : Inclusive differential cross section for ^{10}B fragments. The solid curves describe the full "three moving source" fits and the dashed curves show the emission from a slow moving "target like" source.

Fig. 6 : Correlation function as a function of relative energy for α -p. The relative energy of α -p, and the excitation energy of ^5Li are indicated in the lower and upper scale respectively. The solid curve is the fit to the data assuming the background designated by the dashed line. The dotted line shows an alternate background.

Fig. 7 : Correlation function as a function of relative energy for $^3\text{He-d}$. The relative energy of $^3\text{He-d}$ is shown in the lower scale and the upper scale gives the excitation energy

of ${}^5\text{Li}$. The solid curve is the fit to the data assuming the background designated by the dashed line. The dotted line shows an alternate background.

Fig. 8 : The d- α correlation as a function of the relative energy. The fits to the resonances is shown by solid lines assuming the background shown by dashed line. The dotted curve shows as an alternative form of the background.

Fig. 9 : t- α correlation function as a function of relative energy. The location and spins of particle-unstable states in ${}^7\text{Li}$ are indicated. The insert gives an expanded view showing the second maximum. The solid curves are the fits to the data assuming the background designated by the dashed line. The dotted line shows an alternate background.

Fig. 10 : p- ${}^6\text{He}$ correlation function as a function of relative energy. The excitation energy in ${}^7\text{Li}$ is indicated on the top. The location and spin of a particle-unstable state in ${}^7\text{Li}$ is shown.

Fig. 11 : Correlation function as a function of relative energy for ${}^3\text{He}$ - α . The location and spins of particle-unstable states in ${}^7\text{Li}$ are indicated. The insert gives an expanded view showing the second maximum in the correlation function. The solid curves give a fit to the data with the background shown by the dashed lines. The dotted line shows an alternate background.

Fig. 12 : p- ${}^6\text{Li}$ correlation function as a function of relative energy. The location and spin of a particle-unstable state in ${}^7\text{Be}$ is indicated. The solid curve shows a fit to the data with the background designated by the dashed line. The dotted line shows an alternate background.

Fig. 13 : ${}^8\text{B} \rightarrow {}^7\text{Be} + \text{p}$ correlation function. The excitation energy in ${}^8\text{B}$ is indicated

on the top. The solid curve shows a fit to the data assuming the background depicted by the dashed line. The dotted line shows an alternate background.

Fig. 14 : ${}^6\text{Li}+\alpha$ (upper part) and ${}^9\text{Be}+p$ (lower part) excitation energy spectra. The location and spins of particle-unstable states in ${}^{10}\text{B}$ are indicated. The solid curves show the fits to the data assuming the background depicted by the dashed line. The dotted lines indicate an alternate choice for the background.

Fig. 15 : Excitation energy spectrum of ${}^{11}\text{C}$ obtained from the coincidence cross section of ${}^7\text{Be}+\alpha$. The relative energy of ${}^7\text{Be}$ and α , and the excitation energy of ${}^{11}\text{C}$ are indicated in the lower and upper parts, respectively. The solid line is a fit to the data assuming the background depicted by the the dashed line. The dotted line shows an alternate background.

Fig. 16 : Excitation energy spectrum of ${}^{13}\text{N}$ obtained from the coincidence cross section of ${}^{12}\text{C}-p$. The lower scale gives the relative energy of ${}^{12}\text{C}$ and proton, and the upper scale gives the excitation energy of ${}^{13}\text{N}$ assuming proton decay which leaves ${}^{12}\text{C}$ in its ground state. The locations of states which decay to ${}^{12}\text{C}$ in its ground and excited states are indicated by the solid and dotted marks, respectively. The solid line is a fit to the data assuming the background depicted by the dashed line. The dotted curve shows an alternate background.

Fig. 17 : Energy spectrum resulting from the decay of particle unstable ${}^{14}\text{N}$. The relative energy of ${}^{13}\text{C}$ and proton, and the excitation energy of ${}^{14}\text{N}$ are indicated in the lower and upper scales, respectively. The solid curve is a fit described in the text assuming the background shown by the dashed curve. The dotted curve shows an alternate description of the background.

Fig. 18 : Excitation energy spectrum of ${}^{16}\text{O}$ obtained from the coincidence cross section of ${}^{12}\text{C}+\alpha$. The scale in the bottom gives the relative energy of ${}^{12}\text{C}$ and α , and the top scale

gives the excitation energy for ^{16}O . The locations of states which decay to ^{12}C in its ground and excited states are indicated by the solid and dotted marks, respectively. The solid curve describes a fit obtained by assuming the dashed line as one possible background. The dotted curve shows an alternate background.

Fig. 19 : Excitation energy spectrum of ^{18}O obtained from the ^{14}C - α coincidence cross section. The lower scale indicates the relative energy of ^{14}C and α , and the upper scale shows the excitation energy of ^{18}O . The solid curve describes a fit obtained by assuming the dashed curve as one possible background.

Fig. 20 : Elemental yields at $\theta = 38^\circ$ summed over measured energies. The dashed and solid histograms show the primary and final yields of particle stable fragments produced by the feeding calculations. Results for $T_{\text{em}}=2, 3, 4, 5, 6,$ and 8 MeV with the corresponding parameters f are given in the figure.

Fig. 21 : Comparisons of measured and calculated isotopic yields at $\theta = 38^\circ$. The solid histograms show final fragment distributions for feeding calculations at $T_{\text{em}}=2, 3,$ and 4 MeV.

Fig. 22 : Comparisons of measured and calculated isotopic yields at $\theta = 38^\circ$. The solid histograms show final fragment distributions for feeding calculations at $T_{\text{em}}=5, 6,$ and 8 MeV.

Fig. 23 : Results of the least-squares analysis for four groups of fragments. The solid lines depict χ^2_{ν} calculated for a combination of population probabilities and the ratios of population probabilities. The dot-dashed lines show χ^2_{ν} when just the ratios of population probabilities are included.

Fig. 24 : Results of least-squares analysis for a combination of all fragments. The dashed, dash-dotted and solid lines depict χ^2_ν calculated for the population probabilities, the ratios of populations probabilities, and the summation of the population probabilities and ratios of population probabilities respectively. The dotted line depicts χ^2_ν calculated from the decays of ^5Li .

Fig. 25 : Experimental values for β_{app} and T_{app} are shown as the solid points for excited states of Li and Be isotopes. The histograms represent the results of sequential feeding calculation with an initial temperature $T_{\text{em}} = 4$ MeV. The shaded region between the histograms represent the range of values predicted by the sequential feeding calculations for an initial temperature of $T_{\text{em}} = 4$ MeV.

Fig. 26 : Experimental values for β_{app} and T_{app} are shown as the solid points for the groups of excited states of B and C isotopes described in table 3.3. The histograms represent the results of sequential feeding calculation with an initial temperature $T_{\text{em}} = 4$ MeV. The shaded region between the histograms represent the range of values predicted by the sequential feeding calculations for an initial temperature of $T_{\text{em}} = 4$ MeV.

Fig. 27 : Experimental values for β_{app} and T_{app} are shown as the solid points for the groups of excited states of ^{13}N and ^{14}N described in table 3.4. The histograms represent the results of sequential feeding calculation with an initial temperature $T_{\text{em}} = 4$ MeV. The shaded region between the histograms represent the range of values predicted by the sequential feeding calculations for an initial temperature of $T_{\text{em}} = 4$ MeV.

Fig. 28 : Experimental values for β_{app} and T_{app} are shown as the solid points for the groups of excited states of ^{16}O and ^{18}O described in table 3.5. The histograms represent the results of sequential feeding calculation with an initial temperature $T_{\text{em}} = 4$ MeV. The shaded

region between the histograms represent the range of values predicted by the sequential feeding calculations for an initial temperature of $T_{em} = 4$ MeV.

Fig. 29 : Relative populations, n_i , of different groups of particle-unstable states in ^{10}B are plotted as a function of excitation energy. The vertical scale is normalized so that $\sum_k (2J_k + 1)n_k = 1$, where the summation is restricted to the particle-stable states of ^{10}B .

Fig. 30 : Calculations for n_i from the sequential feeding calculation $T_{em} = 4$ MeV, $\bar{m}_{12C} = 6$ and $(\sigma_m)_{12C} = 2.5$ are shown as the solid line in the figure. Experimental values for n_i are depicted by the large solid points.

Fig. 31 : Calculations for n_i in the limit of full spin coupling are shown as dotted, dashed, dot-dashed and solid lines for parent nuclear spins $I_p = 25, 50, 75$ and 100 respectively.

Fig. 32 : Coordinate system used to describe the α -decay of particle unstable excited states of ^{10}B . θ_d and ϕ_d are the decay angles as defined in the text.

Fig. 33 : Relative energy spectra for the decay $^{10}\text{B} \rightarrow \alpha + ^6\text{Li}$ at different values of the decay angle, θ_d .

Fig. 34 : The θ_d dependence of the decay angular distributions are shown for various excited states of ^{10}B . The vertical scale is normalized to the average value of the distributions for each case. The dashed line shows the prediction from an isotropic decay.

Fig. 35 : The ϕ_d dependence of the decay angular distributions are shown for various excited states of ^{10}B . The vertical scale is normalized to the average value of the distributions for each case. The dashed line shows the prediction from an isotropic decay.

Fig. 36 : The θ_d dependence of the decay angular distributions is shown for the first

excited state of ^{10}B . The vertical scale is normalized to the average value. The predictions from statistical calculations with $I_p = 25, 50, 75, 100$ are shown by dotted, dashed, dot-dashed and solid lines respectively.

Table 1: Source parameters of three moving-source fits. The Coulomb repulsion energies U_c and the temperature parameters T_i are given in units of MeV, and the normalization constants N_i are given in units of $\mu\text{b}/(\text{sr MeV}^{3/2})$.

	U_c	T_1	v_1/c	N_1	T_2	v_2/c	N_2	T_3	v_3/c	N_3
p	6.23	3.46	0.036	33490	9.27	0.168	618	3.98	0.27	4159
d	8.56	4.04	0.03	4372	12.07	0.12	164	7.30	0.223	1862
t	8.33	5.49	0.035	1421	12.24	0.14	892.7	6.11	0.242	804.5
^3He	13.08	5.35	0.04	530.5	12.80	0.158	411.1	4.96	0.26	1601
α	12.82	5.38	0.045	11060	12.91	0.138	2101	6.43	0.232	4289
^6He	15.54	6.14	0.043	96.32	14.49	0.116	28.82	9.56	0.193	32.16
^6Li	16.00	9.17	0.064	74.54	16.73	0.114	50.96	11.22	0.207	106.2
^7Li	15.81	19.57	0.023	79.10	4.64	0.089	121.2	12.17	0.139	83.81
^7Be	20.66	8.97	0.06	14.98	18.77	0.107	14.87	11.08	0.198	57.83
^9Be	20.24	10.24	0.055	32.98	17.97	0.114	12.53	10.89	0.200	41.32
^8B	30.41	9.09	0.053	0.63	18.90	0.113	0.40	11.33	0.207	2.54
^{10}B	29.86	9.09	0.053	24.62	18.90	0.113	9.33	11.33	0.207	55.98
^{11}C	40.97	7.72	0.054	7.12	16.82	0.105	2.46	12.02	0.193	13.62
^{12}C	40.67	7.38	0.053	33.17	16.28	0.091	7.15	13.75	0.176	12.57
^{14}C	40.15	9.53	0.051	7.31	14.97	0.101	1.25	16.11	0.155	0.84
^{13}N	46.15	10.43	0.061	0.57	16.69	0.118	0.13	9.88	0.194	2.06
^{14}N	45.87	10.43	0.061	6.21	16.69	0.118	1.41	9.88	0.194	11.93
^{16}O	50.74	12.22	0.057	4.25	3.42	0.091	31.08	12.34	0.114	1.24
^{18}O	50.25	12.22	0.057	1.43	3.42	0.091	19.36	12.34	0.114	0.06

Table 2: Spectroscopic information for Lithium and Beryllium isotopes. Branching ratios Γ_c/Γ are given in percentage. Unless otherwise noted the decays are to the ground states of the daughter fragments. Except for ${}^5\text{Li}$, population probabilities n_λ are defined relative to the particle stable yields for the same nucleus. The group structure is explained in the text.

	Group	$E^*(\text{MeV})$	J^π	$\Gamma_{\text{cm}}(\text{MeV})$	Decay Products	Γ_c/Γ	Population Probability, n_λ
${}^5\text{Li}$	1	g.s.	$\frac{3}{2}^-$	1.5	α -p	100	^{a)} 0.347 ± 0.03
	2	16.66^b	$\frac{3}{2}^+$	0.20	${}^3\text{He}$ -d	86^b	^{a)} $5.3 \times 10^{-3} \pm 1.4 \times 10^{-3}$
${}^6\text{Li}$	1	2.186	3^+	0.024	α -d	100	0.15 ± 0.01
	2	4.31	2^+	1.7	α -d	97	0.059 ± 0.02
		5.65	1^+	1.5	α -d	74	
${}^7\text{Li}$	1	4.63^b	$\frac{7}{2}^-$	0.093^b	α -t	100^b	$0.047 \pm 2.5 \times 10^{-3}$
	2	6.68^b	$\frac{5}{2}^-$	0.875^b	α -t	100^b	$0.03 \pm 7 \times 10^{-3}$
		7.46^b	$\frac{5}{2}^-$	0.089^b	α -t	18^b	
	3	11.24	$\frac{3}{2}^-$	0.272	${}^6\text{He}$ -p	59	$4.8 \times 10^{-3} \pm 1 \times 10^{-3}$
${}^7\text{Be}$	1	4.57^b	$\frac{7}{2}^-$	0.175^b	α - ${}^3\text{He}$	100	$0.052 \pm 5 \times 10^{-3}$
	2	6.73^b	$\frac{5}{2}^-$	1.2^b	α - ${}^3\text{He}$	100^b	0.031 ± 0.01
		7.21^b	$\frac{5}{2}^-$	0.5^b	α - ${}^3\text{He}$	3^b	
	3	7.21	$\frac{5}{2}^-$	0.5	${}^6\text{Li}$ -p	97	$0.021 \pm 3.5 \times 10^{-3}$

^{a)} Values of n_λ for ${}^5\text{Li}$ are defined relative to the the particle stable yields of ${}^6\text{Li}$.

^{b)} Analysis performed using R -matrix parameters given in the text.

Table 3: Spectroscopic information for ^8B , ^{10}B , and ^{11}C isotopes. Unless otherwise noted the decays are to the ground states of the daughter fragments. The branching ratios are given in percent, and n_λ are defined relative to the particle stable yields for the same nucleus. The group structure is explained in the text.

	Group	$E^*(\text{MeV})$	J^π	$\Gamma_{\text{cm}}(\text{keV})$	Decay Products	Γ_c/Γ	Population Probability n_λ	
^8B	1	0.774	1	37	$^7\text{Be-p}$	100	0.152 ± 0.016	
	2	2.32	3^+	310	$^7\text{Be-p}$	100	0.212 ± 0.085	
^{10}B	1	4.774	3^+	8.4×10^{-3}	$^6\text{Li-}\alpha$	100	$0.016^{+2.6 \times 10^{-3}}_{-1.7 \times 10^{-3}}$	
		2	5.1103	2^-	0.98	$^6\text{Li-}\alpha$		100
			5.1639	2^+	1.76×10^{-3}	$^6\text{Li-}\alpha$		13
		5.180	1^+	110	$^6\text{Li-}\alpha$	100	$0.01^{+3.6 \times 10^{-3}}_{-1.6 \times 10^{-3}}$	
	3	5.9195	2^+	6	$^6\text{Li-}\alpha$	100		
		6.0250	4^+	0.05	$^6\text{Li-}\alpha$	100		
		6.1272	3^-	2.36	$^6\text{Li-}\alpha$	97		
	4	6.56	4^-	25.1	$^6\text{Li-}\alpha$	100	$0.01^{+1.2 \times 10^{-3}}_{-1.1 \times 10^{-3}}$	
	5	7.430	2^-	100	$^9\text{Be-p}$	70	$0.0045^{+9.5 \times 10^{-4}}_{-1.6 \times 10^{-4}}$	
		7.467	1^+	65	$^9\text{Be-p}$	100		
		7.478	2^+	74	$^9\text{Be-p}$	65		
		7.5599	0^+	2.65	$^9\text{Be-p}$	100		
	6	7.67	1^+	250	$^9\text{Be-p}$	30	$0.0055^{+4.1 \times 10^{-3}}_{-7.4 \times 10^{-4}}$	
		7.819	1^-	260	$^9\text{Be-p}$	90		
8.07		2^+	800	$^9\text{Be-p}$	10			
7	8.889	3^-	84	$^9\text{Be-p}$	95	$0.0027^{+2.8 \times 10^{-4}}_{-3.5 \times 10^{-4}}$		
	8.895	2^+	40	$^9\text{Be-p}$	19			
^{11}C	1	8.1045	$\frac{3}{2}^-$	0.011	$^7\text{Be-}\alpha$	92	$5.80 \times 10^{-3} \pm 4.3 \times 10^{-4}$	
	2	8.420	$\frac{5}{2}^-$	0.015	$^7\text{Be-}\alpha$	80	$5.67 \times 10^{-3} \pm 4.3 \times 10^{-4}$	
	3	8.655	$\frac{7}{2}^+$	5	$^7\text{Be-}\alpha$	94	$5.93 \times 10^{-3} \pm 3.4 \times 10^{-4}$	
8.701		$\frac{5}{2}^+$	15	$^7\text{Be-}\alpha$	100			

Table 4: Spectroscopic information for ^{13}N and ^{14}N isotopes. Branching ratios Γ_c/Γ are given in percent, and n_λ are defined relative to the particle stable yields for the same nucleus. Unless otherwise noted the decays are to the ground states of the daughter fragments. The group structure is explained in the text.

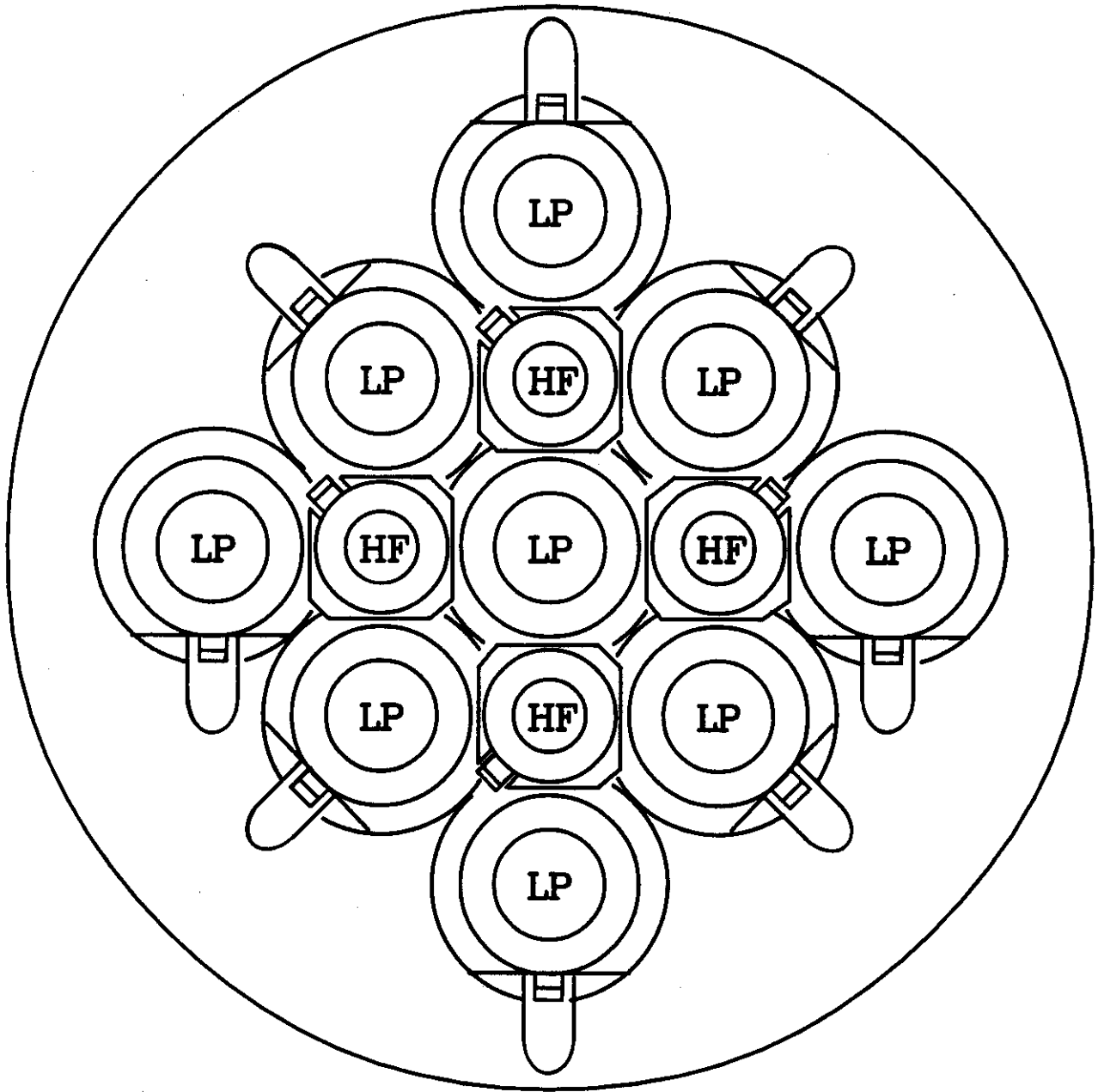
	Group	$E^*(\text{MeV})$	J^π	$\Gamma_{\text{cm}}(\text{keV})$	Decay Products	Γ_c/Γ	Population Probability n_λ
^{13}N	1	3.511	$\frac{3}{2}^-$	62	$^{12}\text{C-p}$	100	0.110±0.02
		3.547	$\frac{5}{2}^+$	47	$^{12}\text{C-p}$	100	
	2	7.155	$\frac{7}{2}^+$	9	$^{12}\text{C-p}$	^{a)} 100	0.07±0.02
^{14}N	1	7.9669	2^-	2.5×10^{-3}	$^{13}\text{C-p}$	99	$7.3 \times 10^{-3} \pm 1.4 \times 10^{-3}$
	2	8.062	1^-	30	$^{13}\text{C-p}$	100	$5.3 \times 10^{-3} \pm 1.7 \times 10^{-3}$
	3	8.4899	4^-	3.46×10^{-5}	$^{13}\text{C-p}$	79	$9.8 \times 10^{-3} \pm 1.1 \times 10^{-3}$
		8.6197	0^+	3.8	$^{13}\text{C-p}$	100	
		8.776	0^-	410	$^{13}\text{C-p}$	100	
	4	8.9118	3^-	16	$^{13}\text{C-p}$	100	$6.32 \times 10^{-3} \pm 7.9 \times 10^{-4}$
		8.9638	5^+	6.25×10^{-6}	$^{13}\text{C-p}$	80	
		8.9804	2^+	8	$^{13}\text{C-p}$	100	
	5	9.1289	3^+	18.9×10^{-6}	$^{13}\text{C-p}$	81	$5.7 \times 10^{-3} \pm 1.2 \times 10^{-3}$
		9.1723	2^+	0.135	$^{13}\text{C-p}$	95	
	6	9.3893	2^-	13	$^{13}\text{C-p}$	100	$3.8 \times 10^{-3} \pm 7.1 \times 10^{-4}$
		9.509	2^-	41	$^{13}\text{C-p}$	100	
7	10.079	3^+	10	$^{13}\text{C-p}$	100	$5.4 \times 10^{-3} \pm 1.0 \times 10^{-3}$	
	10.101	2^+	12	$^{13}\text{C-p}$	100		
8	10.812	5^+	0.39×10^{-3}	$^{13}\text{C-p}$	96	$6.2 \times 10^{-3} \pm 1.5 \times 10^{-3}$	
9	11.05	3^+	1.2	$^{13}\text{C-p}$	100	$4.2 \times 10^{-3} \pm 1.3 \times 10^{-3}$	

^{a)} Branching ratio for proton decay to an excited $^{12}\text{C}^*$ nucleus ($E^* = 4.44 \text{ MeV}$) and proton.

Table 5: Spectroscopic information for ^{16}O and ^{18}O isotopes. Branching ratios Γ_c/Γ are given in percent, and n_λ are defined relative to the particle stable yields for the same nucleus. Unless otherwise noted the decays are to the ground states of the daughter fragments. The group structure is explained in the text.

	Group	$E^*(\text{MeV})$	J^π	$\Gamma_{\text{cm}}(\text{keV})$	Decay Products	Γ_c/Γ	Population Probability, n_λ
^{16}O	1	12.530	2^-	0.097	$^{12}\text{C}-\alpha$	^{a)} 74	$1.89 \times 10^{-3} \pm 7.2 \times 10^{-4}$
	2	9.845	2^+	0.625	$^{12}\text{C}-\alpha$	100	$7.4 \times 10^{-3} \pm 5.2 \times 10^{-3}$
		14.1	3^-	750	$^{12}\text{C}-\alpha$	^{a)} 80	
		14.302	4^-	32	$^{12}\text{C}-\alpha$	^{a)}	
		14.399	5^+	27	$^{12}\text{C}-\alpha$	^{a)}	
	3	10.356	4^+	25	$^{12}\text{C}-\alpha$	100	$4.5 \times 10^{-3} \pm 1.1 \times 10^{-3}$
		14.62	4^+	490	$^{12}\text{C}-\alpha$	^{a)} 20	
		14.66	5^-	670	$^{12}\text{C}-\alpha$	^{a)} 6	
		14.815	6^+	70	$^{12}\text{C}-\alpha$	^{a)} 65	
		14.926	2^+	54	$^{12}\text{C}-\alpha$	^{a)} 58	
4	11.097	4^+	0.28	$^{12}\text{C}-\alpha$	100	$5.3 \times 10^{-3} \pm 1.1 \times 10^{-3}$	
	15.408	3^-	132	$^{12}\text{C}-\alpha$	^{a)} 1		
^{18}O	1	7.117	4^+	2.6×10^{-5}	$^{14}\text{C}-\alpha$	53	$4.1 \times 10^{-3} \pm 1.0 \times 10^{-3}$
	2	7.864	5^-	8	$^{14}\text{C}-\alpha$	100	$6.1 \times 10^{-3} \pm 1.5 \times 10^{-3}$
	3	8.039	1^-	2.5	$^{14}\text{C}-\alpha$	100	$2.93 \times 10^{-3} \pm 6.7 \times 10^{-4}$
		8.125	5^-	1	$^{14}\text{C}-\alpha$	100	
		8.213	2^+	1.6	$^{14}\text{C}-\alpha$	99	
8.282		3^-	8	$^{14}\text{C}-\alpha$	89		

^{a)} Branching ratio for α decay to an excited $^{12}\text{C}^*$ nucleus ($E^* = 4.44 \text{ MeV}$).



0 1 2 3 4 5
Scale in cm

Fig 1

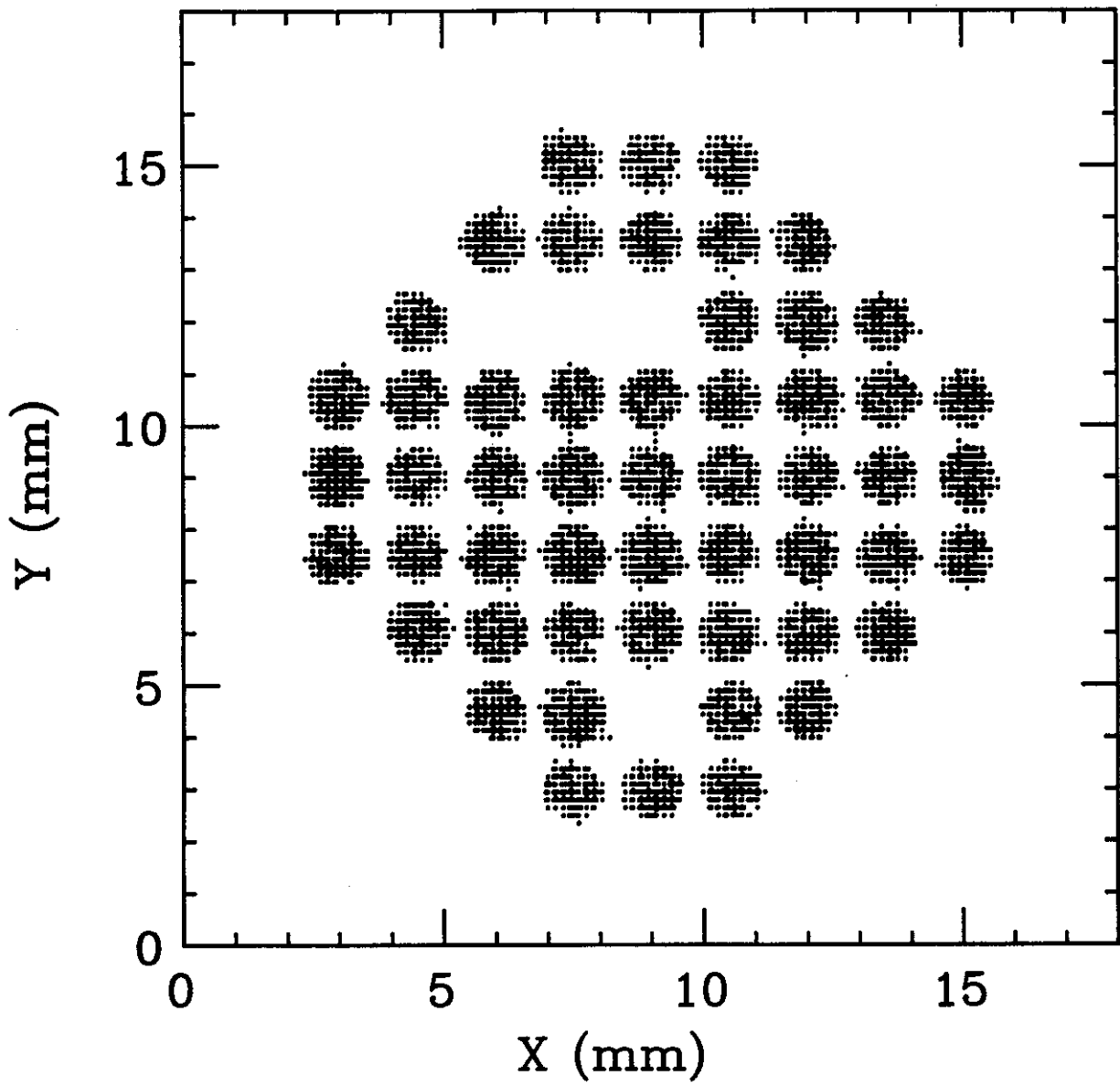


Fig 2

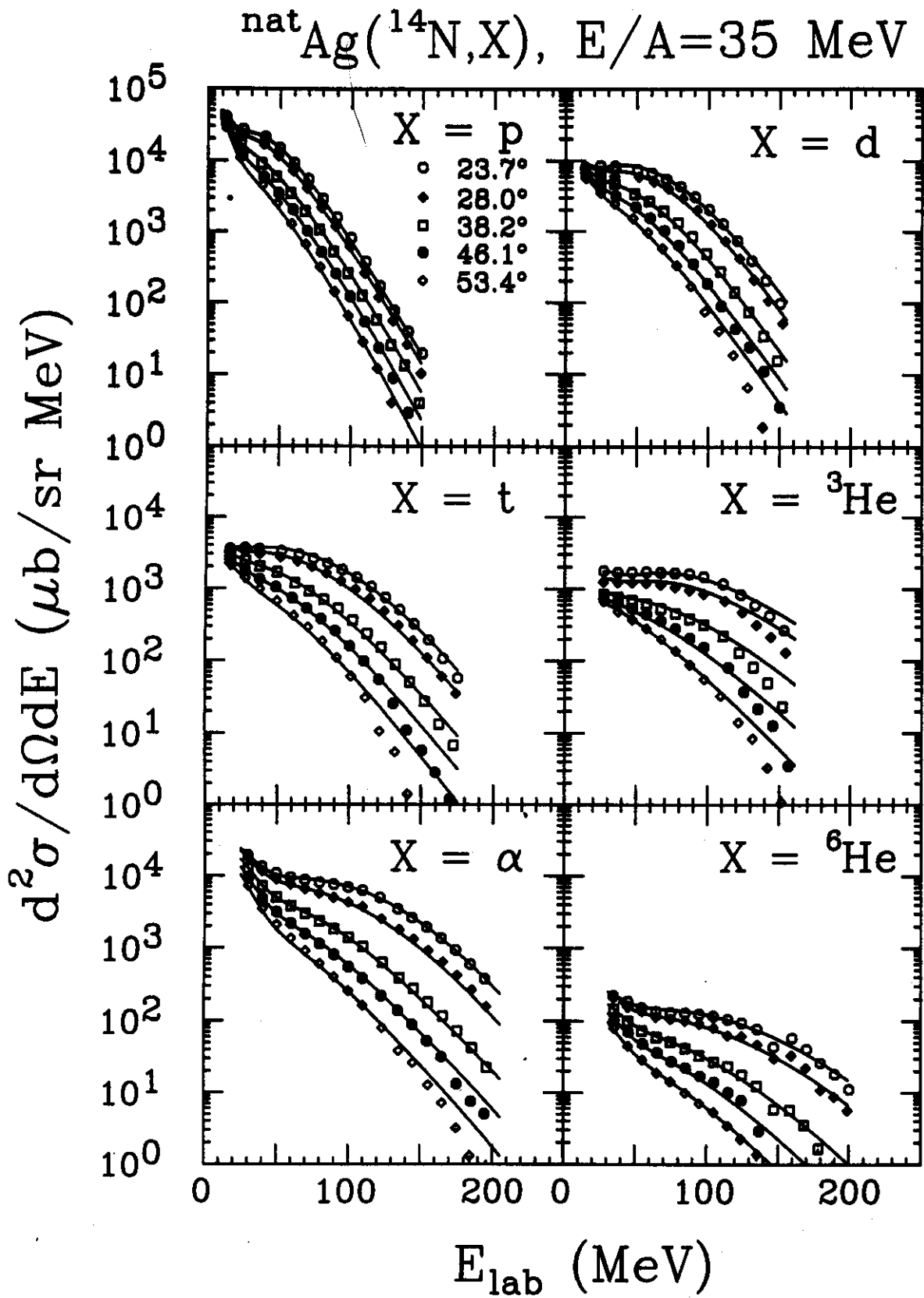


Fig 3

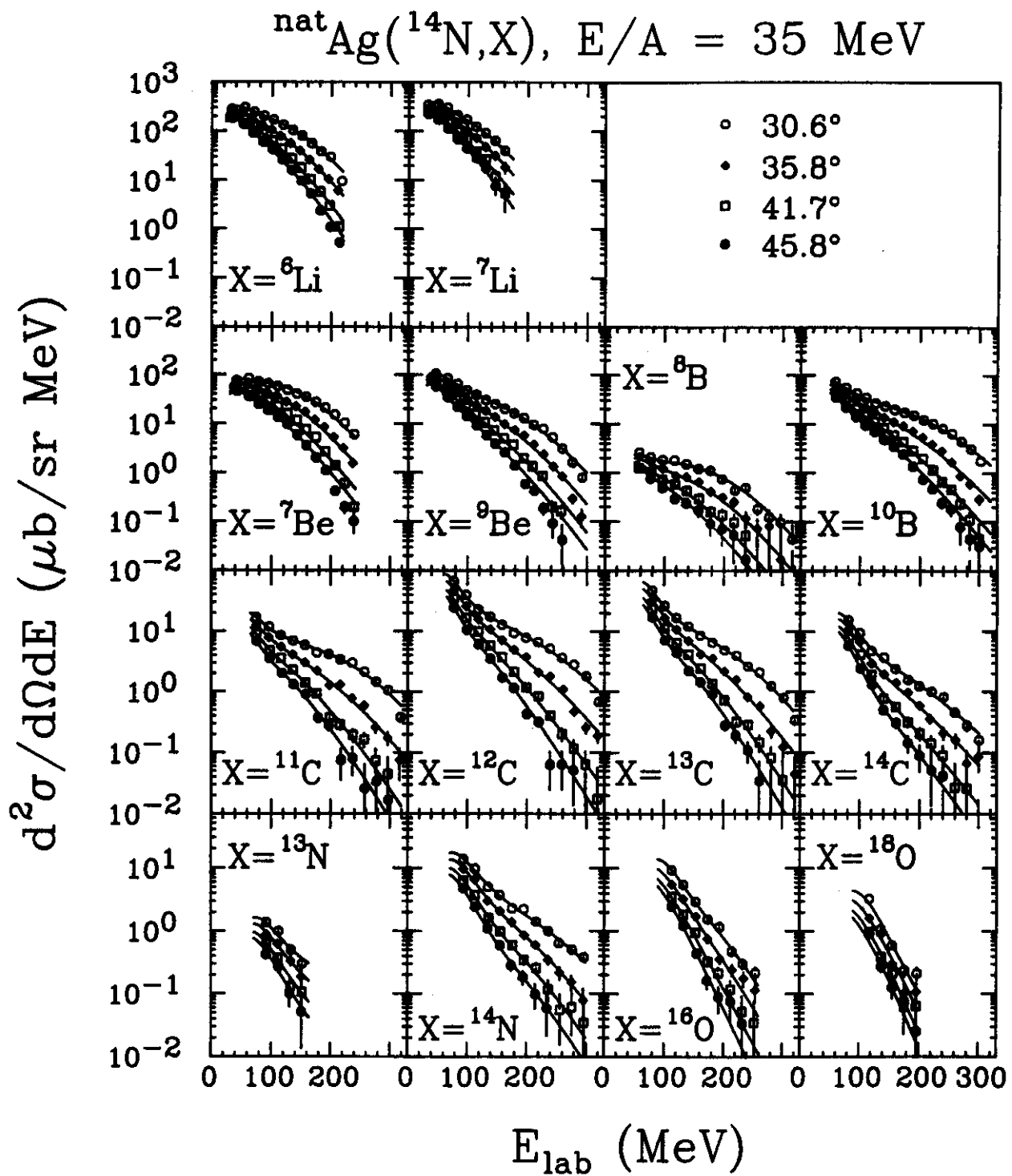


Fig 4

$^{nat}\text{Ag}(^{14}\text{N}, ^{10}\text{B})\text{X}$, $E/A=35$ MeV

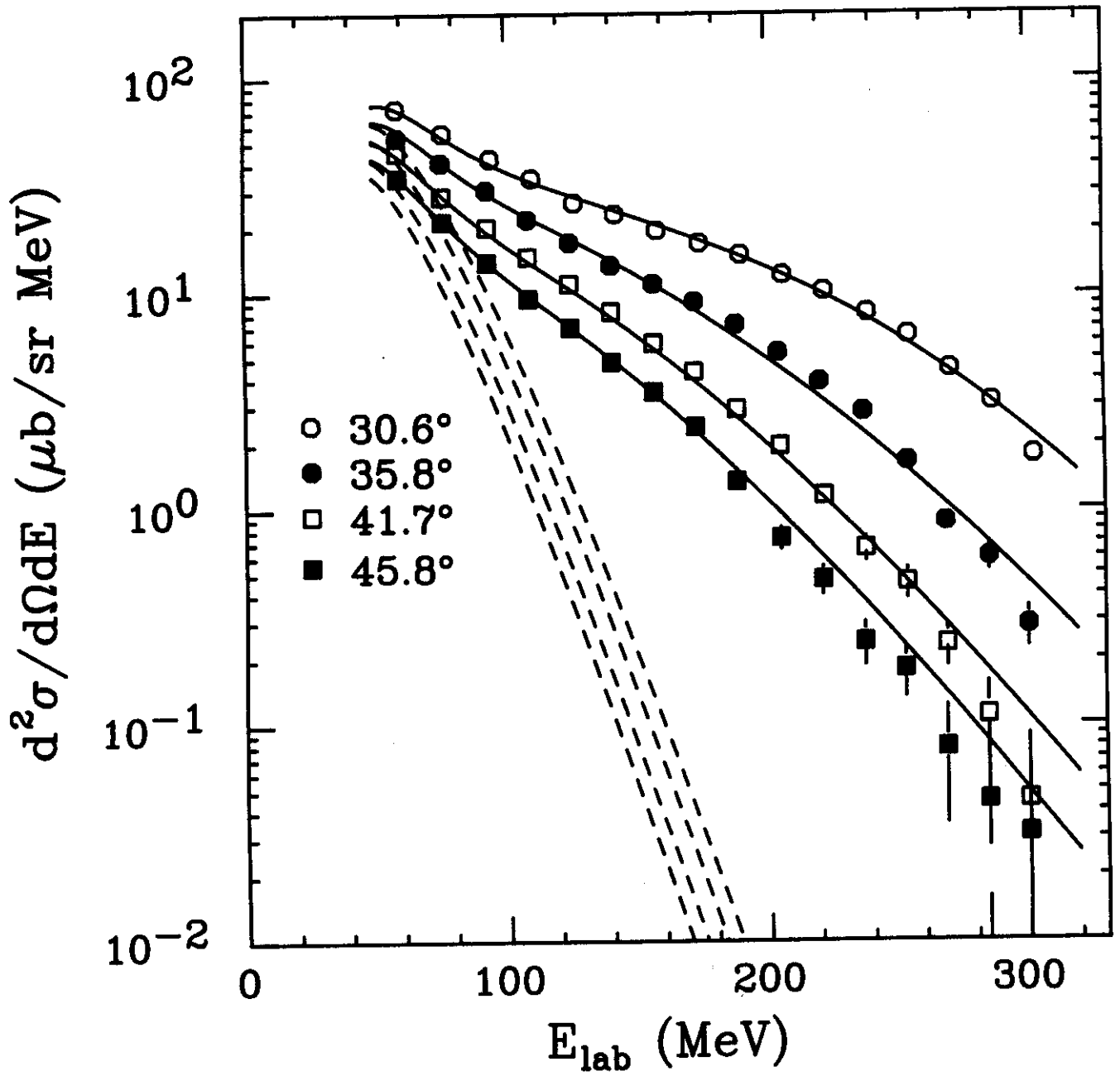


Fig 5

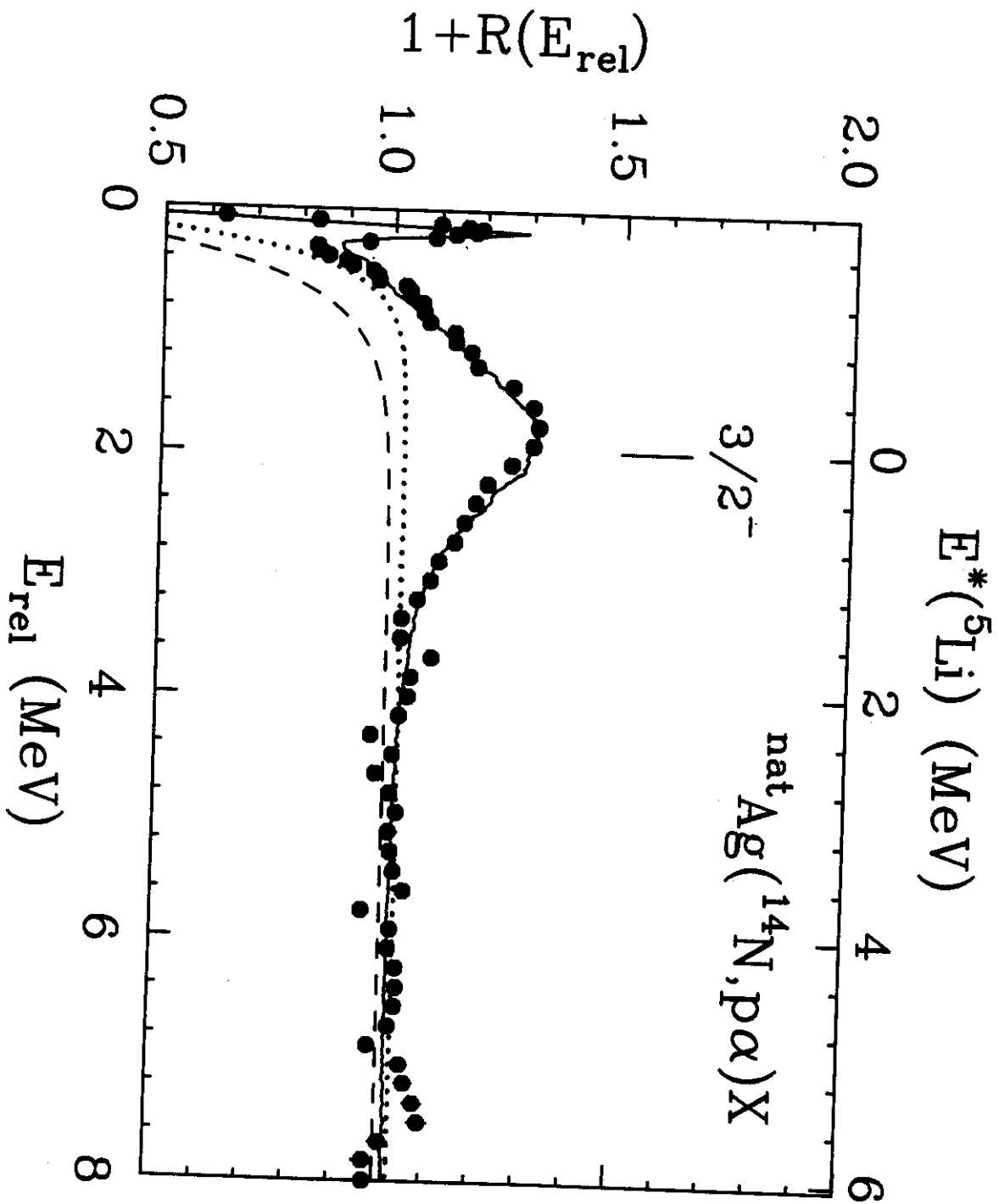


Fig 6

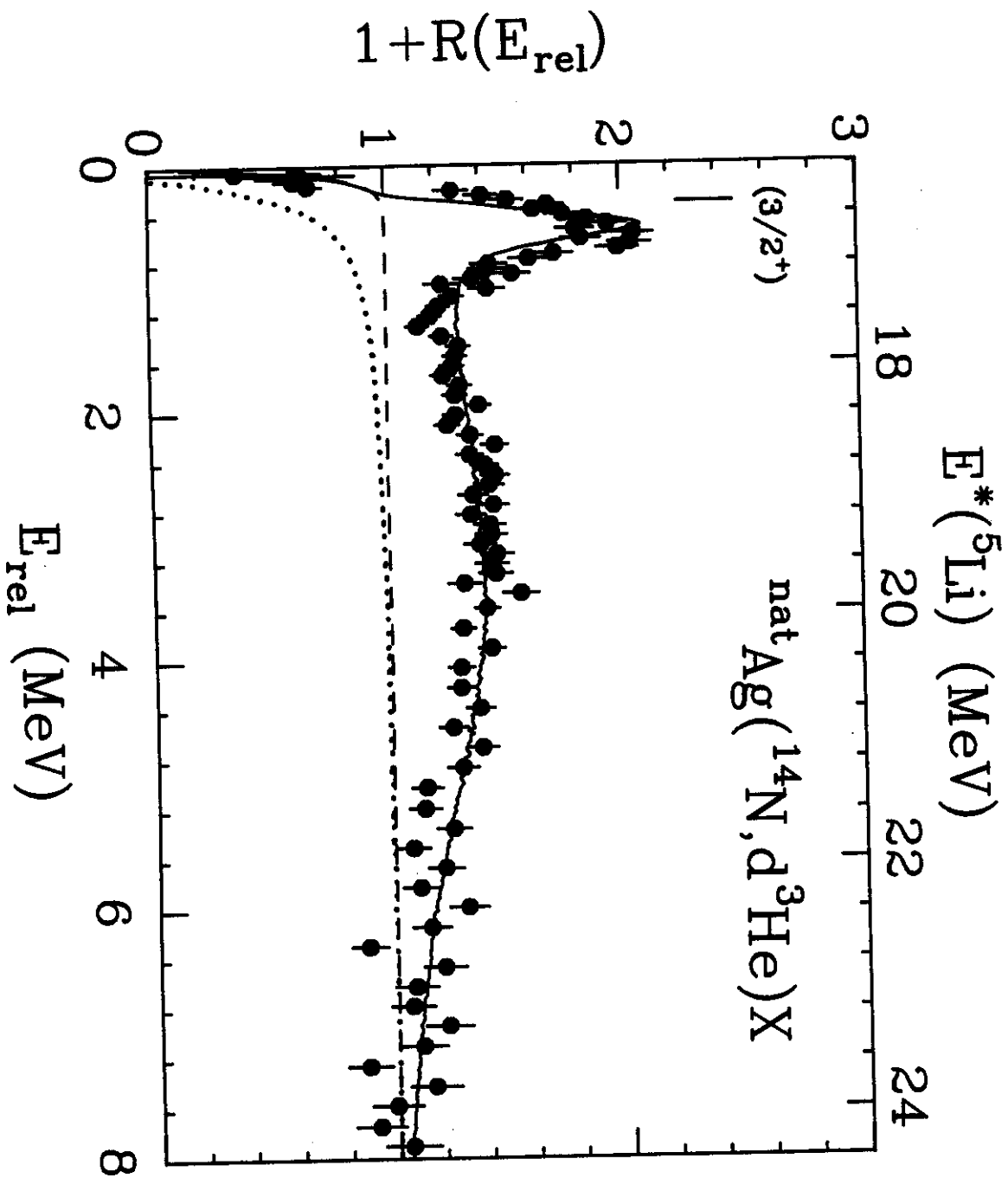


Fig 7

$^{nat}\text{Ag}(^{14}\text{N}, \alpha d)X$

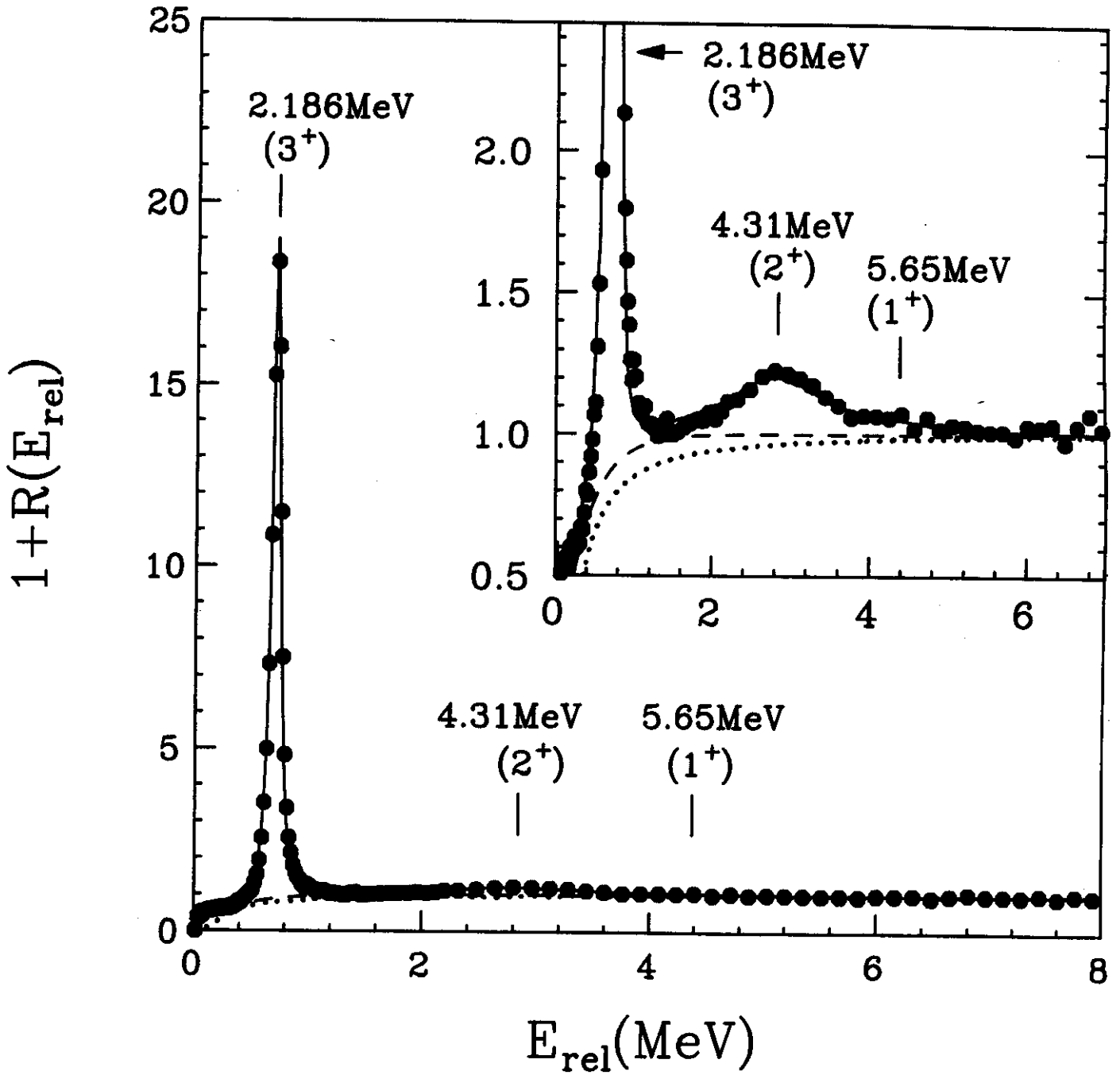


Fig 8

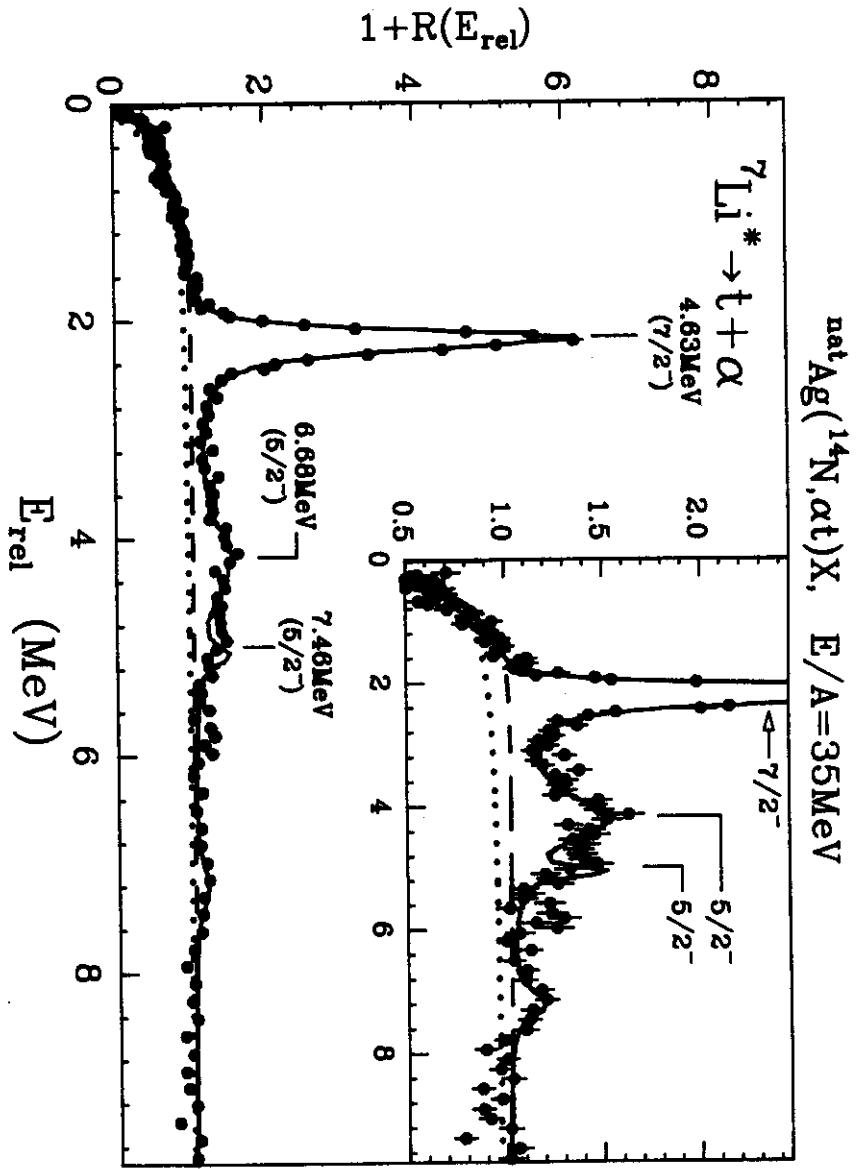


Fig 9

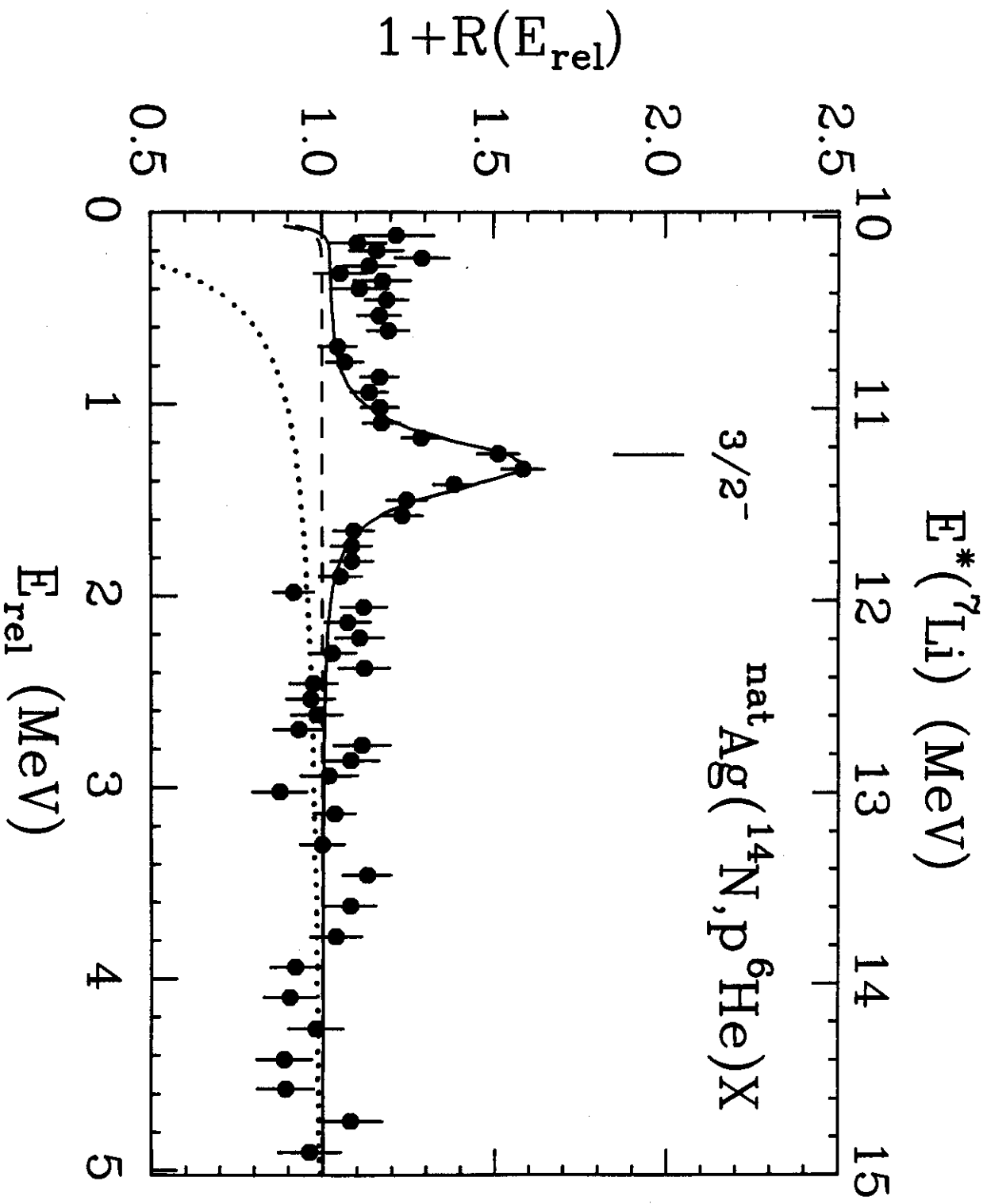


Fig. 10

$^{nat}Ag(^{14}N, \alpha^3He)X, E/A=35MeV$

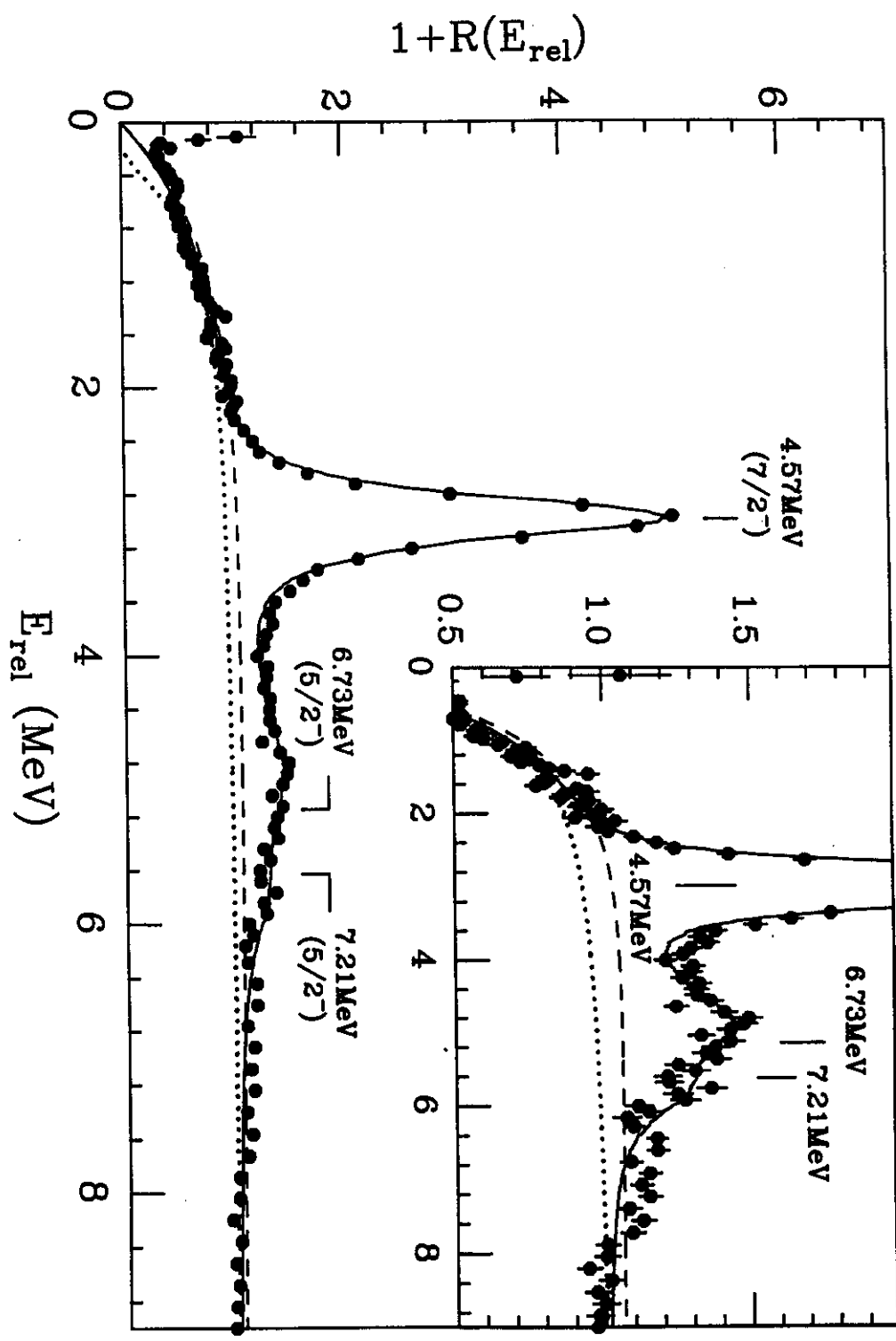


Fig 11

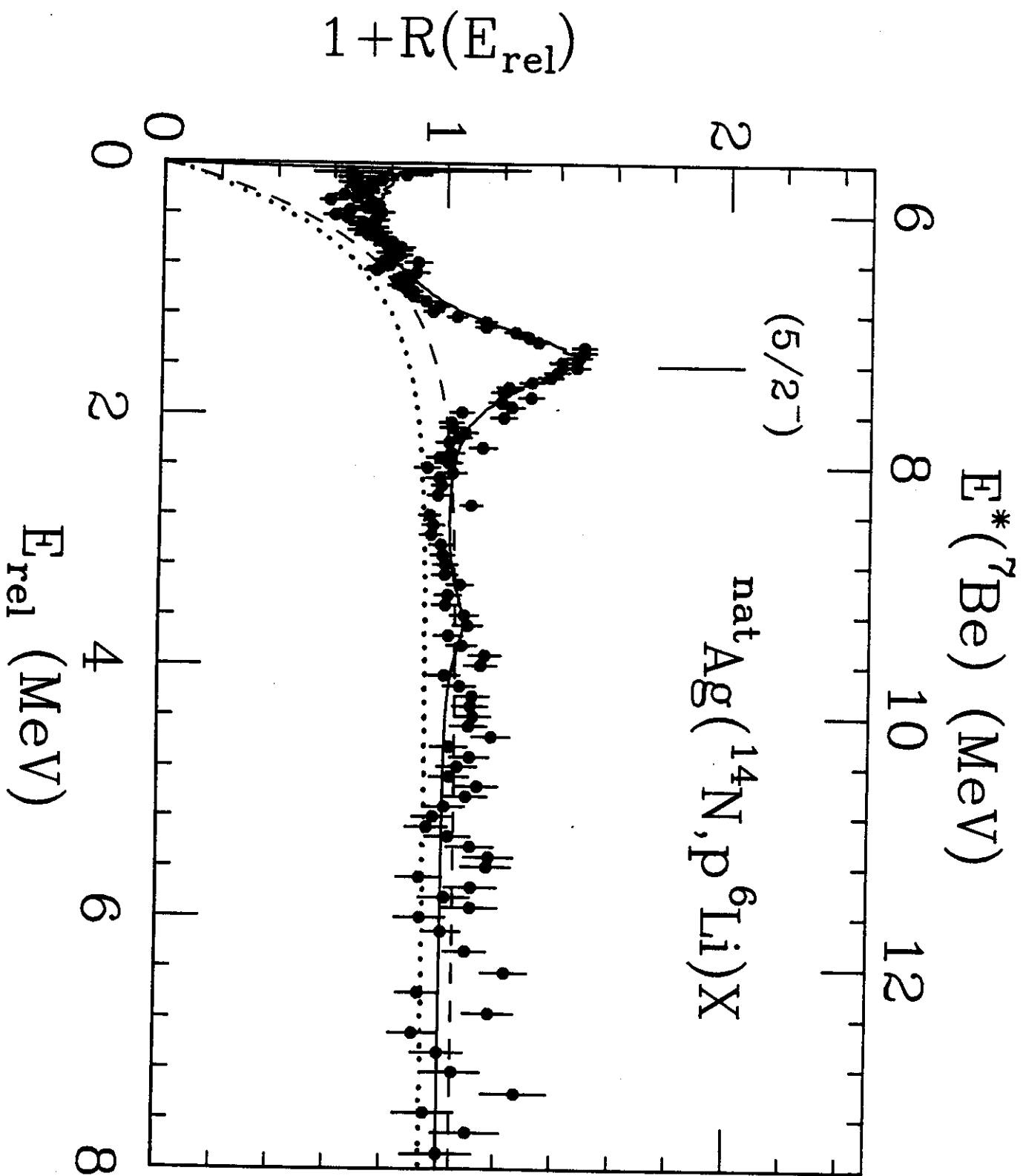


Fig 12.

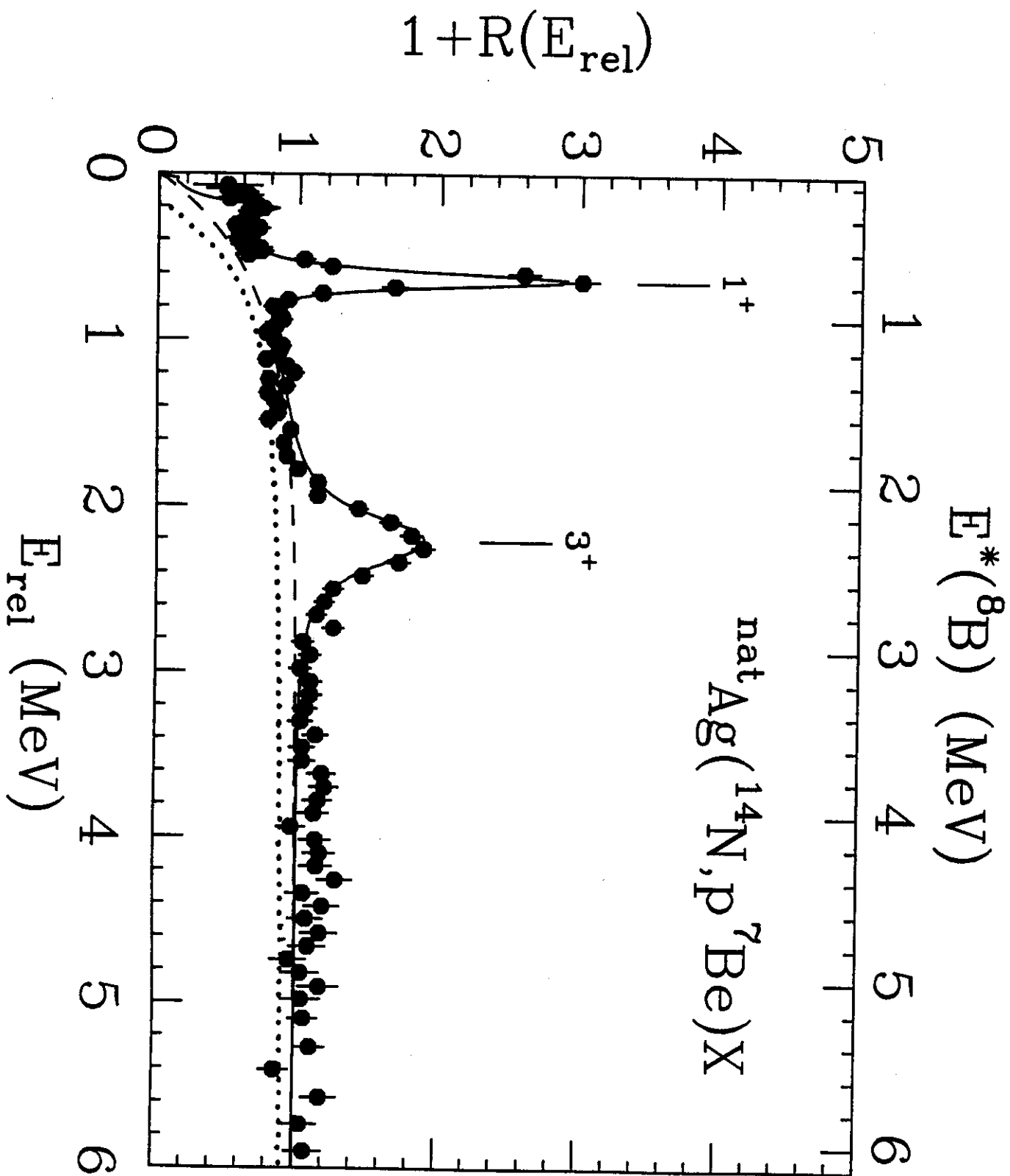


Fig 13

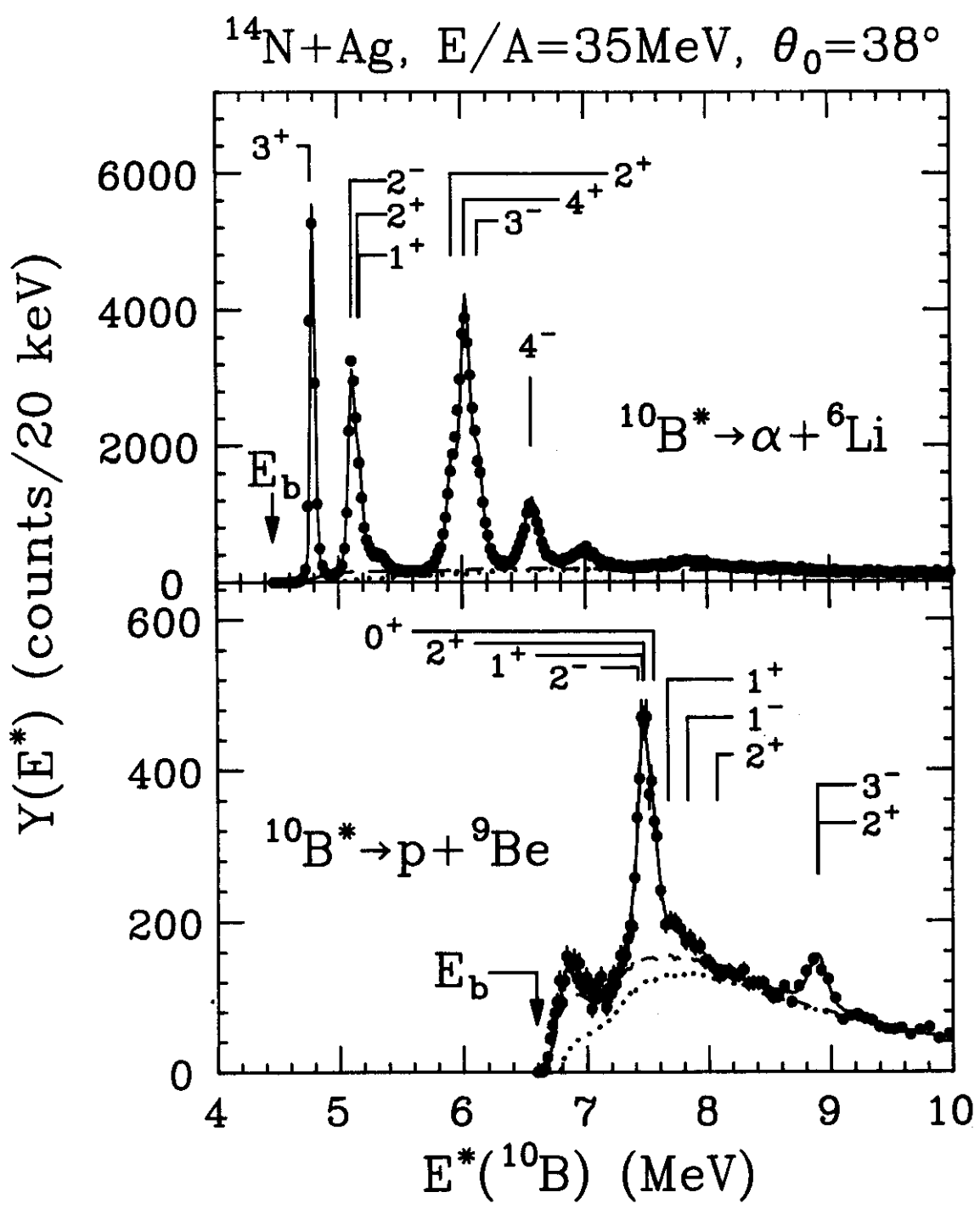


Fig. 14

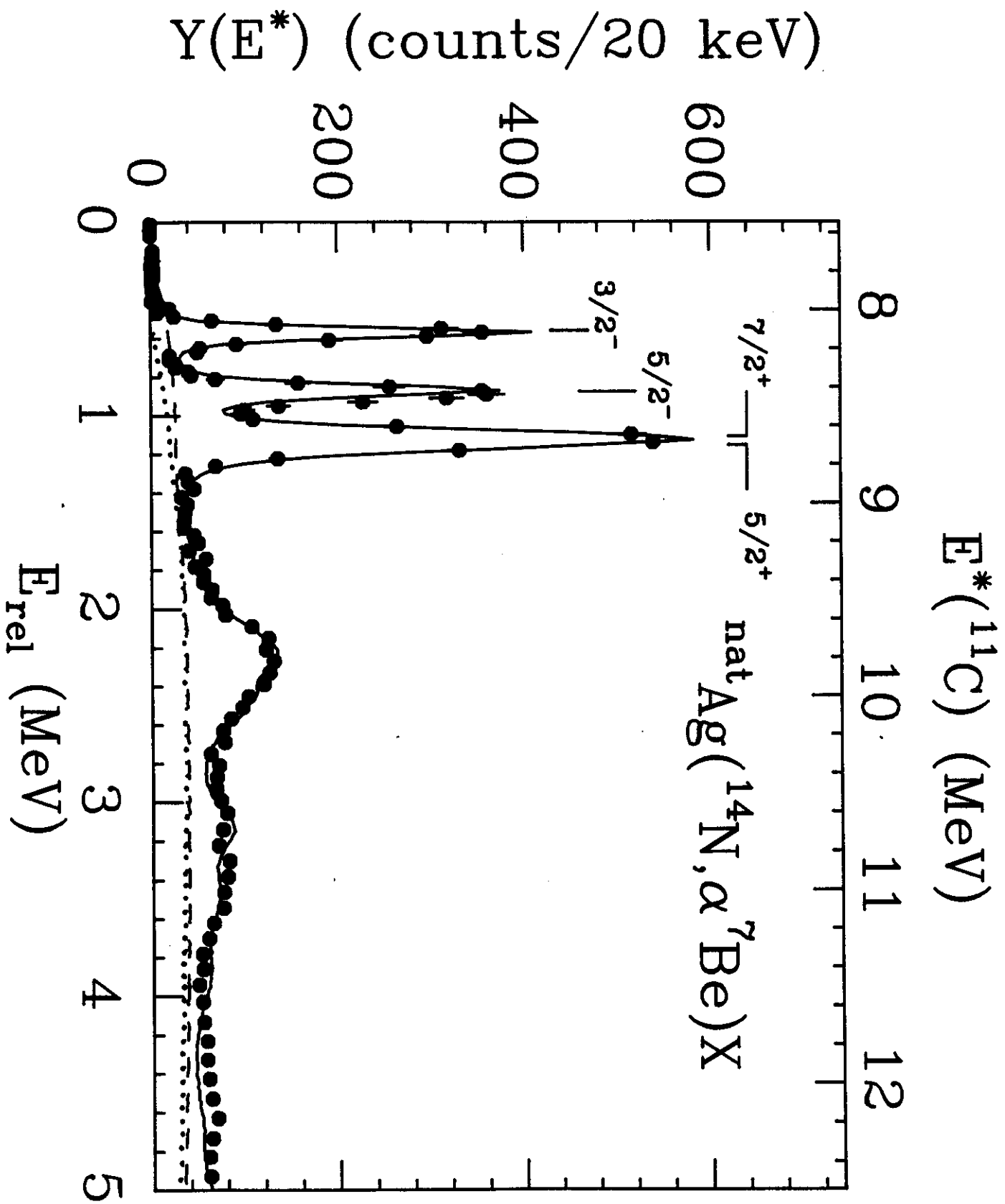


Fig 15

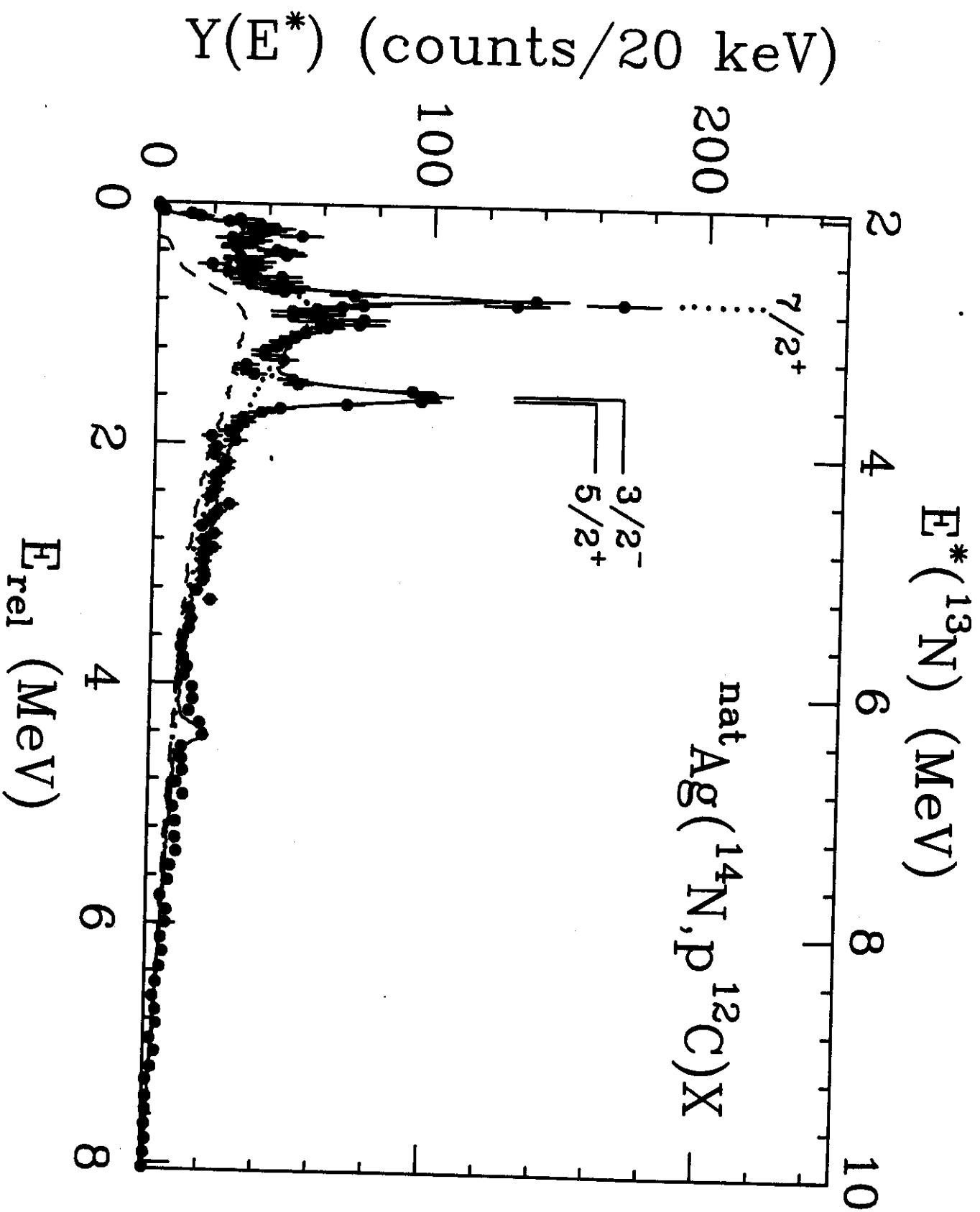


Fig 16

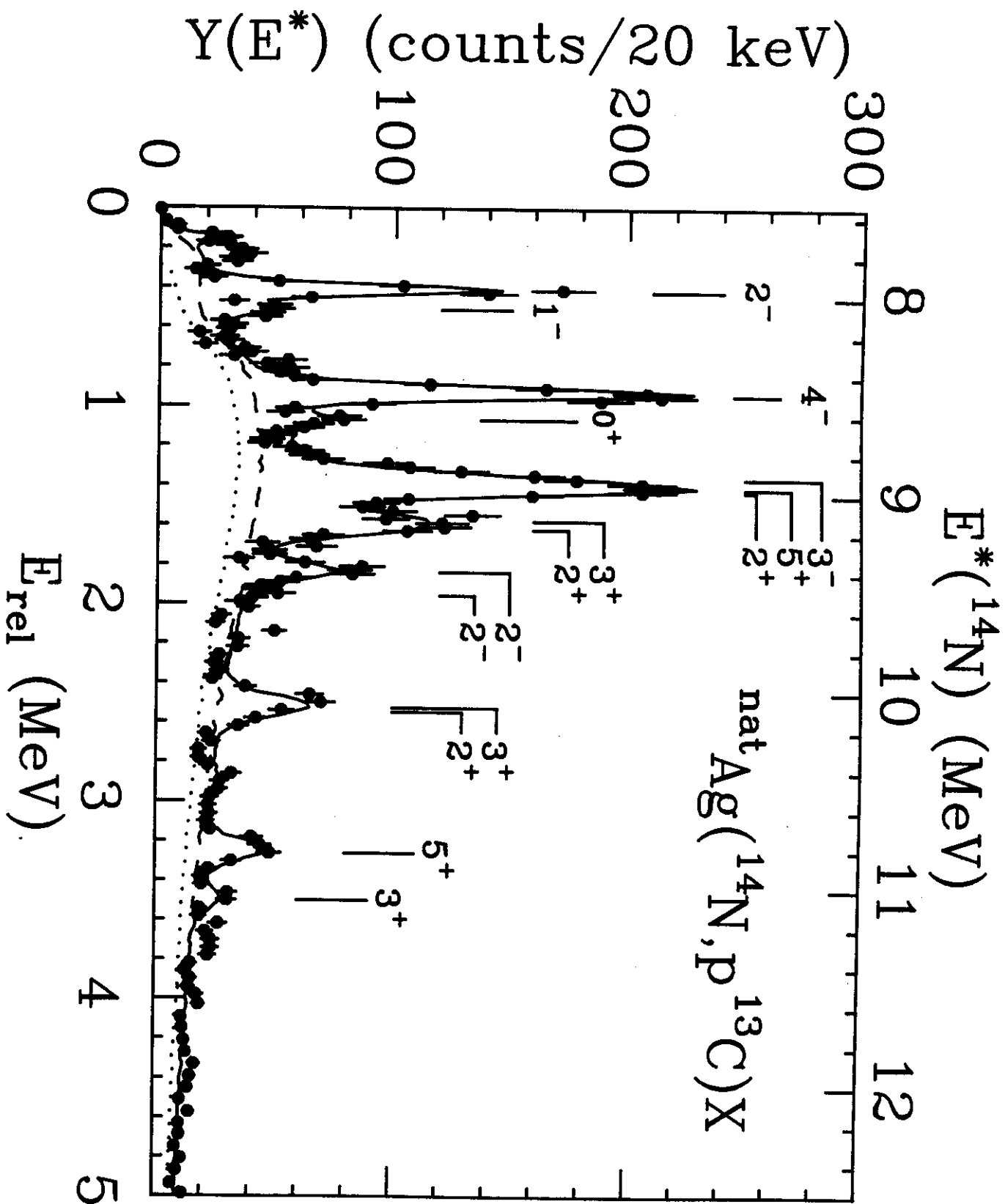


Fig 17

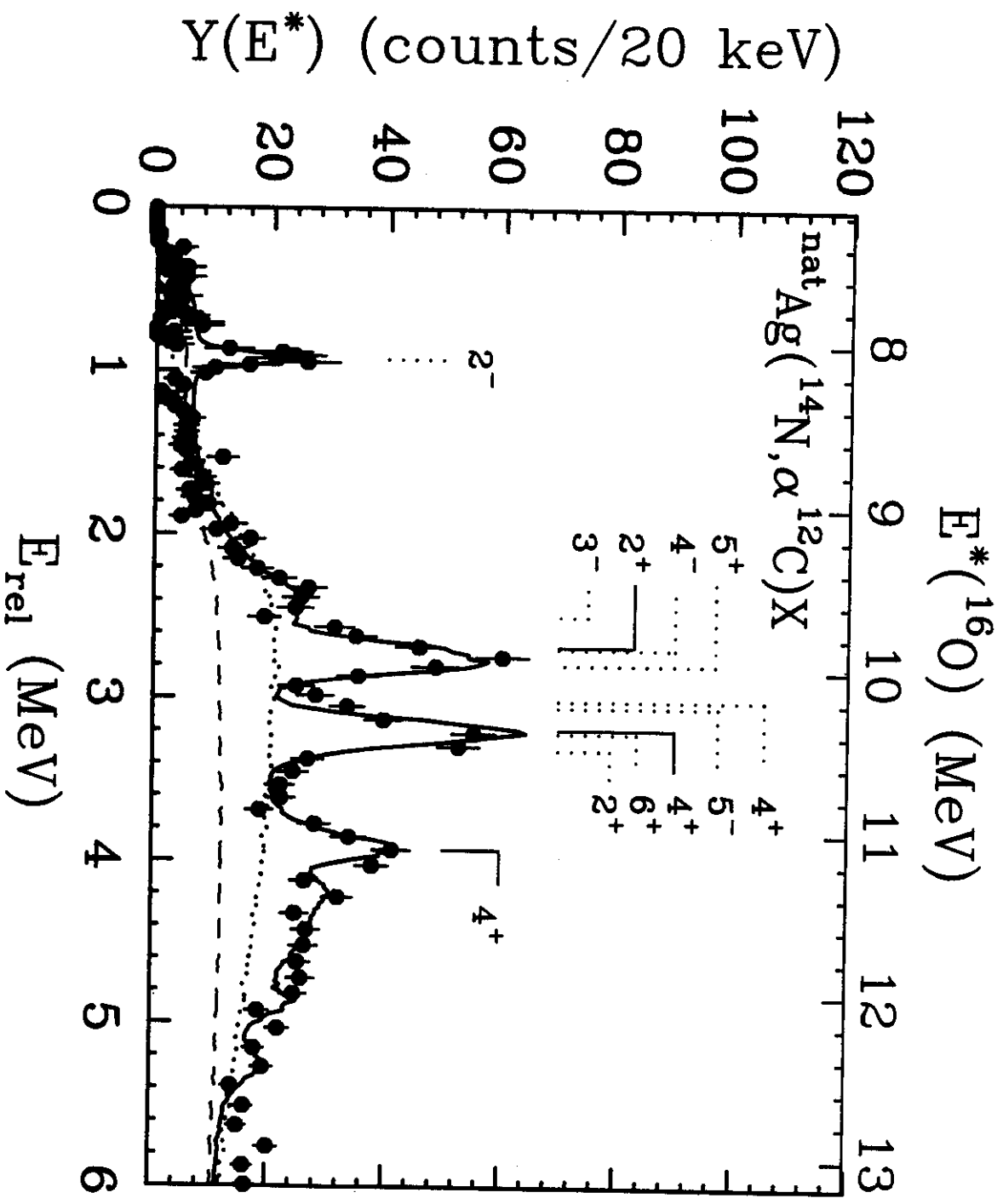


Fig 18

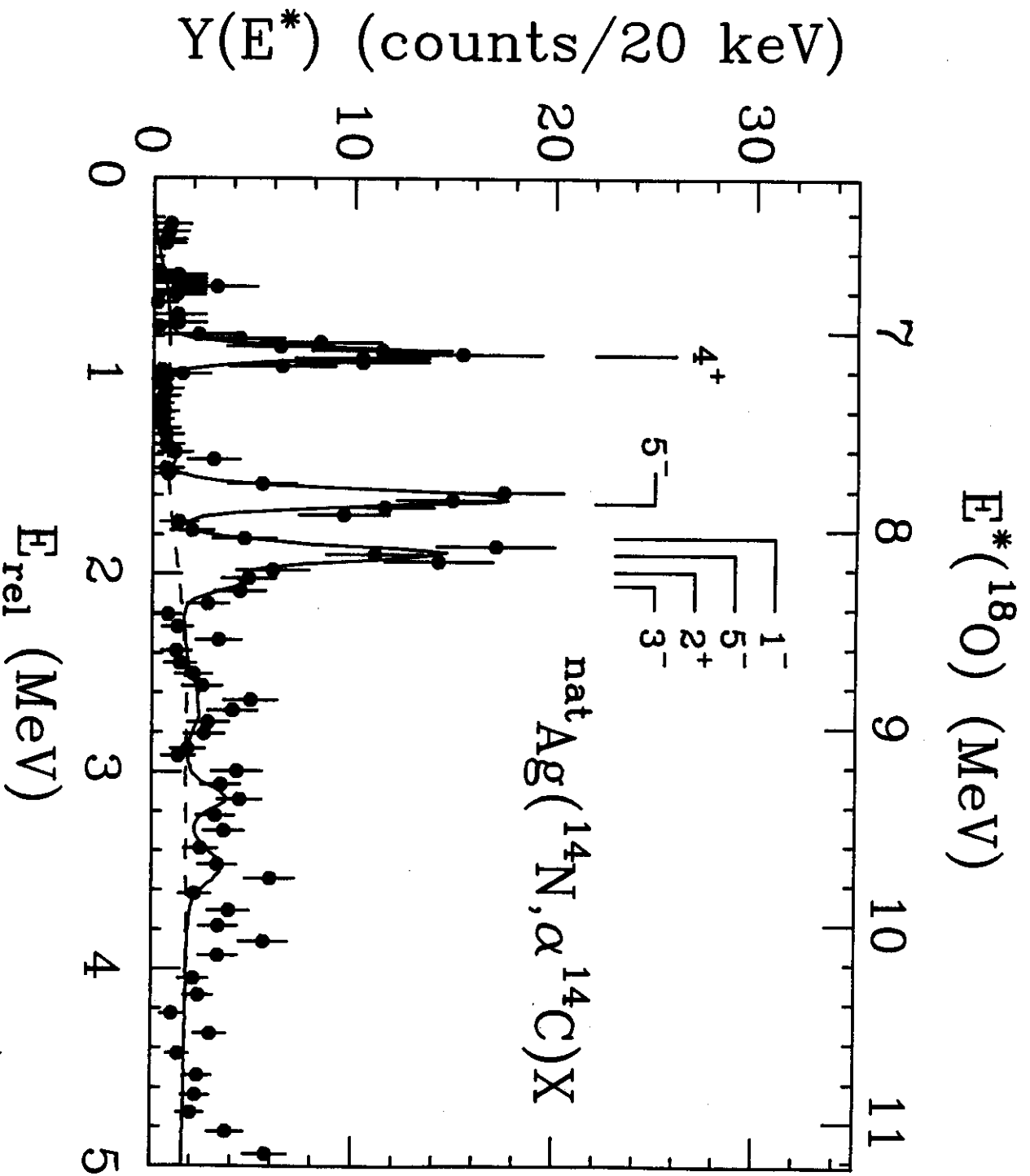


Fig 19

$^{14}\text{N} + \text{Ag}$, $E/A = 35 \text{ MeV}$, $\theta_0 = 38^\circ$

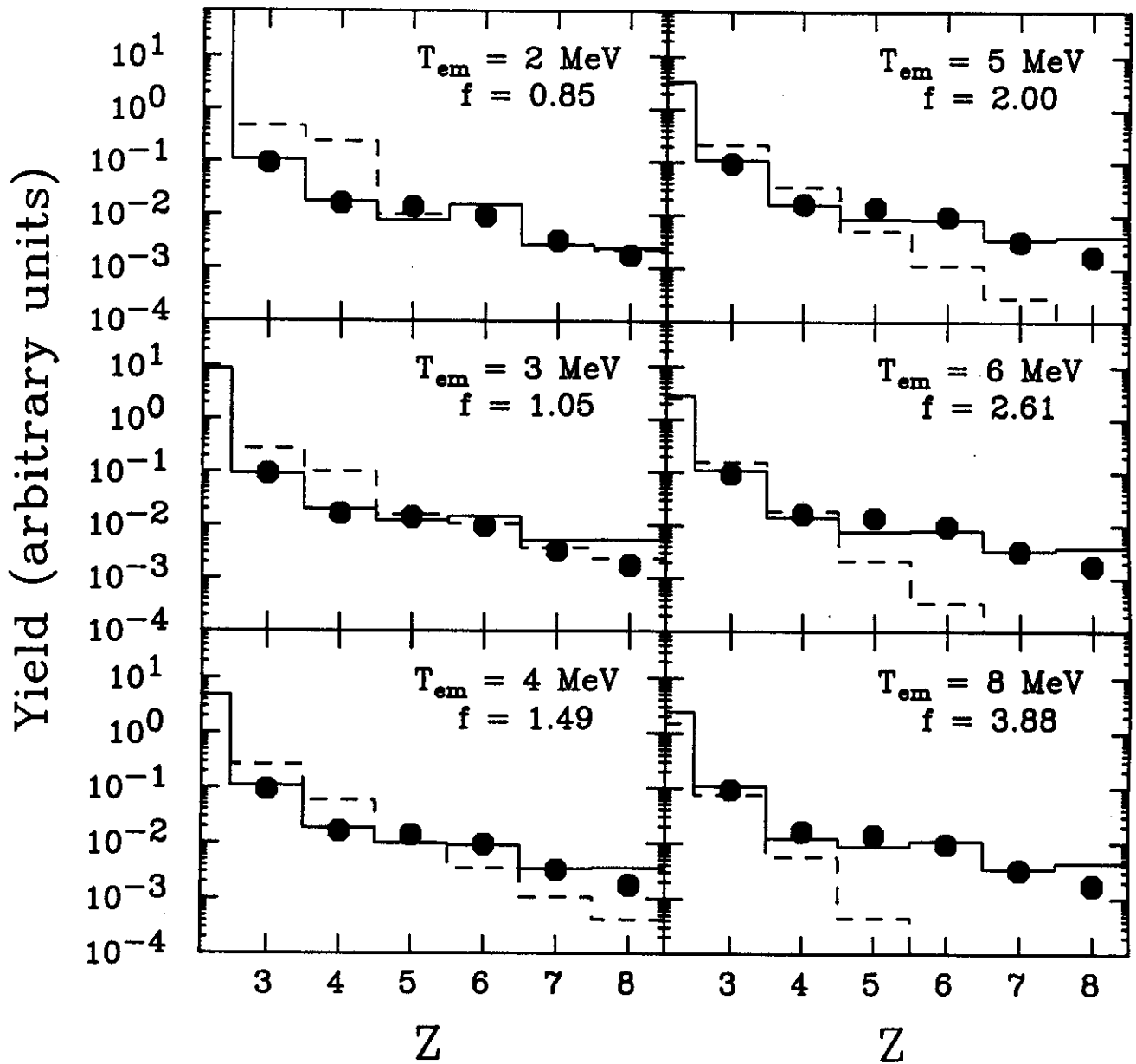


Fig. 20

$^{14}\text{N} + \text{Ag}$, $E/A = 35 \text{ MeV}$, $\theta_0 = 38^\circ$

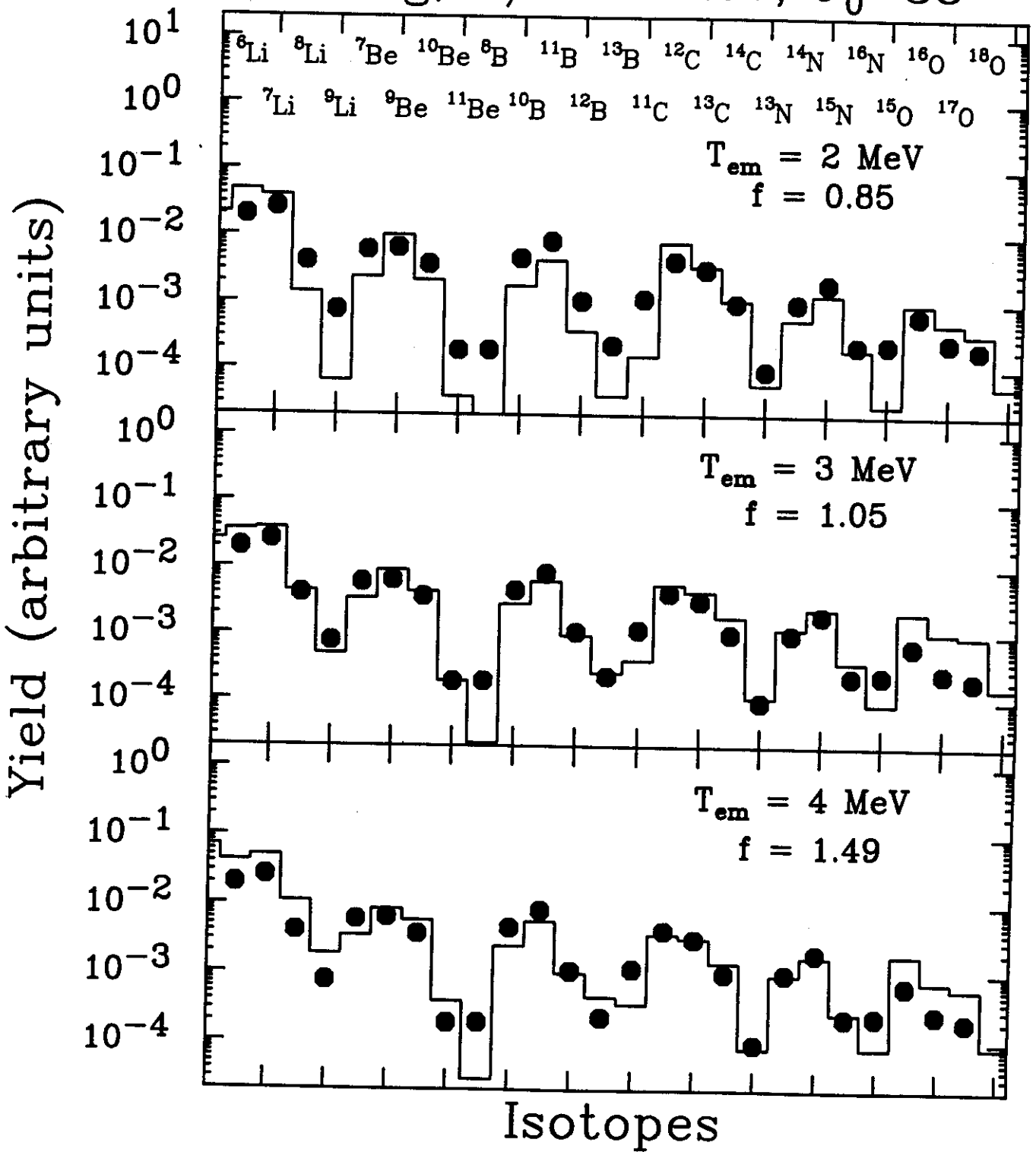


Fig 21

$^{14}\text{N} + \text{Ag}, E/A = 35 \text{ MeV}, \theta_0 = 38^\circ$

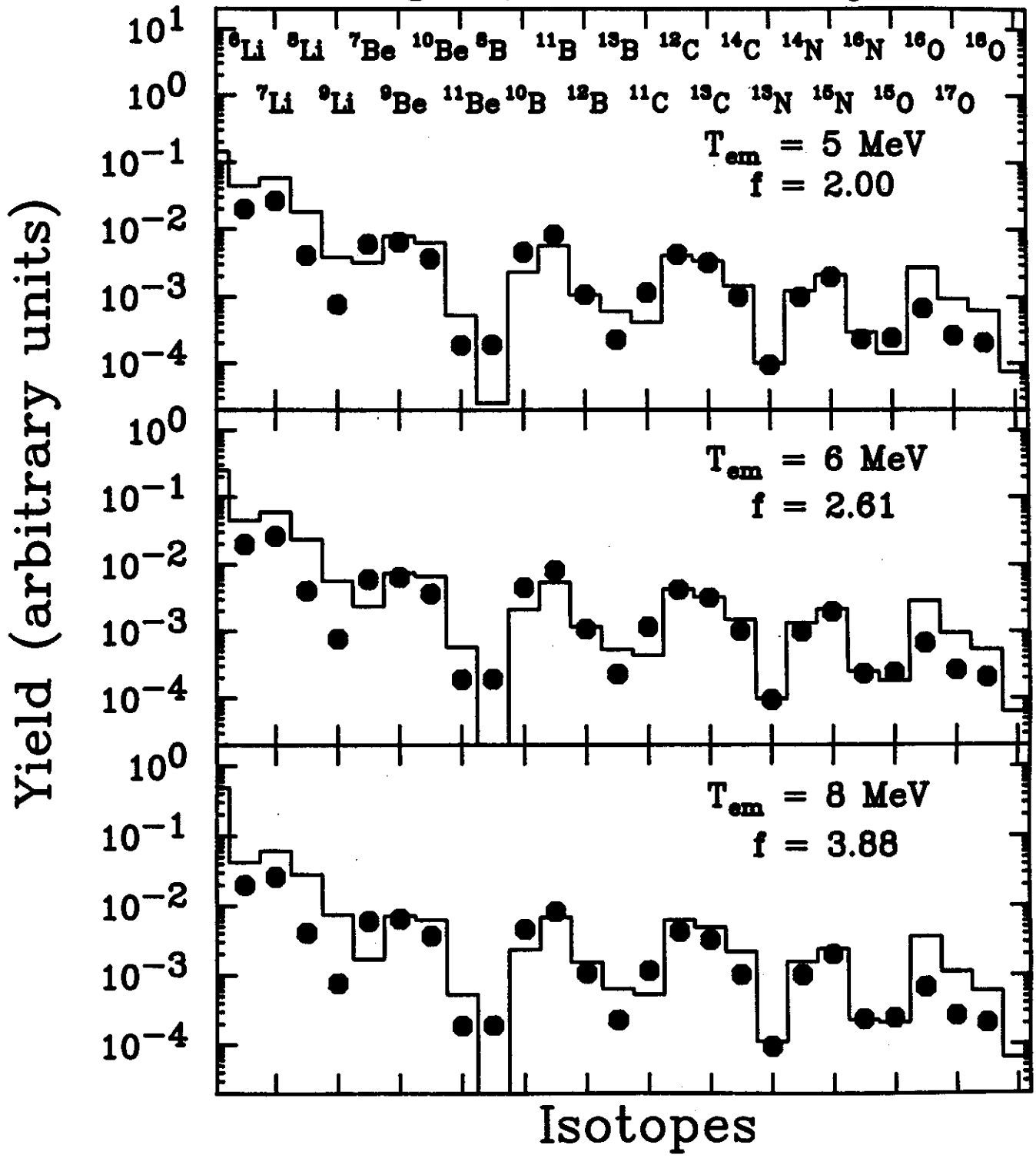


Fig. 22

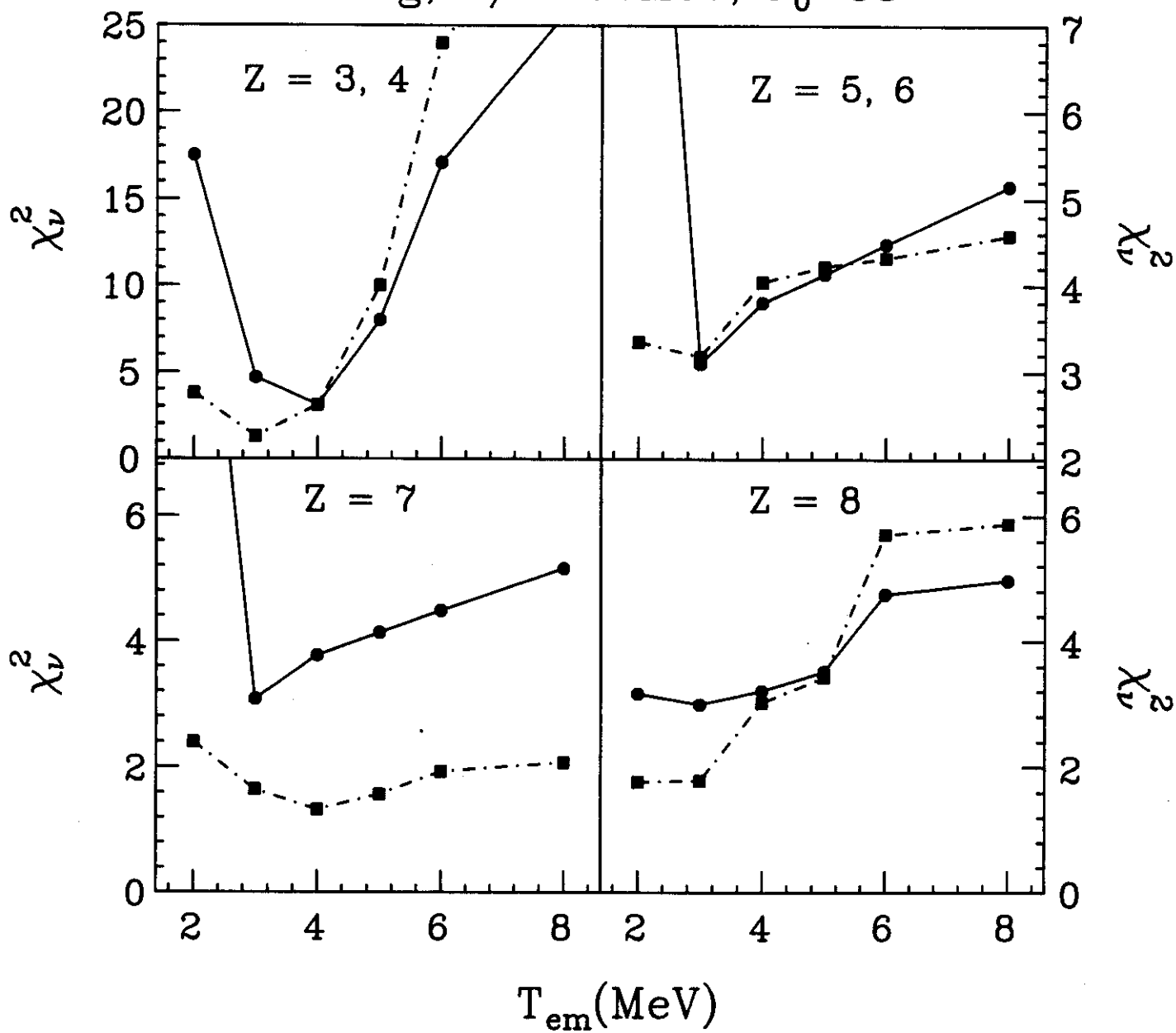
$^{14}\text{N} + \text{Ag}, E/A = 35 \text{ MeV}, \theta_0 = 38^\circ$ 

Fig. 23

$^{14}\text{N} + \text{Ag}$, $E/A = 35\text{MeV}$, $\theta_0 = 38^\circ$

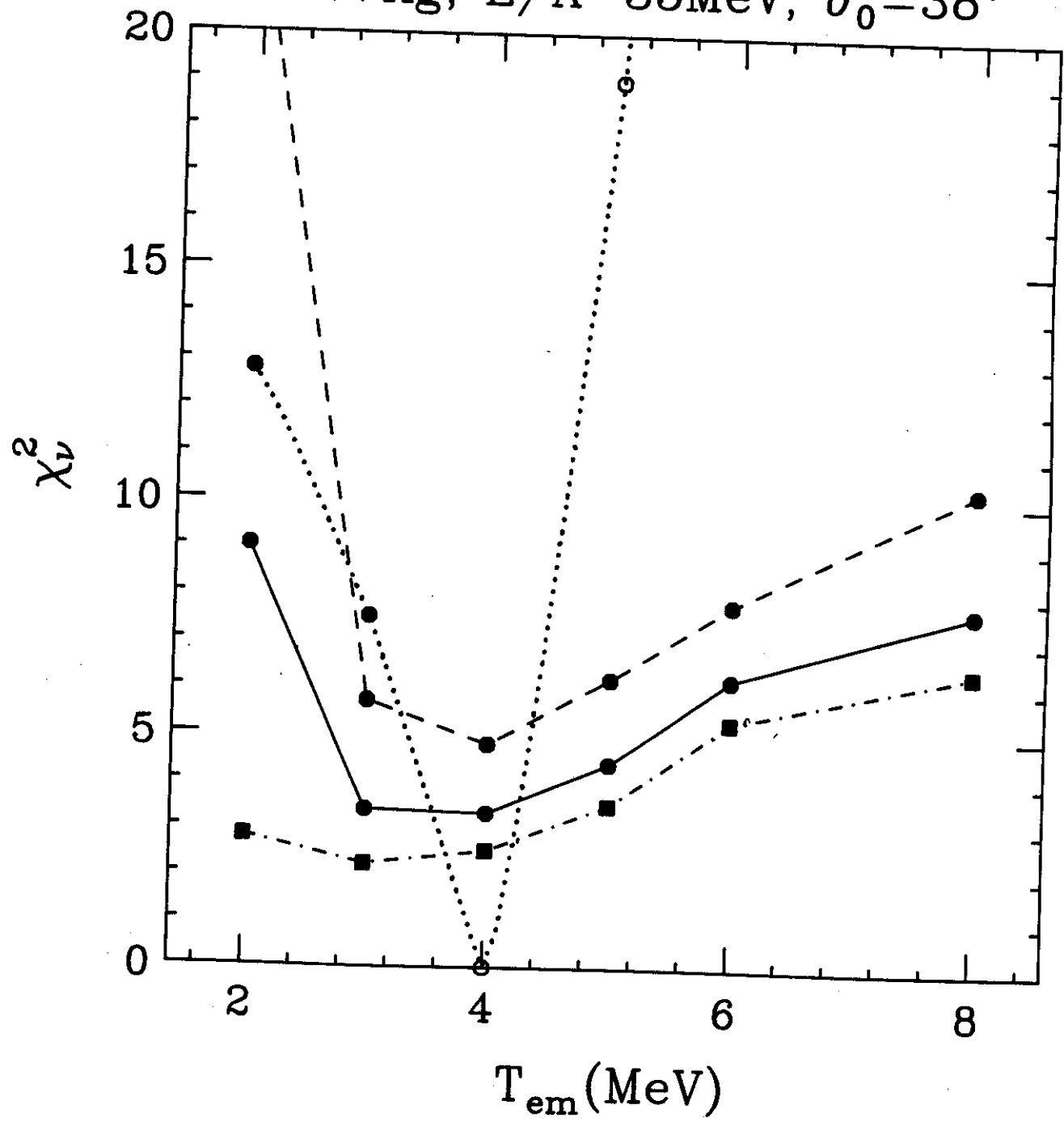


Fig 24

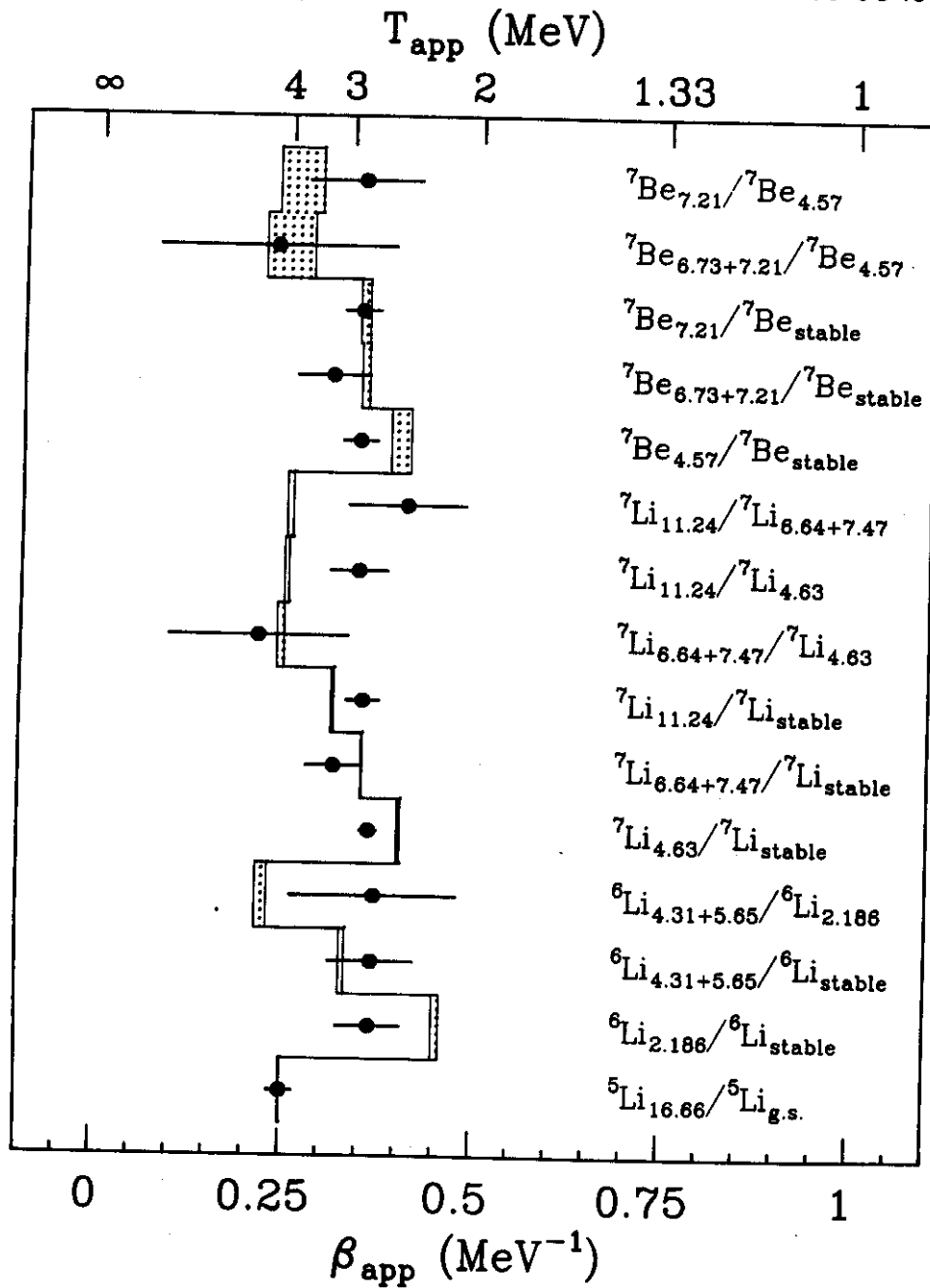


Fig. 25

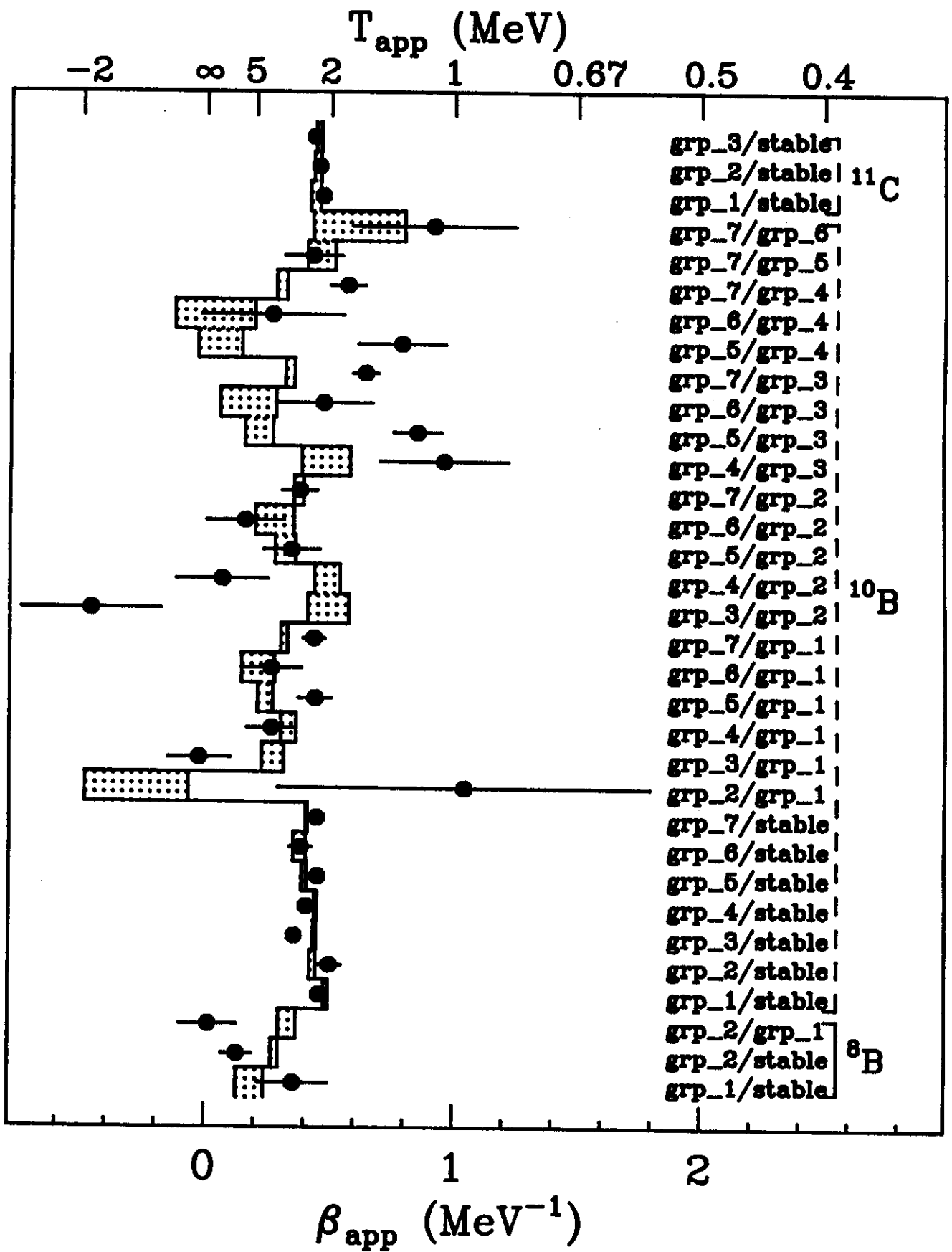


Fig. 26

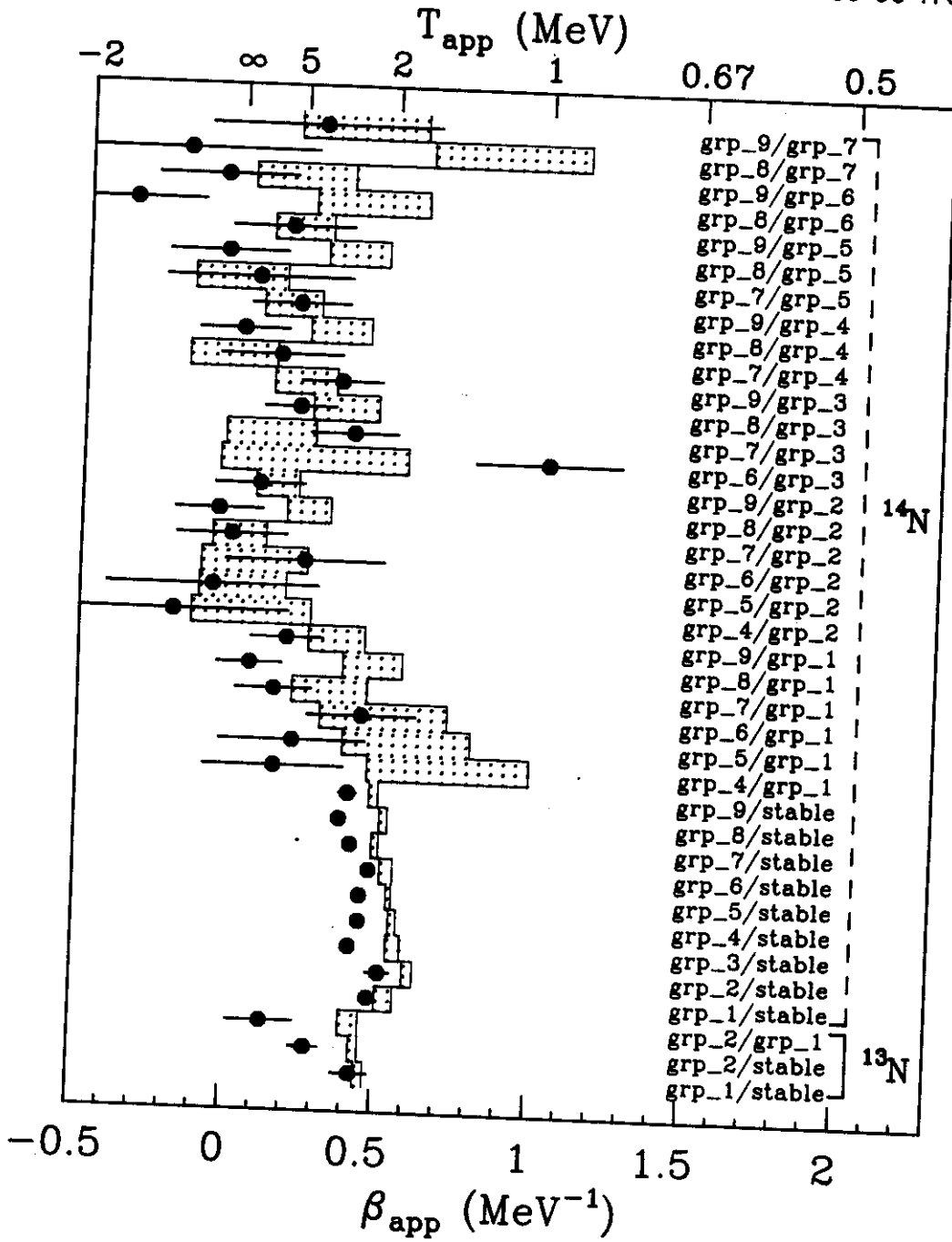


Fig. 27

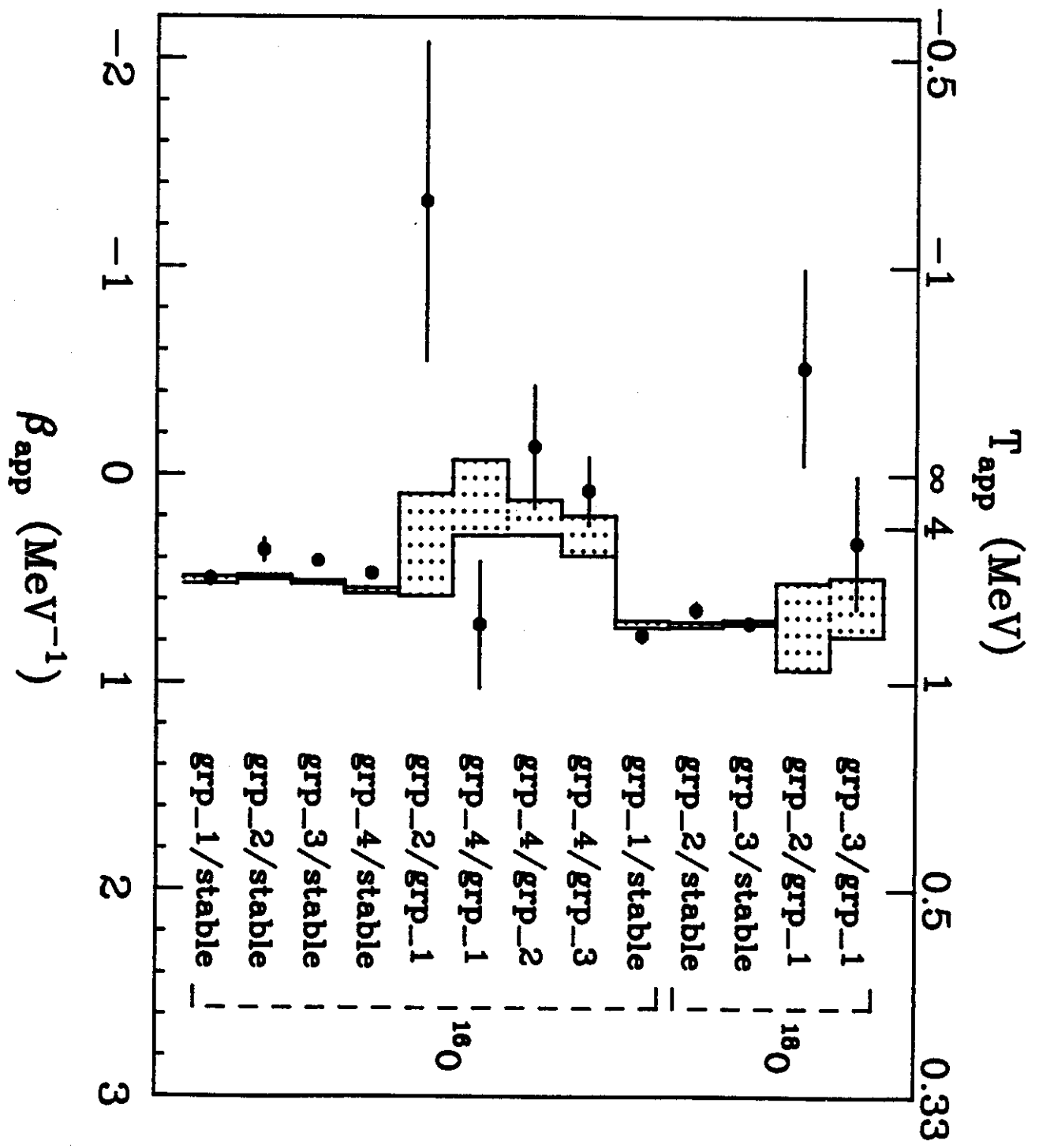


Fig. 28

$^{14}\text{N}+\text{Ag}$, $E/A=35\text{MeV}$, $\theta_0=38^\circ$

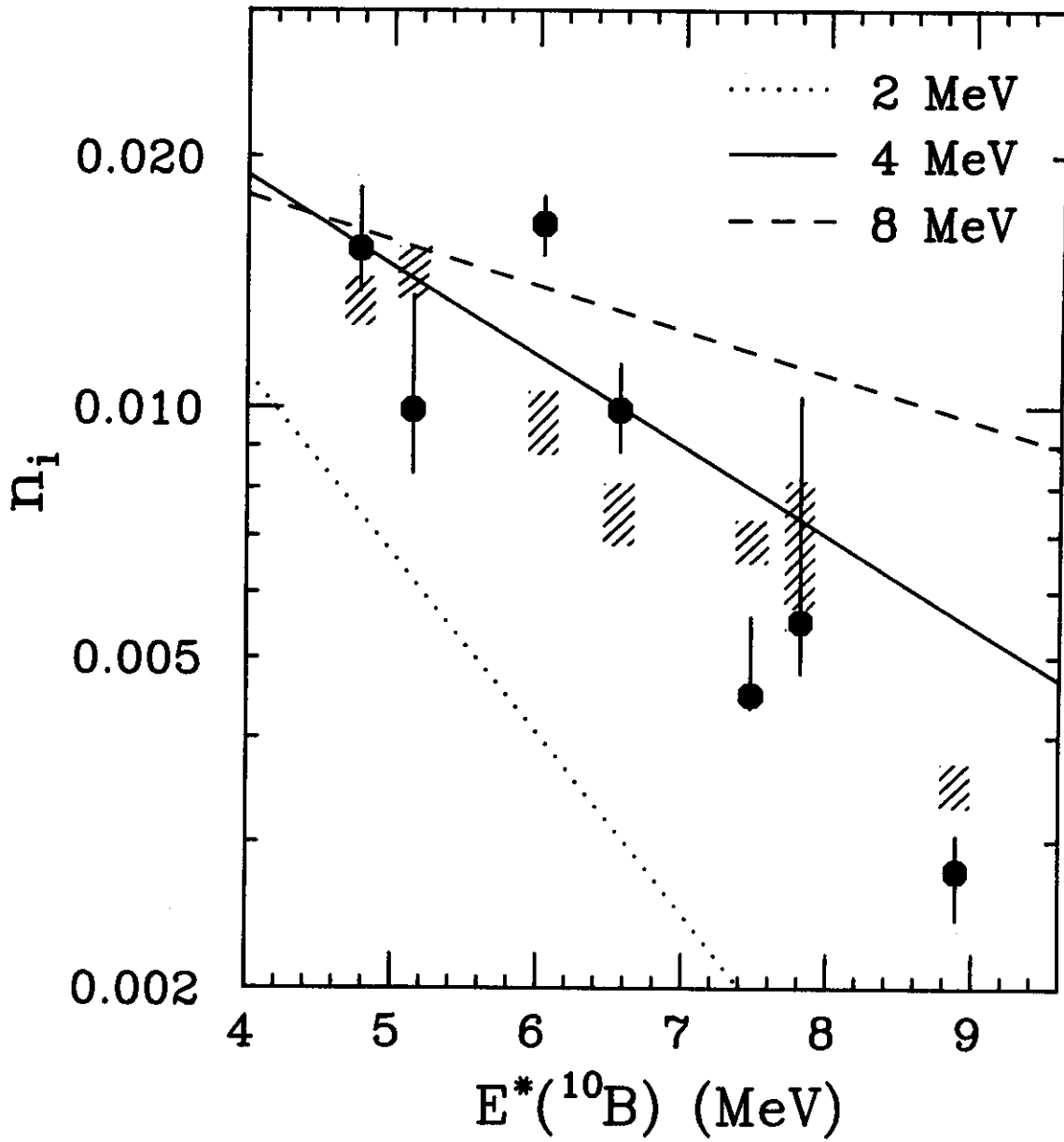


Fig. 29

$^{14}\text{N} + \text{Ag}$, $E/A = 35\text{MeV}$, $\theta_0 = 38^\circ$

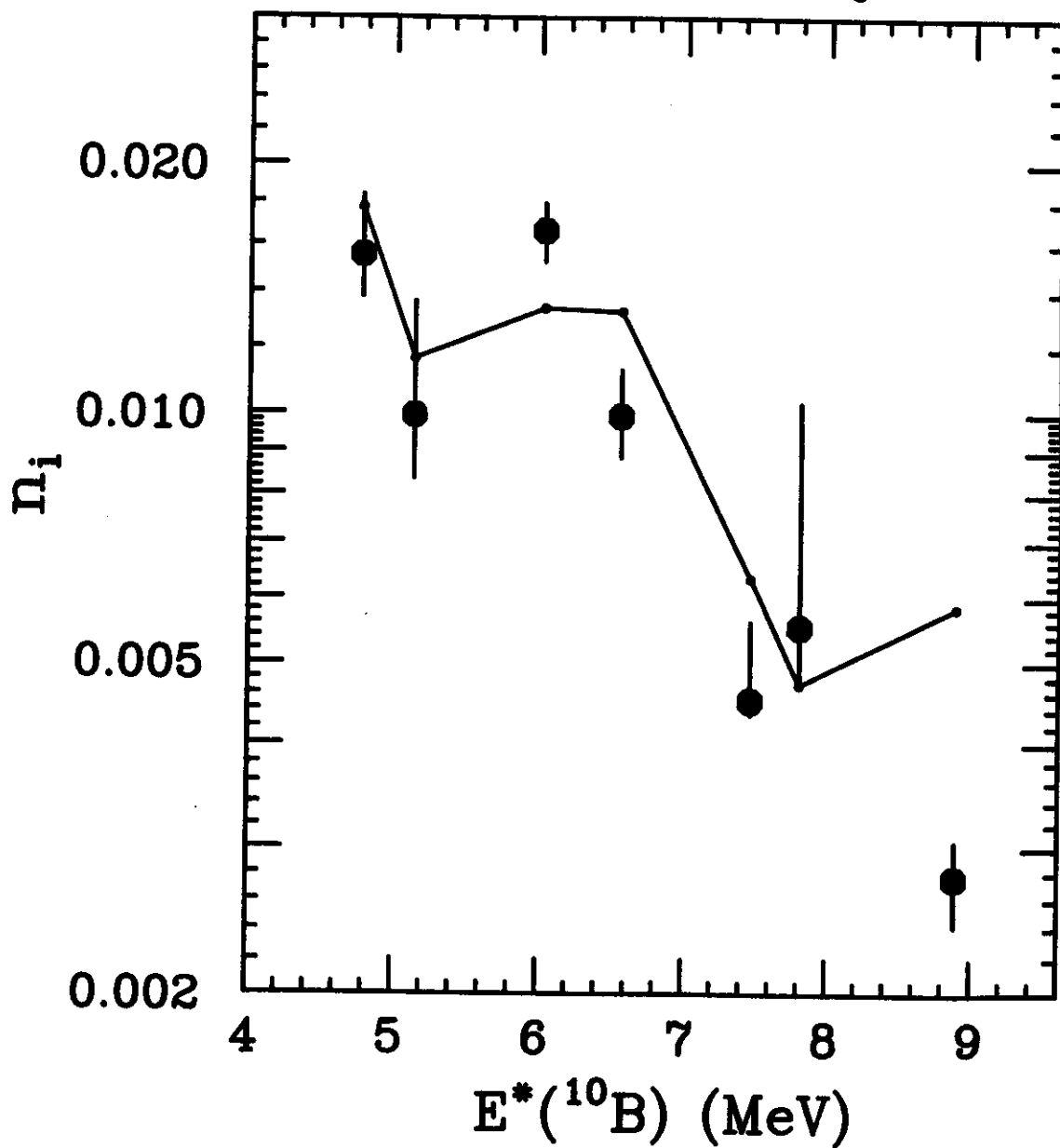


Fig 3D

$^{14}\text{N}+\text{Ag}$, $E/A=35\text{MeV}$, $\theta_0=38^\circ$

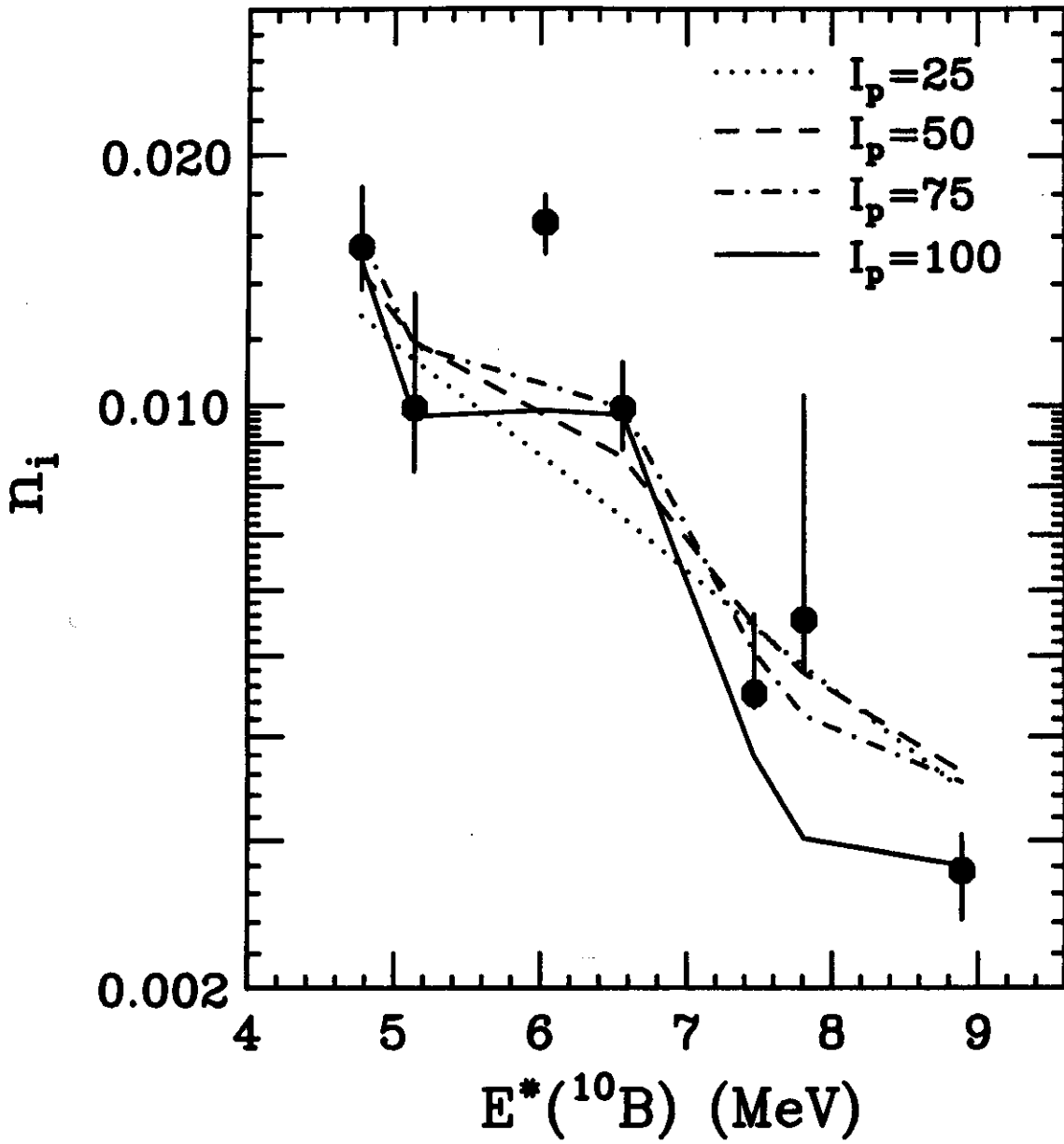


Fig 31

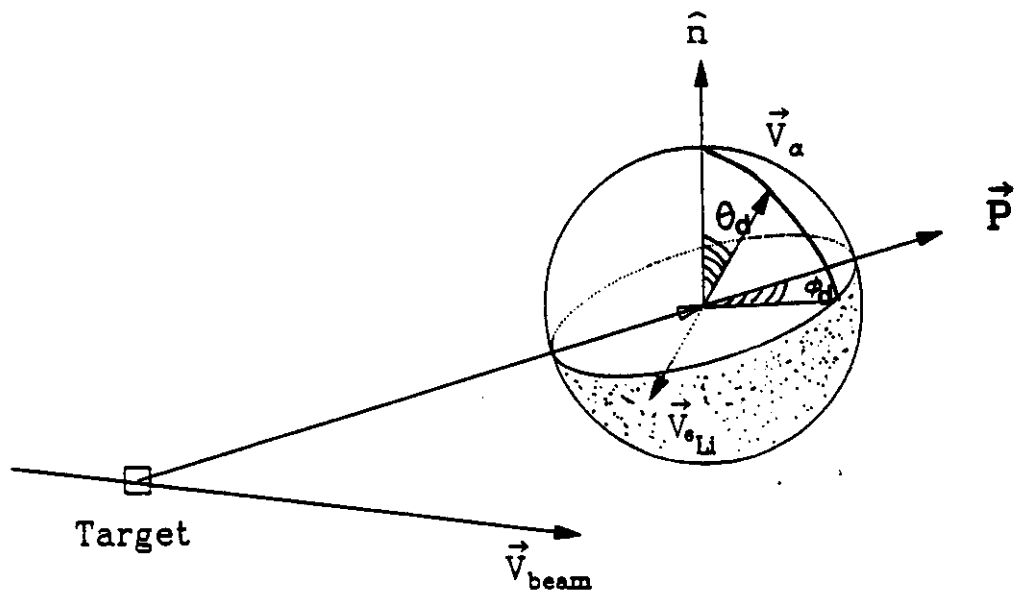


Fig 32

Theta Angular Distribution for $^{10}\text{B}^* \rightarrow \alpha + ^6\text{Li}$

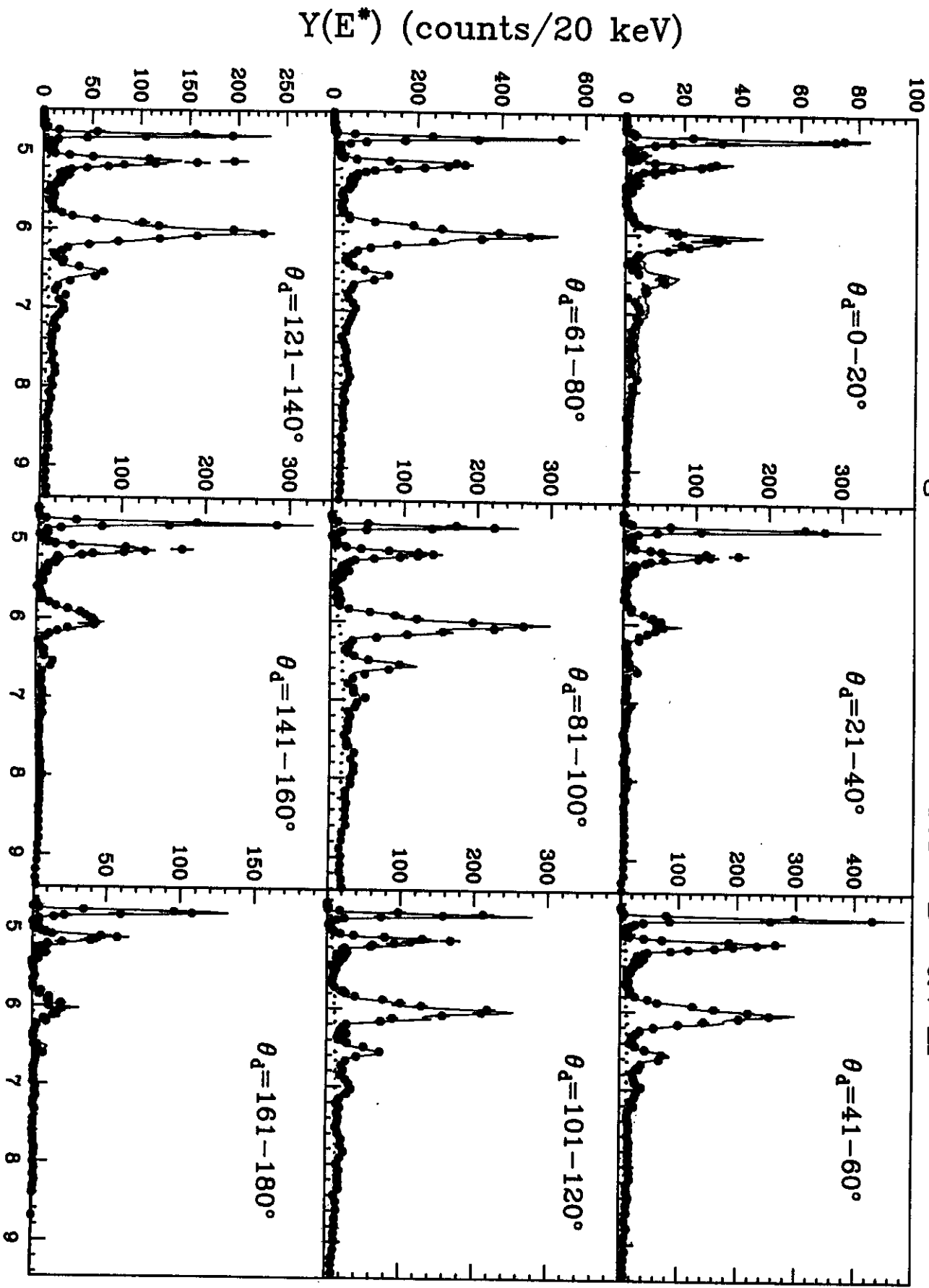


Fig 33

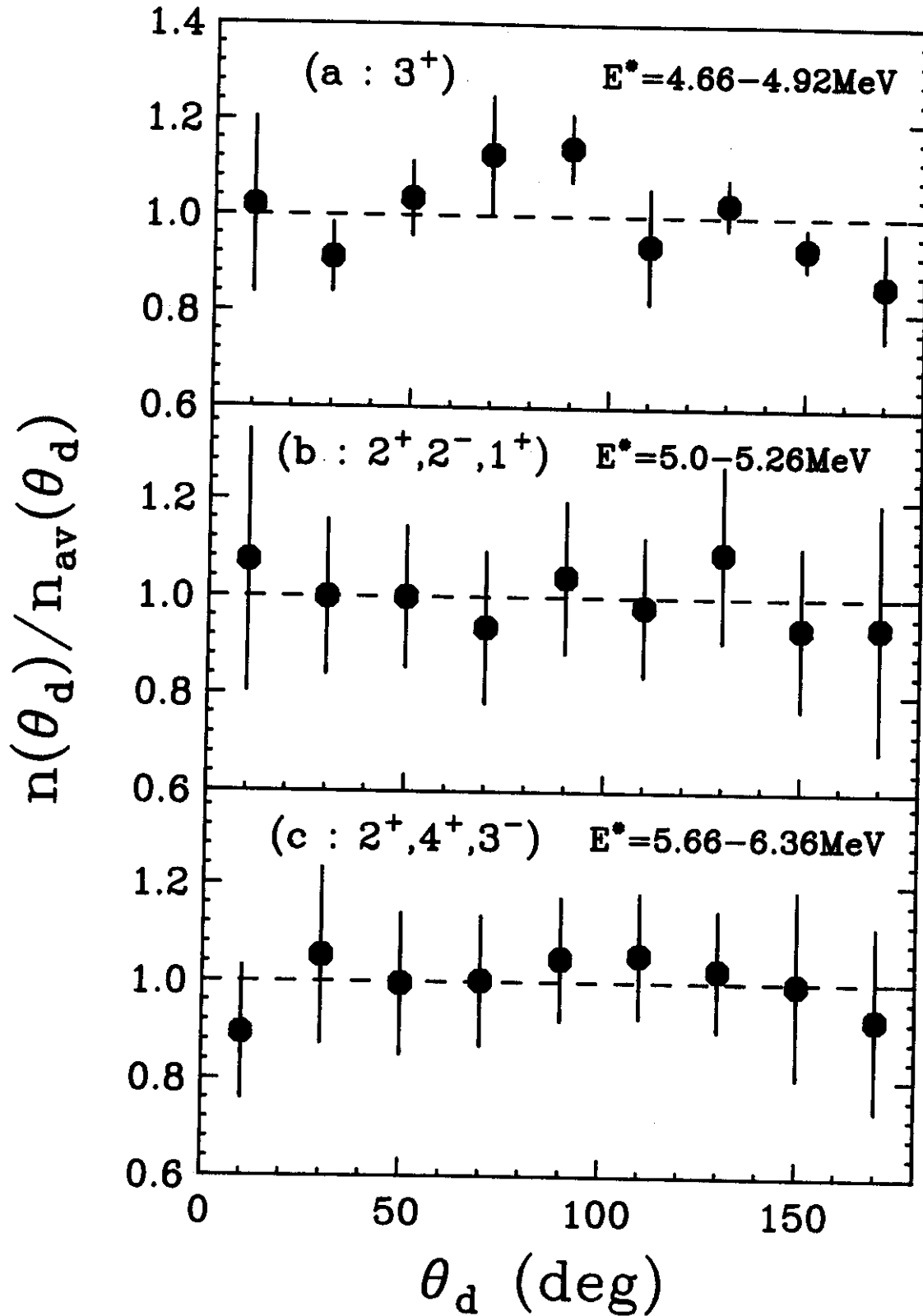
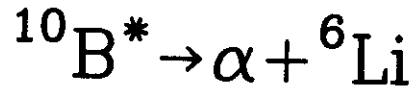


Fig 34

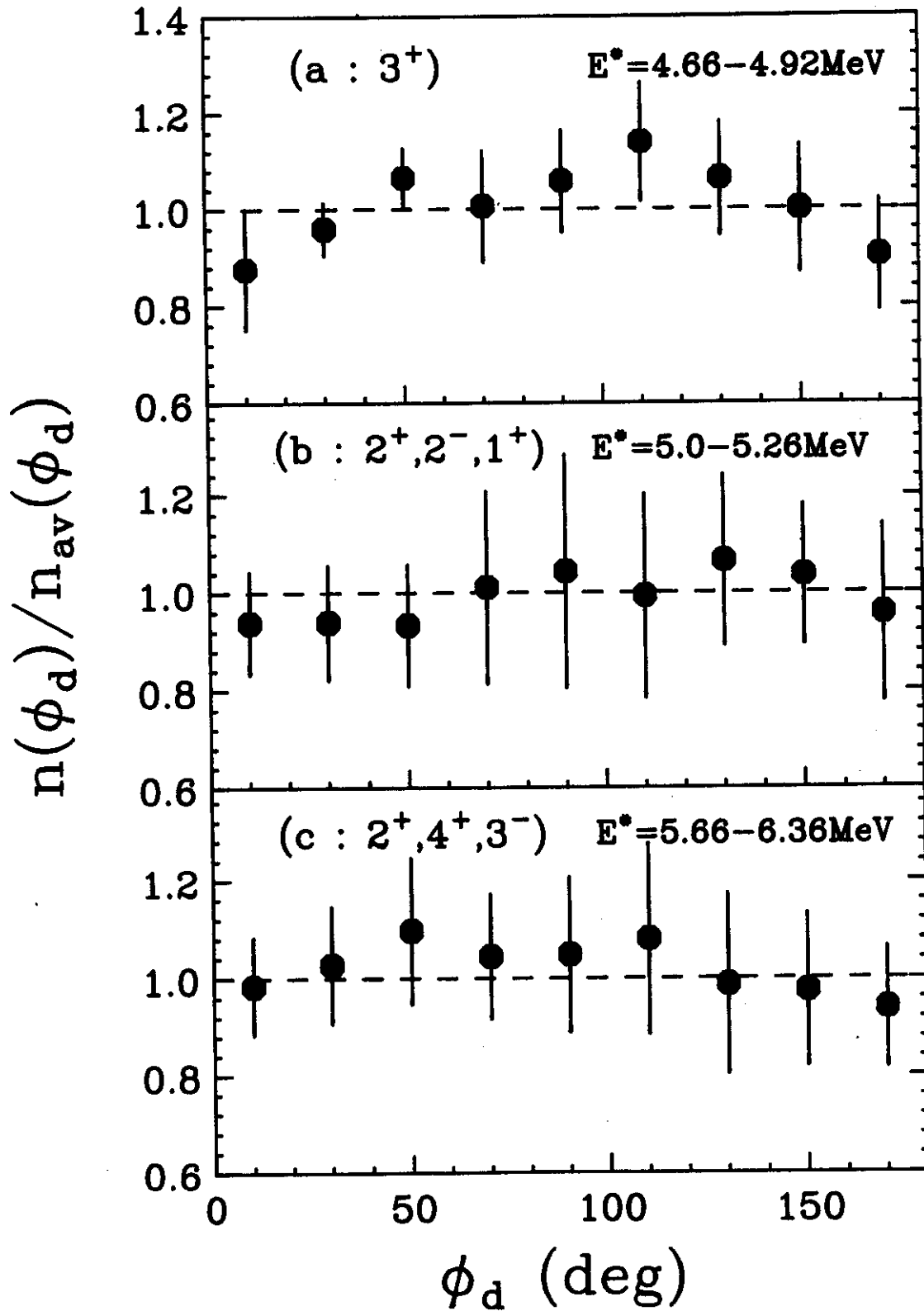
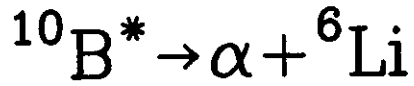


Fig 35

$^{10}\text{B} : 4.774 \text{ MeV} : \text{Full spin Coupling}$

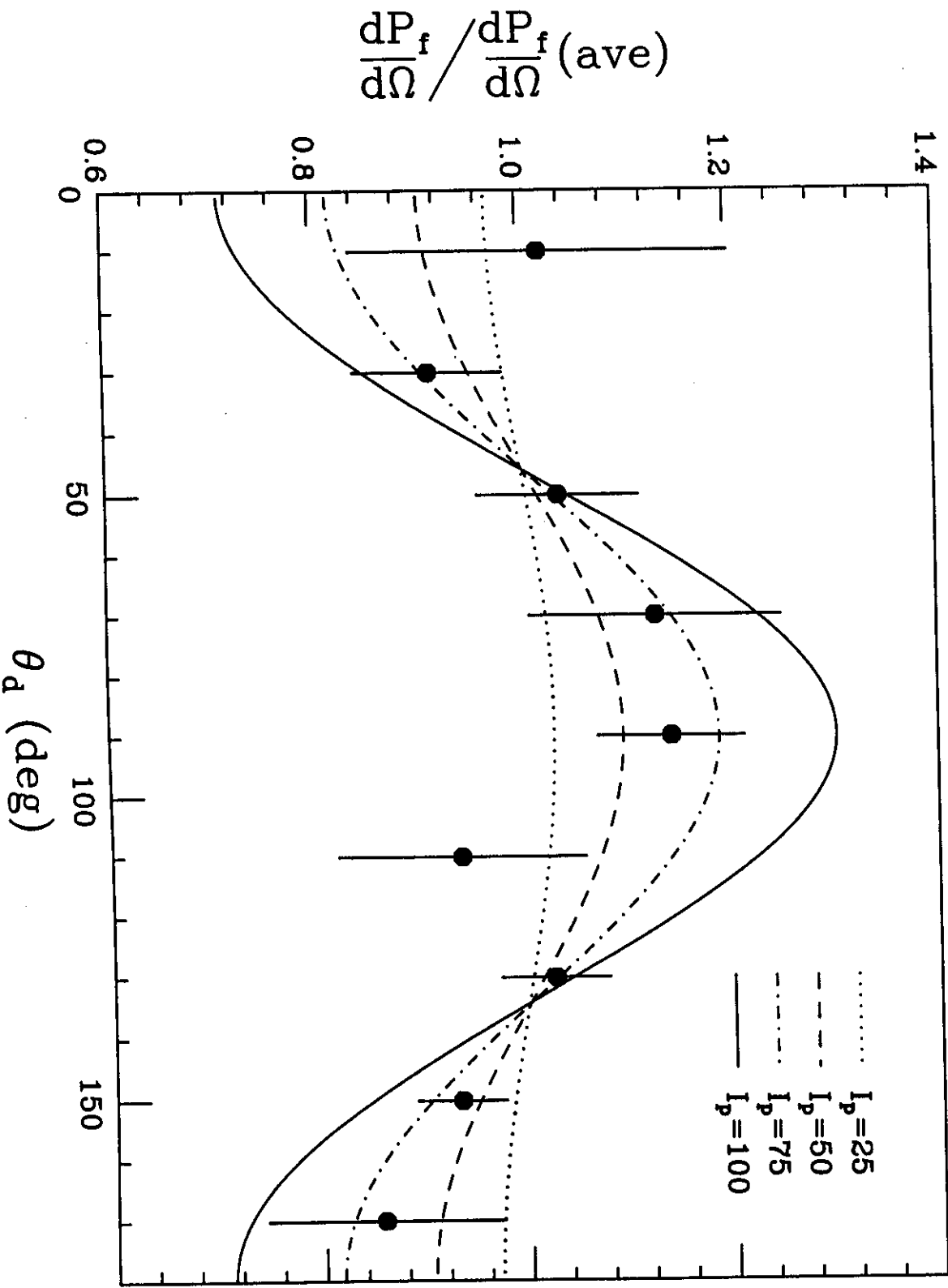


Fig 36